DEVELOPMENT OF HIGH PRESSURE MASS SPECTROMETRY FOR HANDHELD INSTRUMENTS

Kenion H. Blakeman

A dissertation submitted to the faculty at the University of North Carolina at Chapel Hill in partial fulfillment of the requirements for the degree of Doctor of Philosophy in the Department of Chemistry.

Chapel Hill
2015

Approved by:

J. Michael Ramsey

James W. Jorgenson

Matthew R. Lockett

James F. Cahoon

Eric M. Brustad

ABSTRACT

Kenion H. Blakeman: Development of High Pressure Mass Spectrometry for Handheld Instruments
(Under the direction of J. Michael Ramsey)

This work describes the development of microscale ion traps intended for high pressure mass spectrometry in handheld mass spectrometers. By operating at pressures approaching 1 Torr, the major size, weight and power (SWaP) contributor, the turbopump can be eliminated. Unlike other mass analyzers, ion traps can successfully operate at higher pressures by reducing the trap size and operating at higher RF drive frequencies.

HPMS was first demonstrated with helium buffer gas with volatile organic compounds (VOCs) and a r_o = 500 µm cylindrical ion trap (CIT). RF frequencies up to 10 MHz minimized mass resolution loss with pressure. HPMS with nitrogen and air were then explored as field available buffer gases to eliminate helium tanks in the field, reducing instrument size and weight. Peak widths at 1.0 Torr were 0.7 Da for helium and 5 Da for nitrogen and air were observed at RF drive frequencies of 10 MHz.

As peak widths widen at high pressures due to more frequent collisions, the RF frequency was increased along with a reduction in trap size to regain mass resolution. Five CITs were operated at 1 Torr in air with RF drive frequencies between 6.14 MHz to 59.44 MHz resulting in peak widths improving from 5.5 Da to 0.8 Da. Stretched length ion traps (SLITs) and 7-element CIT arrays improved sensitivity over the single element traps by

factors of 6 and 7. Operating at ambient air pressures between 250 mTorr and 1.0 Torr with RF frequencies between 30 MHz and 60 MHz reduced peak widths to sub-0.6 Da.

Finally, printed circuit board (PCB) and silicon ion traps were developed as alternative materials to metal ion traps. Both PCB and Si traps lower trap capacitance reducing RF power needs and improving instrument SWaP. PCB traps had a factor of two lower sensitivity and peak widths within 10% of metal traps while silicon ion traps had twice the signal intensity of metal traps and better peak widths by up to 30 %. In terms of fabrication, PCB traps can be mass produced while Si traps can be produced with higher dimensional fidelity than metal ion traps.

ACKNOWLEDGEMENTS

I would first like to thank my adviser J. Michael Ramsey for the opportunity to work in his research group over the past 5 years. J.P. Alarie and Tina Stacy were helpful in both getting me established in lab and then editing my dissertation. I would also like to thank everyone from the Ramsey group, especially the micro-mass spectrometry sub-group for the many useful discussions and collaborations. Derek Wolfe and Craig Cavanaugh were close collaborators in many early projects, as were many other group members in later projects. I received significant RF electronics support from Harry Chase, Collin McKinney, and the UNC Electronics facility. Finally, I would like to thank my friends and family for their support throughout graduate school.

TABLE OF CONTENTS

LIST OF TABLES x

LIST OF FIGURES xi

LIST OF ABBREVIATIONS AND SYMBOLS xvi

CHAPTER 1: INTRODUCTION TO MINIATURE MASS SPECTROMETRY AND QUADRUPOLE ION TRAPS 1

1.1 Motivation for Handheld Mass Spectrometers 1

1.2 Current Handheld Chemical Instrumentation 3

1.3 Portable Mass Spectrometry 5

1.4 Quadrupole Ion Trap Background 9

1.4.1 Mass Analysis by QITs 9

1.4.2 Mass Resolution for QITs 11

1.4.3 Sensitivity for QITs 12

1.4.4 Simplified Ion Trap Geometries 14

1.4.4 Higher Order Field Components 16

1.5 High Pressure Mass Spectrometry 17

1.6 Objectives 19

1.7 Figures 21

1.8 References 25

CHAPTER 2: DEVELOPING HPMS WITH HELIUM BUFFER GAS 34

2.1 Introduction 34

2.2 Experimental 34

2.3 Ionization Source 37

2.3.1 Ionization Source Optimization 38

2.3.2 Effect of Pressure on Mass Resolution 40

2.4 The Microionizer 43

2.4.1 Microionizer Concept and Operation 45

2.4.2 Microionizer Generated High Pressure Mass Spectra 46

2.5 Conclusions 50

2.6 Figures 51

2.7 References 63

CHAPTER 3: DEVELOPING HPMS WITH NITROGEN AND AIR BUFFER GASES 68

3.1 Introduction 68

3.2 Filament Electron Source 69

3.3 Glow Discharge-Electron Ionization 70

3.3.1 Emission Studies 71

3.3.2 High Pressure Comparison with Different Buffer Gasses 73

3.4 Conclusions 79

3.5 Figures 80

3.6 References 93

CHAPTER 4: HIGH RF DRIVE FREQUENCY TRAP OPERATION FOR IMPROVED MASS RESOLUTION.....97

4.1 Introduction.....97

4.2 Proof of Concept Experiments.....100

4.2.1 Low Pressure Helium.....101

4.2.2 High Pressure Helium.....103

4.3 High RF Frequency Operation with Air Buffer Gas.....104

4.3.1 Miniaturization of CITs.....104

4.3.2 CIT Arrays and SLITs.....108

4.3.3 Tradeoffs between Mass Resolution, Pressure, and RF Frequency.....111

4.4 Conclusions.....113

4.5 Tables and Figures.....115

4.6 References.....131

CHAPTER 5: CHARACTERIZING NEW ELECTRODE MATERIALS.....135

5.1 Introduction.....135

5.2 PCB Traps.....138

5.2.1 PCB Electrodes Physical Properties.....139

5.2.2 PCB Ion Trap Performance.....140

5.3 Silicon Ion Traps.....146

5.3.1 Silicon Electrodes Physical Properties.....147

5.3.2 Silicon Ion Trap Performance.....148

5.4 Conclusions.....151

5.6 Tables and Figures.....153

5.7 References.....173

CHAPTER 6: CONCLUSIONS AND FUTURE DIRECTIONS.....178

6.1 Conclusions.....178

6.2 Future Directions 180

6.3 References.....183

LIST OF TABLES

Table 4.1: Critical dimensions for CITs used to investigate high RF frequencies 115

Table 4.2: Critical dimensions for SLITs used to investigate high RF frequencies 116

Table 5.1: Critical dimensions for PCB ion traps used to compare ion trap performance with different materials.....153

Table 5.2: Critical dimensions for silicon ion traps used to compare ion trap Performance with different materials 154

LIST OF FIGURES

Figure 1.1: Schematic for a QIT showing the hyperbolic ring and endcap electrodes 21

Figure 1.2: Stability diagram for an ideal QIT showing the regions of ion stability and instability 22

Figure 1.3: Schematic for a CIT showing the simplified electrode geometry used to simplify fabrication on the microscale 23

Figure 1.4: Graphical depiction of the CIT vs. SLIT trap where the length of the SLIT feature is used to improve sensitivity 24

Figure 2.1: Schematic for a differentially pumped mass spectrometer used to develop the miniaturized ion traps independently of the detector 51

Figure 2.2: Schematic for the instrumentation used to generate high RF drive frequency voltages used to perform mass analysis with the miniaturized ion traps 52

Figure 2.3: Mass spectra showing Xenon signal increasing with electron energy in 1.2 Torr of helium 53

Figure 2.4: Mass spectra of mesitylene showing an improvement in signal with increasing electron energy in 1.0 Torr of helium 54

Figure 2.5: Mass spectra of CEES with increasing helium buffer gas pressure from 62 mTorr to 1.2 Torr 55

Figure 2.6: Experimental and calculated peak widths for CEES 75 Da peak as a function of increasing helium pressure 56

Figure 2.7: Mass spectra of octane as a function of increasing helium buffer gas pressure from 110 mTorr to 1.0 Torr 57

Figure 2.8: Experimental and calculated peak widths for octane 41 Da peak as a function of increasing helium pressure 58

Figure 2.9: Optical and SEM images of a microionizer 59

Figure 2.10: Schematic of the microionizer showing the device dimensions and operating conditions 60

Figure 2.11: Mass spectra of Xenon acquired with the microionizer in 1.3 Torr of helium 61

Figure 2.12: Mass spectra of DMMP acquired with the microionizer in 1.0 Torr of helium 62

Figure 3.1: Comparison of CEES mass spectra taken in 7 mTorr of helium and nitrogen buffer gases 80

Figure 3.2: Mass spectra of MES with increasing nitrogen buffer gas pressure from 130 mTorr to 1.0 Torr 81

Figure 3.3: Instrument setup for acquiring mass spectra and current density measurements with glow discharge as the ionization source 82

Figure 3.4: Current density measurements in helium, nitrogen, and air buffer gases for the glow discharge source and filament 83

Figure 3.5: Mass spectra of *p*-xylene with increasing helium buffer gas pressure from 510 mTorr to 1.0 Torr 84

Figure 3.6: Mass spectra of *p*-xylene with increasing nitrogen buffer gas pressure from 490 mTorr to 1.9 Torr 85

Figure 3.7: Mass spectra of *p*-xylene with increasing air buffer gas pressure from 490 mTorr to 1.9 Torr 86

Figure 3.8: Comparison of *p*-xylene mass spectra in 1.0 Torr of helium, nitrogen, and air buffer gases 87

Figure 3.9: Peak widths for *p*-xylene 106 Da peak with increasing buffer gas pressures for helium, nitrogen, and air 88

Figure 3.10: Integrated peak area for *p*-xylene with increasing nitrogen and air buffer gas pressures 89

Figure 3.11: Signal-to-noise for *p*-xylene with increasing nitrogen and air buffer gas pressures 90

Figure 3.12: Mass spectra for a VOC mixture in 1.0 Torr ambient air buffer gas showing the unique mass spectra for each components 91

Figure 3.13: Mass Spectra of VOCs sampled in 1.0 Torr of ambient air showing different fragmentation patterns or signal intensities for each analyte 92

Figure 4.1: Mass spectra of hexane in 20 mTorr helium buffer gas showing improved peak widths and LMCO with increasing RF frequency 117

Figure 4.2: Mass spectra of toluene taken with 20 mTorr of helium buffer gas showing peak widths below 0.1 Da 118

Figure 4.3: Mass spectra of TEP with increasing helium buffer gas pressure at 17.2 MHz 119

Figure 4.4: Average peak widths for TEP as a function of helium buffer gas pressure for RF frequencies of 10.1 MHz, 13.6 MHz, and 17.2 MHz. 120

Figure 4.5: Ejection voltages for *p*-xylene 106 Da peak as a function of RF frequency for five microscale CITs 121

Figure 4.6: Mass spectra of *p*-xylene with increasing RF frequency and decreasing CIT dimensions with 1.0 Torr of ambient air buffer gas 122

Figure 4.7: Peak widths for *p*-xylene 106 Da as a function of RF frequency in 1.0 Torr of ambient air buffer gas from 6 to 60 MHz.....123

Figure 4.8: Mass spectra of *p*-xylene in 1.0 Torr ambient air buffer gas for a single CIT and 7-element CIT array showing a factor of 7 better signal for the CIT array 124

Figure 4.9: Mass spectra of *p*-xylenein 1.0 Torr ambient air buffer gas for a single CIT and SLIT trap showing a factor of 6 better signal for the SLIT 125

Figure 4.10: Mass spectra of *p*-xylene taken in 1.0 Torr ambient air buffer gas with 7-element CIT arrays with increasing RF drive frequency and decreasing trap dimensions.....126

Figure 4.11: Mass spectra of *p*-xylene taken in1.0 Torr ambient air buffer gas with SLITs withincreasing RF five frequency and decreasing trap dimensions 127

Figure 4.12: Peak widths for *p*-xylene as a function of RF frequency for single CITs, single SLITs, and 7-element CIT arrays in 1.0 Torr of ambient air buffer gas 128

Figure 4.13: Mass spectra of *p*-xylene at a RF frequency of 59.44 MHz with Decreasing ambient air buffer gas pressures from 1.02 Torr to 313 mTorr 129

Figure 4.14: Peak widths for *p*-xylene 106 Da peak with increasing ambient air pressures at three different RF frequencies 130

Figure 5.1: Images comparing metal and PCB electrodes showing the conductive patterning of PCB electrodes used to decrease capacitance 155

Figure 5.2: Images of PCB ion trap electrodes designed to minimize capacitance 156

Figure 5.3: Capacitance measurements for four different PCB trap configurations designed to minimize capacitance and RF power draw.....157

Figure 5.4: Mass spectra of *p*-xylene comparing signal strength for a MCIT and PCIT operated at 1.0 Torr of ambient air buffer gas.....158

Figure 5.5: Mass spectra of *p*-xylene with a r_o = 165 µm hy-MCIT with RF frequencies from 21.67 MHz to 25.07 MHz at 1.0 Torr ambient air buffer gas 159

Figure 5.6: Mass spectra of *p*-xylene for a r_o = 130 µm PCIT from 36.06 MHz to 43.96 MHz at 1.0 Torr ambient air buffer gas.....160

Figure 5.7: Peak widths for *p*-xylene 106 Da peak with increasing RF frequency for MCITs, a hy-MCIT, and a PCIT operated at 1.0 Torr of ambient air 161

Figure 5.8: Mass spectra of *p*-xylene with a x_o = 240 µm PSLIT at RF drive frequencies from 16.76 MHz to 25.76 MHz in 1.0 Tor ambient air.....162

Figure 5.9: Peak widths for *p*-xylene 106 Da peak with increasing RF frequency for MSLITs and PSLITs operated at 1.0 Torr ambient air 163

Figure 5.10: Images of the stacked PCB trap showing the two endcap and two ring electrodes, and the three insulating layers that separate them.....164

Figure 5.11: Mass spectra of *p*-xylene for the stacked PCB trap operated with a RF frequency of 19.86 MHz with 715 mTorr of ambient air 165

Figure 5.12: Schematic for the DRIE Bosch Process used to fabricate silicon ion traps.....166

Figure 5.13: Silicon ion trap images showing the physical design and sidewall smoothness from fabrication.....167

Figure 5.14: Mass spectra of *p*-xylene comparing signal strength for a MCIT and SCIT (r_o = 130 µm) operated at 1.0 Torr of ambient air 168

Figure 5.15: Mass spectra of *p*-xylene for a r_o = 225 µm hy-SCIT operated at RF frequencies from 17.90 MHz to 21.50 MHz with 1.0 Torr of ambient air buffer gas 169

Figure 5.16: Mass spectra of *p*-xylene for a r_o = 250 µm SCIT at RF drive frequencies from 15.20 MHz to 24.70 MHz with 1.0 Torr ambient air 170

Figure 5.17: Mass spectra of *p*-xylene for a r_o = 130 µm SCIT at RF drive frequencies from 15.20 MHz to 24.70 MHz with 1.0 Torr ambient air 171

Figure 5.18: Peak widths for *p*-xylene 106 Da peak with increasing RF frequency for the MCITs, a hy-SCIT, and a SCIT 172

LIST OF ABBREVIATIONS AND SYMBOLS

0-p	zero to peak
^{o}C	degrees Celsius
AC	alternating current
A.U.	arbitrary unit
BeCu	beryllium copper
C	capacitance 3.3.2
CE	capillary electrophoresis
CEES	2-chloro ethyl ethyl sulfide
CIT	cylindrical ion trap
cm	centimeter
Cu	copper
CWA	chemical warfare agent
Da	Dalton
DAPI	discontinuous atmospheric pressure interface
DC	direct current
DMMP	dimethyl methyl phosphonate
DRIE	deep reactive ion etch
ESI	electrospray ionization
eV	electron volt
FT-ICR	Fourier transform ion cyclotron resonance
FWHM	full width at half max
GC	gas chromatography

GD	glow discharge
GD-EI	glow discharge electron impact ionization
GDI	glow discharge ionization
h	hours
HCl	hydrochloric acid
HNO_3	nitric acid
HPMS	high pressure mass spectrometry
hy-MCIT	hybrid metal and circuit board cylindrical ion trap
hy-PCIT	hybrid printed circuit board cylindrical ion trap
hy-SCIT	hybrid silicon cylindrical ion trap
IMS	ion mobility spectrometry
kg	kilogram
kV	kilovolt
LC	liquid chromatography
LCD	Lightweight Chemical Detector
LCR	inductance, capacitance, and resistance
LMCO	low mass cutoff
LOD	limit of detection
MCIT	metal cylindrical ion trap
MEMS	microelectromechanical systems
MES	methyl salicylate
mm	millimeter
mHz	megahertz

MS	mass spectrometer
MSLIT	metal stretched length ion trap
mTorr	milliTorr
mV	milliVolt
mW	milliWatt
nA	nanoAmps
PCB	printed circuit board
PCIT	printed circuit board cylindrical ion trap
p-p	peak to peak
ppb	parts-per-billion
pF	picoFarad
PSLIT	printed circuit board stretched length ion trap
QIT	quadrupole ion trap
QMF	quadrupole mass filter
r	radial
RIT	rectilinear ion trap
RF	radiofrequency
r_o	radius of an ion trap
s	second
SCIT	silicon cylindrical ion trap
SEM	scanning electron microscope
SIM	soft ionization membrane
SiO_2	silicon dioxide

SLIT	stretched length ion trap
SMA	subminiature version A
S/N	signal to noise ratio
SOI	silicon-on-insulator
SWaP	size, weight, and power
Torr	unit of pressure where 760 Torr = 1 atmosphere
TEP	triethyl phosphate
TIC	toxic industrial compound
µm	micron
V	Volt
VOC	volatile organic compound
W	Watt
x_o	the radius of the small dimension for the stretched length ion trap
y_o	half-length for the long axis for the stretched length ion trap
z	axial
z_o	distance between endcap and center of trap

CHAPTER 1: INTRODUCTION TO MINIATURE MASS SPECTROMETRY AND QUADRUPOLE ION TRAPS

1.1 Motivation for Handheld Mass Spectrometers

Mass spectrometers are widely used in laboratory settings and are considered by many to be the gold standard for chemical analysis, owing to their ability to identify and quantify a wide range of chemical constituents.[1-3] Analysis times on the sub-second time scale are common, and mass spectrometers have been coupled to separation methods including gas chromatography (GC), liquid chromatography (LC), and capillary electrophoresis (CE) for improved analytical performance. Areas where mass spectrometers are used as workhorse instruments include the fields of proteomics[4], forensics[5], environmental analysis[6], and elemental composition.[7]

The sensitivity and selectivity of mass spectrometry, and the ability to perform analyses on a fast time scale makes hand-portable mass spectrometers ideal analytical instruments for field applications. Such applications include detecting volatile organic compound pollutants[8], chemical warfare agents (CWAs)[9-10], and toxic industrial compounds (TICs).[11] However, developing truly portable mass spectrometers that operate in the field with a reasonable power draw while maintaining high analytical performance has proven difficult.

Current field analysis often relies upon remote sampling and transportation to centralized laboratories where samples are analyzed with appropriate instrumentation.[12-13]

There are several tradeoffs to be considered between field measurements and transporting samples to centralized laboratories. The centralized laboratory approach minimizes the quantity of highly specialized and expensive instruments needed. Trained personnel are able to run samples and perform routine maintenance on the instruments. However, the sample transportation time to centralized laboratories can range from minutes to days which delays obtaining results. Furthermore, samples must be chemically stable over the span of time between sampling and analysis, which can prove challenging.[14] Transporting samples to the centralized location also increases analysis cost. With centralized laboratories often suffering long analysis queues, potentially up to days, along with the costs associated with shipping samples and the time-sensitive hazardous nature of potential target compounds, there is a clear need to pursue handheld instrumentation.

Handheld mass spectrometers for field applications have several challenging figures of merit. The first is the ability to detect a wide variety of compounds with varying vapor pressures at relevant concentrations. Limits of detections (LODs) in the parts-per-billion (ppb) range are also required to detect analytes at relevant concentrations. Positive identification must also be accomplished in the presence of interferences such as vehicle exhaust or cleaning agents. Low false alarm rates are required since a positive test can trigger an immediate response to a possible threat, which can be expensive and time consuming if evacuation or cleanup procedures are initiated. Long battery lifetimes are necessary in areas with limited access to electricity. This constraint requires instruments with low size, weight, and power (SWaP). Instruments also need to be rugged enough to handle extreme temperatures and physical harm requirements described in detail by existing instrument military standards (MIL-STD-810G). Finally, the instrument must be simple

enough for an untrained user to operate and maintain in a field setting.[15-16] Designing a handheld rugged instrument that meets these analytical metrics has proven difficult.

1.2 Current Handheld Chemical Instrumentation

With the need for in-the-field chemical analysis, both ion mobility spectrometry (IMS) and Raman spectrometry have been developed in truly handheld forms. For IMS, a gaseous sample is ionized and introduced into a constant electric field region within a drift tube. Ions undergo collisions as they migrate against a steady flow of drift gas (nitrogen or air) and separate based on their average velocity, which is directly proportional to the electric field applied. Ions are detected at a collector plate.[17] As an analytical technique, advantages of IMS include high sensitivity, ruggedness, low cost, and fast analysis times. Drawbacks that limit its application include poor selectivity and resolution, difficulties separating mixtures, and non-linear response with concentration. These drawbacks lead to high false alarm rates, which severely limits its suitability to serve as a reliable detector for dangerous chemicals.[18-20]

Raman spectrometry is an analytical technique that measures the vibrational characteristics of a molecule due to its chemical bonding and molecular symmetry. When a sample is irradiated with a coherent light source such as a laser, a fraction of incident radiation is scattered. While most of the scattering is elastic (Rayleigh scattering), Raman or inelastic scattering occurs when incident and scattered wavelengths are different. Stokes Raman spectra are redshifted, while Anti-Stokes spectra are blueshifted. The strength of the Raman spectra are determined by the molecular polarizability of the molecule, with a dipole moment being necessary for a molecule to be Raman active.[21] The resulting spectrum gives

a “fingerprint” of the chemical that can be used for identification. Since only a fraction of molecules have a dipole moment, Raman spectrometry is fundamentally limited in the number of target molecules it can determine. Although chemical libraries are still possible, long signal averaging times are required to overcome poor sensitivity and high background signal. This long signal averaging severely limits its applicability where sub-second detection with minimal false alarm rates are required such as in safety and security applications.

Although lacking in sensitivity, handheld Raman spectrometers are useful as a non-invasive and non-destructive method, especially for white powder explosives and colorless liquids. Samples can be analyzed through many clear and colored plastic and glass containers limiting exposure of first responders to potentially harmful samples.[22] Sample identification is limited by requiring the analyte to be Raman active, long signal averaging, large sample size requirements, and background interferences such as fluorescence.[21, 23]

Truly handheld forms of IMS have been realized for several decades. An early example includes the Lightweight Chemical Detector (LCD) by Graseby Dynamics Limited Company reported in 1988.[24] It has dimensions of 18 x 8 x 4 cm and has a total weight of 0.6 kg and operates on a battery for approximately 40 h. More recently, Smiths Detection released the LCD 3.3 handheld IMS in 2009, which has dimensions of 10.54 x 17.3 x 4.65 cm, weighs 0.65 kg and has battery lifetimes ranging from 40 to 75 h. Ongoing challenges for handheld IMS instruments that limit its field use include chemical selectivity, limited duty cycle, low ionization sampling volume, and the operating temperature of the instrument.[19, 25]

Handheld Raman spectrometers have become readily available commercially in the past decade, largely aided by recent developments in miniature lasers. The First Defender by Ahura Scientific was announced in 2005. It has dimensions of 19.3 x 10.7 x 4.4 cm, weighs 1.8 kg, and has a 5 hour battery lifetime with a library of over 500 hazardous solids and liquids.[26] Another handheld Raman spectrometer is the DeltaNu Inspector Raman which has also been available for over a decade and has a similar mass of 1.9 kg.[27] Recent challenges for handheld Raman spectrometers have included sensitivity and the development of optics that have performance similar to benchtop counterparts while maintaining ruggedness.[28] While the current handheld instruments are largely limited by selectivity (IMS) and sensitivity (Raman), mass spectrometry can address both limitations.

1.3 Portable Mass Spectrometry

There have been numerous attempts to miniaturize mass spectrometers to form factors comparable to the previously described IMS and Raman handheld instruments. These efforts have been based primarily on miniaturizing the component parts of laboratory-based mass spectrometers such as vacuum pumps, traps and electronics. As a result, current portable mass spectrometry technologies are typically suitcase size in the 13-45 kg range and are more luggable than portable. Examples of such instruments include the Guardion-7 and the HAPSITE chemical identification system.[29-31] The Guardion-7 has dimensions of 47 x 36 x 18 cm, weighs 13 kg and runs 50-100 analyses between maintenance.[32-33] In comparison, the HAPSITE chemical identification system has dimensions of 46 x 43 x 18 cm, weighs 16 kg, and has a battery life of 2-3 hours.[34] These instruments have impractical weights for a truly handheld device.

The main limiting factors in developing a portable or miniature mass spectrometer are the vacuum and power requirements primarily associated with the turbopump needed to reach operational pressures. The target power budget for a handheld instrument is approximately 25 W[35] but can vary with instrumental operational lifetime needs. For a handheld mass spectrometer approximately 25 W of power draw would be acceptable for operational times exceeding 4 hours. The power required to run a turbopump is a significant drain on battery lifetime, which presents a problematic tradeoff between battery size and weight, and instrument run time. Even next generation miniaturized turbopumps under development are estimated to draw at least 4 W, a significant fraction of the power budget (16 %) for a handheld instrument of approximately 25 W. An additional pumping challenge is the lack of mechanical stability and ruggedness of a miniature turbopump operating in the field.[36] Eliminating the turbopumps would significantly decrease the size, weight, and power (SWaP) requirements, and reduce the cost of an instrument.

While eliminating the need for turbopumps is ideal, there have been other efforts to alleviate pumping and power requirements associated with miniature spectrometers. Discontinuous atmospheric pressure interface (DAPI) bridges the pressure gap by pulsing in a gas load from atmosphere and then pumping down to pressures suitable for mass analysis. Shortcomings of this strategy include increased analysis time and still requires a turbopump to reach the target pressure.[36-37] Examples of instruments that use DAPI for analysis include the Mini 11 and Mini 12 from Purdue University, and Palm-Portable Mass Spectrometer from the Sam Yang Chemical Company.[38-41] When DAPI was first introduced in the Mini 10 mass spectrometer the pumping system drew 18 W. This is 72% of the targeted power

budget, demonstrating why for truly handheld instrumentation eliminating turbopumps yields the largest gain in terms of SWaP.[37]

By eliminating the turbopump and operating at elevated pressures in excess of 100 mTorr, each fundamental component of the mass spectrometer including the ionization source, mass analyzer, and detector must be operational at elevated pressures. Ionization sources have been widely used at ambient pressures for over a decade.[42-43] While ionization sources will require optimization for high pressure mass spectrometry (HPMS), the fundamental technology exists. For detection, electron multipliers are widely used for low pressure detection, while Faraday cup detectors can be operated independently of pressure.[44-45] Faraday cup detectors have less sensitivity and sampling bandwidth than electron multipliers, but are also a well-developed technology and can be optimized for HPMS.

Mass analyzers remain undeveloped for high pressure operations, and are a primary research area for HPMS. There have been efforts to miniaturize most mass analyzers to smaller form factors including time of flight [46-47], magnetic sectors[48], Fourier transform ion cyclotron resonance (FT-ICR)[49], quadrupole mass filters (QMFs)[50], and quadrupole ion traps (QITs)[51]. Of these mass analyzers, only QITs and QMFs have performance metrics that scale favorably with smaller critical dimensions and higher operating conditions, which are necessary to minimize SWaP requirements.

Traditional quadrupole mass filters (QMFs) and quadrupole ion traps (QITs) operate at approximately 1 millitorr (mTorr), which is at least several orders of magnitude higher than other mass analyzers. Thus, even with minimal pressure scaling, vacuum requirements are reduced compared to other mass analyzers.[52-53] There are tradeoffs between QMFs and

QITs as mass analyzers. Since they are not trapping instruments, QMFs are well-suited for detecting low mass ions[50] while QITs are more sensitive to analytes that are several times larger than the buffer gas. A critical drawback for QMFs is the tight dimensional tolerances required to fabricate and align the quadrupole rods on the microscale.[54-55]

Another potential benefit of using QMFs and QITs is the capability of performing tandem mass spectrometry. Tandem mass spectrometry is a simple, well-developed method for gaining the maximum chemical information from a compound, and can greatly enhance an instrument's ability to handle complex samples.[56] QMFs are only capable of tandem mass spectrometry in space, not time and require multiple mass analyzers, fundamentally increasing the size and weight of the instrument.[57] QITs on the other hand are capable of tandem mass spectrometry in time so an increase in trap size is unnecessary adding functionality to a hand portable instrument.

1.4 Quadrupole Ion Trap Background

The QIT mass analyzer (Figure 1.1) was first reported by Paul and Steinwedel in 1953.[58] It consists of three hyperbolic electrodes: a central ring electrode separated from two endcap electrodes by insulating material, examples of which includes Teflon, Kapton, and ceramic. Critical dimensions that determine operational characteristics for the trap include the radius of the ion trap r_o and the distance from the center of the trap to the endcap electrode z_o. Ions enter and exit the ion trap axially through apertures or meshes in the two endcap electrodes. A radio frequency (RF) potential applied to the ring electrode creates a quadrupolar electric field that traps ions in stable axial (z) and radial (r) trajectories. Ions

eject from the ion trap through the endcap electrodes when their motion becomes unstable in the z dimension.[52, 59]

1.4.1 Mass Analysis by QITs

There has been significant development in understanding the motion of trapped ions and the different methods for performing and optimizing mass analysis. Stable ion motion in a quadrupolar, alternating field is described by the Mathieu equation.[60] The dimensionless parameters a_z and q_z define stable or unstable trajectories in the z-dimension, while a_r and q_r define motion in the r-dimension. The equations for each of these parameters are defined by equations 1.1 through 1.4,

$$a_z = -\frac{16eU}{m(r_o^2 + 2z_o^2)\Omega^2} \tag{1.1}$$

$$a_r = \frac{8eU}{m(r_o^2 + 2z_o^2)\Omega^2} \tag{1.2}$$

$$q_z = \frac{8eV}{m(r_o^2 + 2z_o^2)\Omega^2} \tag{1.3}$$

$$q_r = \frac{-4eV}{m(r_o^2 + 2z_o^2)\Omega^2} \tag{1.4}$$

where U is the DC voltage applied to the ring electrode, V is the zero-to-peak (0-p) RF voltage applied to the ring electrode, Ω is the angular frequency of the RF signal applied to the ring electrode, e is the elementary charge, m is the mass of the ion, r_o is the trap radius, and $2z_o$ is the distance between the two endcap electrodes.[52] While ion motion was well-

characterized by early work, the more challenging problem was developing and optimizing methods for performing mass analysis by ejecting the ions. The original method described by Paul and Steinwedel for mass analysis was called resonant detection.[61] With this method a small alternating current (AC) voltage was applied between the two endcap electrodes in addition to AC and DC trapping voltages to resonantly eject ions when their axial frequency of motion matched the endcap excitation frequency.[61] Later, Dawson and Whetten developed mass selective storage where ions were trapped one m/z value at a time based on carefully chosen AC and DC voltages, and subsequently ejected by applying a DC pulse between the endcap electrodes.[62]

The previous two methods of mass analysis have overwhelmingly been replaced by mass selective instability operation, developed by Stafford and coworkers at Finnigan MAT Corporation and the University of Kent.[63] Figure 1.2 shows the stability diagram for a QIT as a function of the a_z and q_z parameters. Ions are trapped with stable trajectories provided their trapping parameters β_r and β_z (complex trapping functions related to a_z and q_z)[53] fall within the 0-1 range (shaded orange). With this method, no DC voltage is applied to the ring electrode so q_r and a_r equal zero. The stability of the trapped ions is determined by q_z, which is stable for all values below 0.908 (red line). Another important consideration is the mass range of ions that can be ejected. Rearranging equation 1.3 for mass range (m/e),

$$\frac{m}{e} = \frac{8V}{q_z(r_o^2 + 2z_o^2)\Omega^2} \tag{1.5}$$

shows ions can be ejected as a function of m/z by varying V, Ω, and the QIT dimensions until an unstable q_z value is reached. For a given QIT, ions can be mass analyzed with increasing mass by ramping the V at a fixed Ω until they are ejected when $q_z > 0.908$. The

RF drive frequency can also be ramped, although that is uncommon since resonant circuits tuned for a specific frequency are used to increase efficiency of the RF generation process.

1.4.2 Mass Resolution for QITs

So far, the treatment of the ion trap has focused on ideal hyperbolic ion traps without considerations for background or buffer gas pressure. Since the goal of handheld mass spectrometry is high pressure operation, understanding these pressure effects are critical. Ion traps were first operated at very low pressures, around 10^{-6} Torr, to minimize ion-neutral collisions that could affect ion motion and cause peak broadening. Since there was considerable interest in using QITs as GC detectors, Stafford and coworkers increased the helium buffer gas pressure in their r_o = 1 centimeter (cm) QIT from approximately 10^{-6} Torr to 10^{-2} Torr.[63] Mass resolution was studied as a function of increasing helium pressure focusing on the perfluroro tributyl amine (PFTBA) mass-to-charge (m/z) 69 and m/z 502 peaks. An improvement in mass resolution with pressure up to approximately 1 mTorr was seen. They suggested that increased helium gas pressure caused collisional dampening of ion motion towards the center of the QIT, resulting in better-defined secular motion of the trapped ions and ejection from the ion trap in a tighter time span, improving mass resolution.[63-64]

The effect of buffer gas pressure on peak widths was theoretically studied by Goeringer and coworkers.[65] A damping factor accounting for the effect of ion-neutral collisions was added to the Mathieu equation. Equation 1.6 shows the relationship between the peak width and ion mass ($\Delta m/m$), pressure (P), collisional relaxation time (τ), and Ω.

$$\frac{\Delta m}{m} \propto \frac{P}{\Omega} = \frac{4\sqrt{3}}{\Omega\tau} \quad (1.6)$$

This shows peak widths scale linearly with increased pressure and inversely with RF drive frequency. The effect of increasing the RF frequency causes ions to experience more RF cycles per ion-neutral collision. More frequent RF cycles contain the ions near the center of the ion trap and increase the secular frequency of motion. When operating pressures increase for a fixed RF drive frequency, the mean free path decreases proportionally. This higher pressure causes more frequent ion-neutral collisions to occur. These collisions cause an increase in ion trajectories from the center of the trap and ions are ejected over a wider time range for the same m/z value resulting in increased peak widths. Therefore, the RF frequency needs to be scaled proportionally in order to prevent peak width broadening as the operating pressure increases.

Building off Equation 1.6, Whitten *et al.* addressed scaling RF drive frequency and decreasing trap sizes with collisional frequency up to a factor of 1,000 compared to traditionally sized QITs.[66] They determined that with correct scaling of parameter space, mass resolution should remain constant with higher operating pressure. While the mass resolution for a QIT fundamentally does not depend on the operating pressure, there remain practical limitations for miniaturizing QITs such as fabrication tolerances, power requirements, and surface roughness that affect their usefulness.[66-67]

1.4.3 Sensitivity for QITs

When increasing the RF drive frequency to maintain mass resolution at higher pressures, there are practical limits to the RF voltage that can be applied. One is the limits on generating the necessary voltages with miniaturized RF amplifiers and the other is the risk of

electrical breakdown with smaller electrode separations.[63, 68] To overcome these limitations, the critical ion trap dimensions can be decreased proportionally to maintain reasonable voltage requirements. Smaller QITs and lower trapping voltages however scale proportionally with sensitivity, which presents challenges since LODs in the part-per-billion range are needed.

The Dehmelt pseudopotential well depth (D_z) calculates how much kinetic energy ions can have and still remained trapped by a QIT. D_z is calculated based on ion motion following the characteristics of a harmonic oscillator in the z-dimension. Equation 1.7 defines D_z under the Dehmelt approximation conditions where $q_z < 0.4$.[69]

$$D_z = \frac{eV^2}{4mz_0\Omega^2} = \frac{q_z V}{8} \tag{1.7}$$

As seen in Equation 1.7, D_z decreases linearly with voltage, which results in signal loss when RF drive voltages are lowered. Fundamentally, D_z must be above thermal energy for a QIT to operate.

The number of ions that can be stored in an ion trap (N_{max}) is dependent on D_z and the critical dimensions of the QIT. Equation 1.8 describes the relationship between N_{max}, z_o, and D_z for a QIT.[69]

$$N_{max} = 2.8x10^7 D_z z_0 \tag{1.8}$$

Fundamentally, ion storage capacity decreases linearly with z_o, resulting in additional signal loss for miniaturized ion traps. Since miniaturized ion traps are traditionally operated with a lower D_z, there are further losses in sensitivity beyond simple miniaturization. To address the sensitivity losses with miniaturization, planar ion trap arrays are used to increase signal

strength proportionally to the number of array elements. Mass spectra from arrays with up to 256 elements have been demonstrated in the literature.[67] For charge capacity, ion trap arrays scale beneficially with miniaturization since charge capacity scales with radius while surface areas scales as r^2 and volume decreases as r^3, thus more ions are stored in the same footprint as a conventional sized ion trap.[67, 69] Fabrication tolerances have limited the number of array elements that have been demonstrated, although there is no fundamental limit on the number of array elements. For highly miniaturized ion traps, there are significant questions regarding whether signal strength can be recovered proportionally to the number of trap elements where dimensional tolerances begin to limit mass resolution.

1.4.4 Simplified Ion Trap Geometries

From Equation 1.6, the need to increase the RF drive frequency to improve mass resolution at high pressures is clear. However, while peak widths scale with the inverse of the RF frequency, mass range scales inversely with the RF frequency squared. In order to maintain a practical mass range for analytical applications when using high RF frequencies, ion traps with smaller dimensions, most probably on the microscale, are required.[53, 65] Currently, reproducible manufacturing of hyperbolic ion traps on the microscale is difficult and expensive. These limitations have led to the development of simplified ion trap geometries that can be fabricated on the microscale.

Several examples of simplified geometries in the literature include multi-ring stacks, the toroidal ion trap, rectilinear ion trap, and the halo ion trap.[32, 70-73] One of the mostly widely developed simplified geometries and most applicable for our purposes is the cylindrical ion trap (CIT) shown in Figure 1.3. This geometry simplifies fabricating

miniaturized ion traps by replacing the hyperbolic electrodes with planar electrodes.[74] CITs on the millimeter (mm) to micron (μm) scale have been demonstrated by multiple research groups.[75-76] They have been widely used since planar electrodes can be fabricated by many conventional fabrication methods such as mechanical milling in addition to microfabrication techniques. There have been concerns about potential mass resolution losses resulting from the simplified CIT geometry but mass resolutions comparable to those of commercial instruments have been reported.[74, 77]

Simplified geometries have also been used to offset the sensitivity losses from ion trap miniaturization. As discussed previously, signal increases proportionately to the number of CITs in an array. However, mass resolution can be lost if ion trap arrays are not fabricated with tight dimensional tolerances. One area of research has been novel ion trap geometries that could minimize the need for large ion trap arrays traditionally used to improve sensitivity for microscale traps. Figure 1.4 compares the end-on structure of the CIT (Figure 1.4a) to one such novel ion trap geometry, the stretched length ion trap (SLIT) (Figure 1.4b). The SLIT replaces the cylindrical feature with a slot that stretches along the y-plane increasing ion-trapping capacity and reducing ejection-timing concerns from multiple traps in a CIT array.

Sensitivity for SLITs has been shown to be an order of magnitude better than a CIT, and it scales proportionally to the length of the SLIT feature.[78] Arrays of SLITs and a serpentine geometry are both possible to further improve sensitivity. A key challenge for microscale ion trap arrays is dimensional tolerances between array elements since fabrication imperfections on the 10s of microns scale can significantly influence trapping. SLITs reduce

the number of array elements required for the same sensitivity as a corresponding CIT, significantly reducing fabrication tolerances.

1.4.4 Higher Order Field Components

The hyperbolic QIT was developed with an emphasis on producing trapping fields that are as close to a pure quadrupole as possible. However, higher order fields are created in ion traps by incorporating entrance and exit apertures required to introduce and detect the analyte.[79] Miniaturized ion traps with simplified geometries are also characterized by a combination of higher order field components and non-linear resonances that significantly influence trapping. Higher order fields historically have been difficult to understand theoretically, but have powerful effects on trap operation. Franzen and coworkers have developed an expression (Equation 1.9) to include contributions from different field components of the electric field at a given location within the ion trap ($\Phi_{r,z}$) compared to the overall applied electric field (Φ).[80-81]

$$\phi_{r,z} = \phi_o \left(A_2 \frac{r^2 - 2z^2}{2r_o^2} + A_3 \frac{3r^2z - 2z^3}{2r_o^3} + A_4 \frac{3r^4 - 24r^2z^2 + 8z^4}{8r_o^4} + A_5 \frac{15r^4z - 40r^2z^3 + 8z^5}{8r_o^5} + A_6 \frac{5r^6 - 90r^4z^2 + 120r^2z^4 - 16z^6}{16r_o^6} \ldots \right) \quad (1.9)$$

The coefficients A_2 through A_6 correspond to weighting factors for multipole components including quadrupole, hexapole, octapole, decapole, and dodecapole.

For a perfect QIT, only A_2 contributes to the field component with all other coefficients zero. In real traps there are higher field components in addition to the

quadrupole component. However, the quadrupolar is the strongest field and dominates trap behavior, while providing a linear restoring force with distance from the center of the trap. Higher order components are strongest near the boundaries of the trap, and decrease non-linearly with distance towards the center where ions predominantly reside. Thus, the higher order fields have effects on ion motion, although significantly less than the quadrupolar field.[79]

There are several ways higher order field components can be used to improve QIT performance. A 10.8% stretch in z_o was used by Finnigan Corporation to compensate for mass shifts observed in their mass spectra.[79] Double resonant ejection with higher order field components can be used to improve both mass resolution and mass range.[82] While ion traps typically eject ions at a q_z of 0.908 in mass instability scans, a supplemental (axial) RF voltage can be applied to a single endcap or across the endcap electrodes to resonantly excite the ions at a lower q_z value. Miniature ion traps use double resonant ejection efficiently since they have large higher order field components near the trap boundaries, and have less well-defined ion ejection points from the quadrupole field alone. Theoretical and experimental studies are necessary to ensure higher order fields are used effectively for optimal mass resolution.[73, 83-84]

1.5 High Pressure Mass Spectrometry

Based on the previously presented theory, operation of an ion trap at elevated pressure should be possible, provided ion traps are significantly miniaturized to micron dimensions and operated at elevated RF drive frequencies. The capability of applying higher RF drive frequencies to ion traps with reduced dimensions has been demonstrated but not

under high pressure conditions above 100 mTorr.[51] CITs with critical dimensions of 2.5 and 1.5 mm have been demonstrated at RF frequencies of 2.0 and 2.7 MHz, up from the typical 1 MHz drive RF used with 1 cm traps.[63, 75] When CITs were further miniaturized to 1 mm the RF frequency was scaled to 2.8 MHz.[71] For microscale ion traps with a radius of 500 μm, mass spectral analysis has been performed with RF drive frequencies above 3.0 MHz.[76] Fundamental studies of this CIT size including double resonance ejection, limits of detection, and sample pressure effects have been studied with the drive RF scaled to near 8 MHz.[82, 85-86]

Efforts have also been undertaken to significantly decrease ion trap sizes to the micron level and take advantage of microfabrication techniques such as deep reactive-ion etching (DRIE). Pau and coworkers demonstrated operation of r_o = 20 μm CIT arrays (256 and 2304 elements) fabricated from p-doped polysilicon with silicon dioxide insulating layers. Xenon gas was detected at 10^{-4} Torr of helium pressure with 1% analyte gas.[67] Arrays with up to 10^6 elements of r_o = 1 μm CITs were fabricated by others. Mass analysis was not demonstrated with these traps, but practical considerations concerning fabrication and operation under these extremely miniaturized conditions were discussed.[87] Further investigation into the 1 μm CITs covered geometry, space charge, and buffer gas effects.[88] They concluded that Coulombic repulsions would result in a single ion being trapped in each array element after 1 μs and that trap geometry would only have minor effects on ion ejection at these dimensions.

Several efforts have been made to increase buffer gas pressure beyond the traditional 1 mTorr regime. Recent high-pressure studies from Xu *et al.* utilizing a RIT instrument predicted full width half max (FWHM) peak widths of 9.5 Da operating with air buffer gas at 250 mTorr.[89] Experimental results by Song *et al.* using a RIT configuration demonstrated

FWHM peak widths of 0.98 Da at 4.1 mTorr air buffer gas with an increase to 2.00 Da at 50 mTorr.[90] The studies by Song *et al.* and Xu e*t al.* that explored mass analysis at high pressures up to 250 mTorr used similar RF drive frequencies as commercial instrumentation (1 MHz) so an improvement in mass resolution was not expected.[89-90] Advantages of maintaining the 1 MHz drive RF included simplified RF electronics while maintaining high mass range and low voltages. The lower voltages are a tradeoff between RF voltages and sensitivity since they result in a lower pseudopotential well depth and sensitivity.[91-92] While operation under these conditions represented significant progress towards high pressure operation, combining elevated pressures and RF drive frequencies were not explored.

1.6 Objectives

Although the theoretical background behind high pressure mass spectrometry (HPMS) was developed over two decades ago, ion trap operation under those conditions has proved elusive. While HPMS has been defined as pressures above 100 mTorr, a target pressure of 1 Torr was set for this work making turbopumps unnecessary and portable instrumentation feasible with miniaturized roughing pumps. The pressure range from 100 mTorr to 1 Torr was also explored as further vacuum pump advances could alleviate the SWaP tradeoffs of operating at lower pressures without any compromise in analytical capabilities.

The objectives of this project were four-fold. The first experimental goal was to determine operating conditions for HPMS with helium as the buffer gas while characterizing mass resolution as a function of buffer gas pressure (Chapter 2). To accomplish this, relevant analytes including volatile organic compounds (VOCs) and CWA simulants related to safety

and security applications were analyzed. Since the ionization source must also tolerate high pressure operation with microscale CITs, a goal was also to develop ionization sources. Metrics include operation at 1 Torr, how well mass resolution is maintained with pressure, and SWaP parameters with an eye towards inclusion in a portable device.

The second goal was to develop HPMS operation with nitrogen and air buffer gases as both are readily available in field environments reducing size and weight concerns compared with bottled helium (Chapter 3). This buffer gas change requires further development of oxygen tolerant ionization sources and integration with a CIT. As with helium, the effects of buffer gas pressure on mass resolution are explored. Since significant mass resolution losses are anticipated with nitrogen and air buffer gases compared to helium, the resolution effects of increasing the RF drive frequency and ion trap miniaturization with 1 Torr ambient air buffer gas were investigated (Chapter 4). To offset the decrease in sensitivity due to trap size reduction, methods for regaining sensitivity including CIT arrays and SLIT traps were characterized for sensitivity and potential mass resolution loss.

The final goal was to characterize ion traps fabricated from materials with potential advantages over metal traps used for initial development work (Chapter 5). Printed circuit board (PCB) electrodes were studied since they easily lower ion trap capacitance and scale well for cost. Silicon electrodes fabricated by DRIE were studied since DRIE offers high dimensional control on the microscale. The sensitivity and mass resolution of both materials were studied and compared to metal electrodes to determine experimental tradeoffs between materials at the microscale.

1.7 Figures

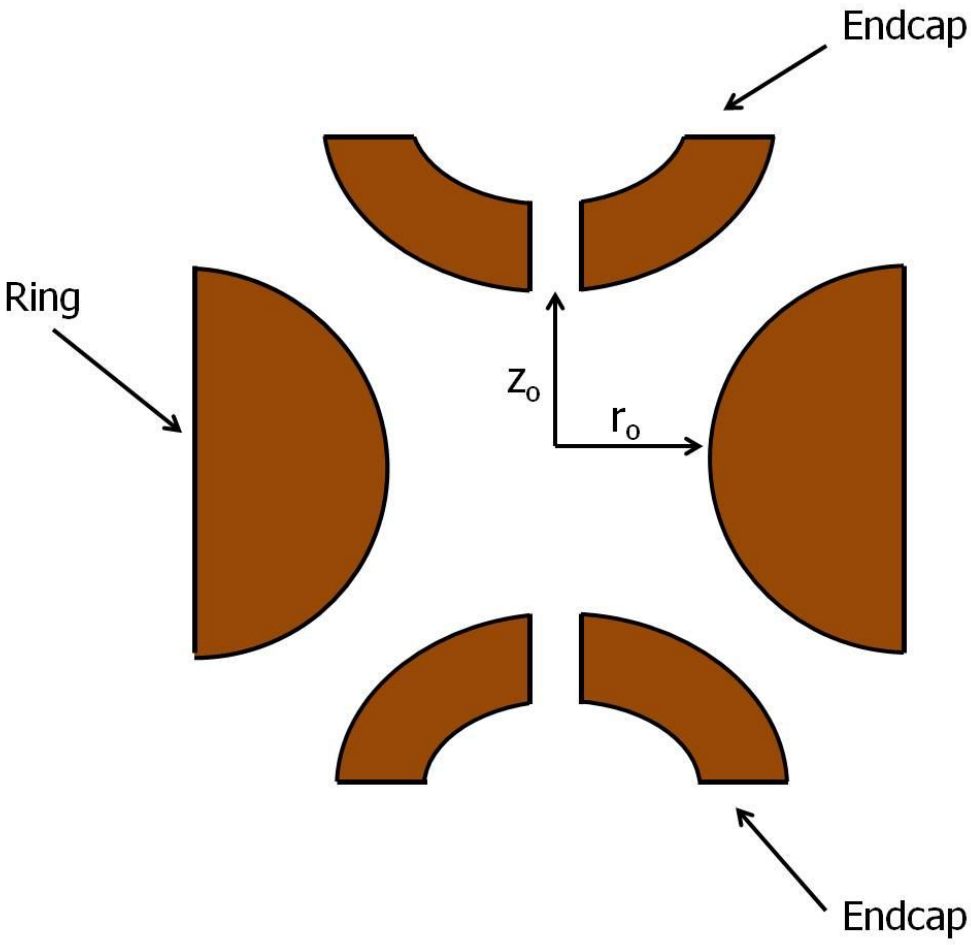

Figure 1.1: Schematic for a quadrupole ion trap. The center hyperbolic ring electrode is electrically isolated from the endcap electrodes. The critical dimensions r_o and z_o correspond to the radius of the ring electrode and the separation between the center of the ring electrode and the endcap electrodes.

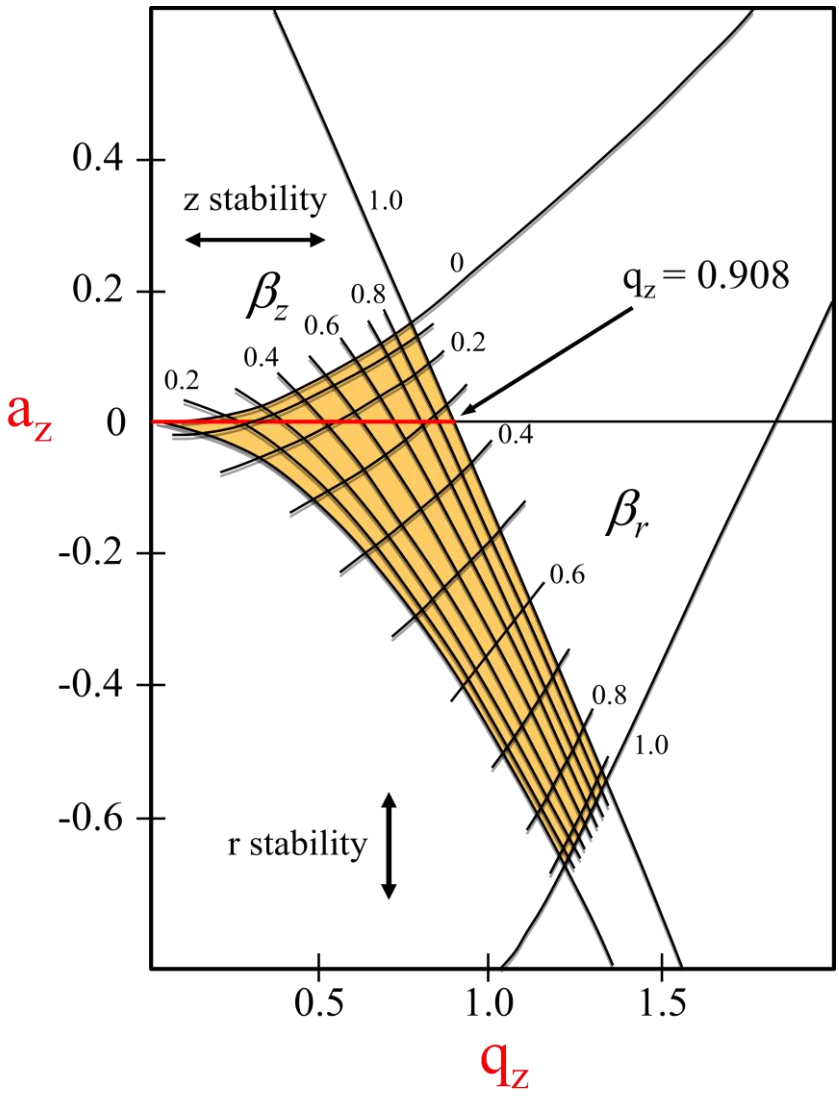

Figure 1.2: Stability Diagram for a QIT. Ions are trapped within the trapping parameters β_z and β_r region (shaded orange) and ion ejection for standard mass instability scans with no DC voltage applied (red line) occurring when q_z reaches 0.908.

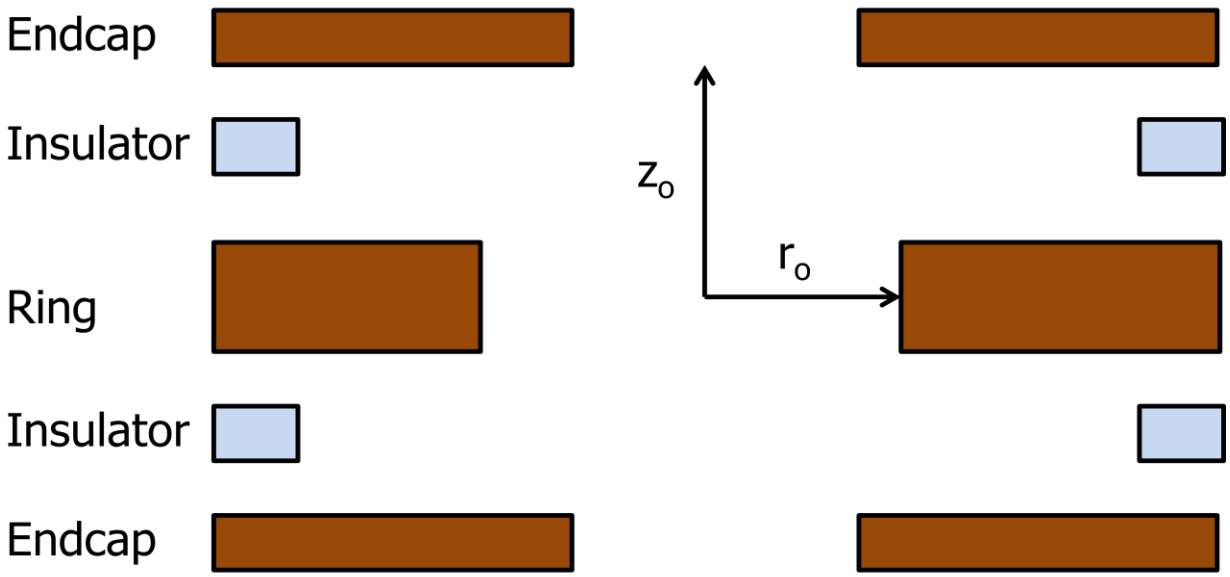

Figure 1.3: Schematic for a cylindrical ion trap. The geometry is simplified from hyperbolic to planar for ease of fabrication when the critical dimensions are reduced, especially to the microscale.

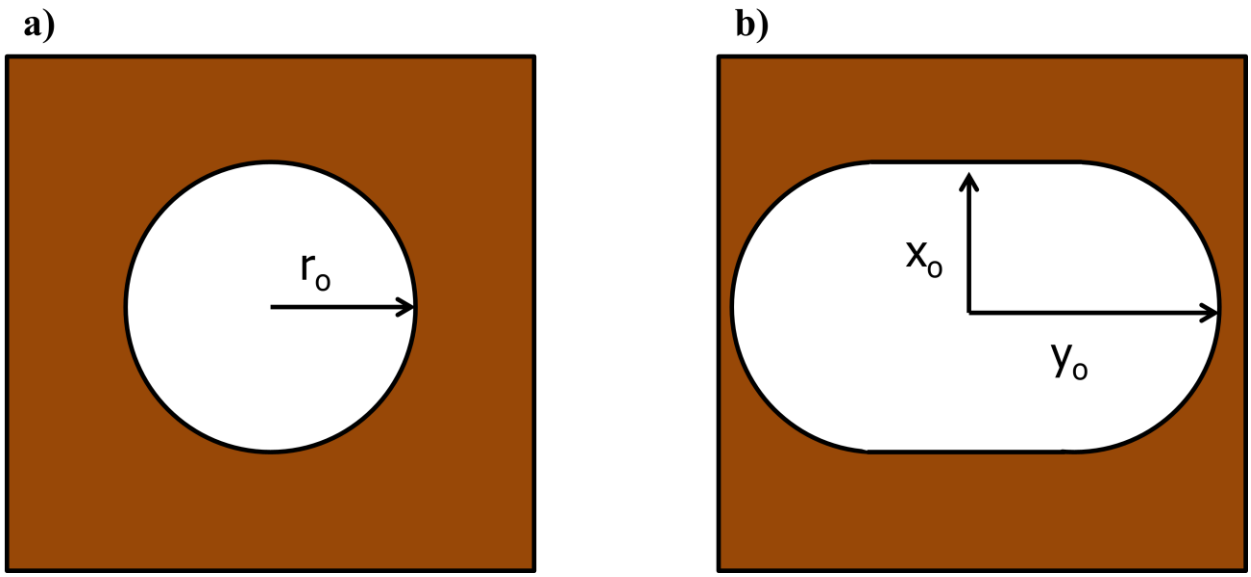

Figure 1.4: Top view of ion trap configurations for a) CIT and b) a SLIT geometry used to increase sensitivity proportionally by the length of the SLIT feature y_o where $r_o = x_o$.

1.8 References

1. Ong, S. E.; Mann, M., Mass spectrometry-based proteomics turns quantitative. *Nature Chemical Biology* **2005,** *1* (5), 252-62.

2. Maurer, H. H., Current role of liquid chromatography-mass spectrometry in clinical and forensic toxicology. *Analytical and Bioanalytical Chemistry* **2007,** *388* (7), 1315-1325.

3. Stanczyk, F. Z.; Clarke, N. J., Advantages and challenges of mass spectrometry assays for steroid hormones. *The Journal of Steroid Biochemistry and Molecular Biology* **2010,** *121* (3-5), 491-5.

4. Nguyen, D. N.; Becker, G. W.; Riggin, R. M., Protein mass-spectrometry - applications to analytical biotechnology. *Journal of Chromatography A* **1995,** *705* (1), 21-45.

5. Ifa, D. R.; Jackson, A. U.; Paglia, G.; Cooks, R. G., Forensic applications of ambient ionization mass spectrometry. *Analytical and Bioanalytical Chemistry* **2009,** *394* (8), 1995-2008.

6. Santos, F. J.; Galceran, M. T., Modern developments in gas chromatography-mass spectrometry-based environmental analysis. *Journal of chromatography A* **2003,** *1000* (1-2), 125-51.

7. Marshall, A. G.; Hendrickson, C. L.; Jackson, G. S., Fourier transform ion cyclotron resonance mass spectrometry: A primer. *Mass Spectrometry Reviews* **1998,** *17* (1), 1-35.

8. Tang, H. P. O., Recent development in analysis of persistent organic pollutants under the Stockholm Convention. *Trac-Trends in Analytical Chemistry* **2013,** *45*, 48-66.

9. Noort, D.; Benschop, H. P.; Black, R. M., Biomonitoring of exposure to chemical warfare agents: A review. *Toxicology and Applied Pharmacology* **2002,** *184* (2), 116-126.

10. Kientz, C. E., Chromatography and mass spectrometry of chemical warfare agents, toxins and related compounds: state of the art and future prospects. *Journal of Chromatography A* **1998,** *814* (1-2), 1-23.

11. Castillo, M.; Barcelo, D.; Pereira, A. S.; Neto, F. R. A., Characterization of organic pollutants in industrial effluents by high-temperature gas chromatography mass spectrometry. *Trac-Trends in Analytical Chemistry* **1999,** *18* (1), 26-36.

12. Kesselmeier, J.; Kuhn, U.; Wolf, A.; Andreae, M. O.; Ciccioli, P.; Brancaleoni, E.; Frattoni, M.; Guenther, A.; Greenberg, J.; Vasconcellos, P. D.; de Oliva, T.; Tavares, T.; Artaxo, P., Atmospheric volatile organic compounds (VOC) at a remote tropical forest site in central Amazonia. *Atmospheric Environment* **2000,** *34* (24), 4063-4072.

13. Yassaa, N.; Meklati, B. Y.; Brancaleoni, E.; Frattoni, M.; Ciccioli, P., Polar and non-polar volatile organic compounds (VOCs) in urban Algiers and saharian sites of Algeria. *Atmospheric Environment* **2001,** *35* (4), 787-801.

14. Ras, M. R.; Borrull, F.; Marce, R. M., Sampling and preconcentration techniques for determination of volatile organic compounds in air samples. *Trac-Trends in Analytical Chemistry* **2009,** *28* (3), 347-361.

15. Steinfeld, J. I.; Wormhoudt, J., Explosives detection: a challenge for physical chemistry. *Annual Review of Physical Chemistry* **1998,** *49,* 203-32.

16. Nambayah, M.; Quickenden, T. I., A quantitative assessment of chemical techniques for detecting traces of explosives at counter-terrorist portals. *Talanta* **2004,** *63* (2), 461-467.

17. Hill, H. H., Jr.; Siems, W. F.; St Louis, R. H.; McMinn, D. G., Ion mobility spectrometry. *Analytical Chemistry* **1990,** *62* (23), 1201A-1209A.

18. Eiceman, G. A.; Stone, J. A., Ion mobility spectrometers in national defense. *Analytical Chemistry* **2004,** *76* (21), 390a-397a.

19. Hill, H. H.; Simpson, G., Capabilities and limitations of ion mobility spectrometry for field screening applications. *Field Analytical Chemistry and Technology* **1997,** *1* (3), 119-134.

20. Li, F.; Xie, Z.; Schmidt, H.; Sielemann, S.; Baumbach, J. I., Ion mobility spectrometer for online monitoring of trace compounds. *Spectrochimica Acta Part B-Atomic Spectroscopy* **2002,** *57* (10), 1563-1574.

21. Moore, D. S.; Scharff, R. J., Portable Raman explosives detection. *Analytical and Bioanalytical Chemistry* **2009,** *393* (6-7), 1571-1578.

22. Eliasson, C.; Macleod, N. A.; Matousek, P., Noninvasive detection of concealed liquid explosives using Raman spectroscopy. *Analytical Chemistry* **2007,** *79* (21), 8185-8189.

23. Izake, E. L., Forensic and homeland security applications of modern portable Raman spectroscopy. *Forensic Science International* **2010,** *202* (1-3), 1-8.

24. Taylor, S. P., J. P., Conner, J. A., FitzGerald, J., Adams, J. H., Harden, Ch.C., Shoff, D. B., Davis, D. M., Ewing, R. G., Design aspects and operation characteristics of the lightweight chemical detector. *International Society for Ion Mobility Spectrometry* **1998,** *1* (1), 58-63.

25. Xu, J.; Whitten, W. B.; Ramsey, J. M., Pulsed-ionization miniature ion mobility spectrometer. *Analytical Chemistry* **2003,** *75* (16), 4206-4210.

26. Santillan, J. D.; Brown, C. D.; Jalenak, W., Advances in raman spectroscopy for explosive identification in aviation security - art. no. 65400P. *Optics and Photonics in Global Homeland Security III* **2007,** *6540*, P5400-P5400.

27. Jehlicka, J.; Vitek, P.; Edwards, H. G. M.; Hargreaves, M.; Capoun, T., Application of portable Raman instruments for fast and non-destructive detection of minerals on outcrops. *Spectrochimica Acta Part a-Molecular and Biomolecular Spectroscopy* **2009,** *73* (3), 410-419.

28. Cullum, B. M.; Mobley, J.; Chi, Z. H.; Stokes, D. L.; Miller, G. H.; Vo-Dinh, T., Development of a compact, handheld Raman instrument with no moving parts for use in field analysis. *Review of Scientific Instruments* **2000,** *71* (4), 1602-1607.

29. Ouyang, Z.; Noll, R. J.; Cooks, R. G., Handheld miniature ion trap mass spectrometers. *Analytical Chemistry* **2009,** *81* (7), 2421-2425.

30. Geear, M.; Syms, R. R. A.; Wright, S.; Holmes, A. S., Monolithic MEMS quadrupole mass spectrometers by deep silicon etching. *Journal of Microelectromechanical Systems* **2005,** *14* (5), 1156-1166.

31. Hendricks, P. I.; Dalgleish, J. K.; Shelley, J. T.; Kirleis, M. A.; McNicholas, M. T.; Li, L.; Chen, T. C.; Chen, C. H.; Duncan, J. S.; Boudreau, F.; Noll, R. J.; Denton, J. P.; Roach, T. A.; Ouyang, Z.; Cooks, R. G., Autonomous in situ analysis and real-time chemical detection using a backpack miniature mass spectrometer: concept, instrumentation development, and performance. *Analytical Chemistry* **2014,** *86* (6), 2900-8.

32. Lammert, S. A.; Rockwood, A. A.; Wang, M.; Lee, M. L.; Lee, E. D.; Tolley, S. E.; Oliphant, J. R.; Jones, J. L.; Waite, R. W., Miniature toroidal radio frequency ion trap mass analyzer. *Journal of the American Society for Mass Spectrometry* **2006,** *17* (7), 916-922.

33. Contreras, J. A.; Murray, J. A.; Tolley, S. E.; Oliphant, J. L.; Tolley, H. D.; Lammert, S. A.; Lee, E. D.; Later, D. W.; Lee, M. L., Hand-portable gas chromatograph-toroidal ion trap mass spectrometer (GC-TMS) for detection of hazardous compounds. *J Am Soc Mass Spectrom* **2008,** *19* (10), 1425-34.

34. Einfled, W., Environmental technology verification report field-portable gas chromatograph/mass spectrometer. *EPA/600/R-98/142* **1998**.

35. Johnson, M. C., McNamee, M. R., Addink, J. L., US Patent 6,412,173. **2002**.

36. Chen, C. H.; Chen, T. C.; Zhou, X.; Kline-Schoder, R.; Sorensen, P.; Cooks, R. G.; Ouyang, Z., Design of portable mass spectrometers with handheld probes: aspects of the sampling and miniature pumping systems. *Journal of the American Society for Mass Spectrometry* **2014**.

37. Gao, L.; Cooks, R. G.; Ouyang, Z., Breaking the pumping speed barrier in mass spectrometry: Discontinuous atmospheric pressure interface. *Analytical Chemistry* **2008,** *80* (11), 4026-4032.

38. Yang, M.; Kim, T. Y.; Hwang, H. C.; Yi, S. K.; Kim, D. H., Development of a palm portable mass spectrometer. *Journal of the American Society for Mass Spectrometry* **2008,** *19* (10), 1442-1448.

39. Misharin, A.; Novoselov, K.; Laiko, V.; Doroshenko, V. M., Development and characterization of a field-deployable ion-trap mass spectrometer with an atmospheric pressure interface. *Analytical Chemistry* **2012,** *84* (22), 10105-10112.

40. Keil, A.; Talaty, N.; Janfelt, C.; Noll, R. J.; Gao, L.; Ouyang, Z.; Cooks, R. G., Ambient mass spectrometry with a handheld mass spectrometer at high pressure. *Analytical Chemistry* **2007,** *79* (20), 7734-7739.

41. Li, L.; Chen, T. C.; Ren, Y.; Hendricks, P. I.; Cooks, R. G.; Ouyang, Z., Mini 12, miniature mass spectrometer for clinical and other applications--introduction and characterization. *Analytical Chemistry* **2014,** *86* (6), 2909-16.

42. Harris, G. A.; Nyadong, L.; Fernandez, F. M., Recent developments in ambient ionization techniques for analytical mass spectrometry. *Analyst* **2008,** *133* (10), 1297-1301.

43. Weston, D. J., Ambient ionization mass spectrometry: current understanding of mechanistic theory; analytical performance and application areas. *Analyst* **2010,** *135* (4), 661-668.

44. Sosolik, C. E.; Lavery, A. C.; Dahl, E. B.; Cooper, B. H., A technique for accurate measurements of ion beam current density using a Faraday cup. *Review of Scientific Instruments* **2000,** *71* (9), 3326-3330.

45. Gerdin, G.; Stygar, W.; Venneri, F., Faraday cup analysis of ion-beams produced by a dense-plasma focus. *Journal of Applied Physics* **1981,** *52* (5), 3269-3275.

46. Brinckerhoff, W. B.; Cornish, T. J.; McEntire, R. W.; Cheng, A. F.; Benson, R. C., Miniature time-of-flight mass spectrometers for in situ composition studies. *Acta Astronautica* **2003,** *52* (2-6), 397-404.

47. Orient, O. J.; Chutjian, A.; Garkanian, V., Miniature, high-resolution, quadrupole mass-spectrometer array. *Review of Scientific Instruments* **1997,** *68* (3), 1393-1397.

48. Diaz, J. A.; Giese, C. F.; Gentry, W. R., Portable double-focusing mass-spectrometer system for field gas monitoring. *Field Analytical Chemistry and Technology* **2001,** *5* (3), 156-167.

49. Henry, C. M., The incredible shrinking mass spectrometers. *Analytical Chemistry* **1999,** *71* (7), 264a-268a.

50. Brubaker, W. M.; Tuul, J., Performance studies of quadrupole mass filter. *Review of Scientific Instruments* **1964,** *35* (8), 1007.

51. Tian, Y.; Higgs, J.; Li, A.; Barney, B.; Austin, D. E., How far can ion trap miniaturization go? Parameter scaling and space-charge limits for very small cylindrical ion traps. *Journal of Mass Spectrometry* **2014,** *49* (3), 233-40.

52. March, R. E., Quadrupole ion traps. *Mass Spectrometry Reviews* **2009,** *28* (6), 961-989.

53. March, R. E., An introduction to quadrupole ion trap mass spectrometry. *Journal of Mass Spectrometry* **1997,** *32* (4), 351-369.

54. Taylor, S.; Tindall, R. F.; Syms, R. R. A., Silicon based quadrupole mass spectrometry using microelectromechanical systems. *Journal of Vacuum Science & Technology B* **2001,** *19* (2), 557-562.

55. Cornish, T. J.; Ecelberger, S.; Brinckerhoff, W., Miniature time-of-flight mass spectrometer using a flexible circuitboard reflector. *Rapid Communications in Mass Spectrometry* **2000,** *14* (24), 2408-2411.

56. Louris, J. N.; Cooks, R. G.; Syka, J. E. P.; Kelley, P. E.; Stafford, G. C.; Todd, J. F. J., Instrumentation, applications, and energy deposition in quadrupole ion-trap tandem mass-spectrometry. *Analytical Chemistry* **1987,** *59* (13), 1677-1685.

57. Johnson, J. V.; Yost, R. A.; Kelley, P. E.; Bradford, D. C., Tandem-in-space and tandem-in-time mass-spectrometry - triple quadrupoles and quadrupole ion traps. *Analytical Chemistry* **1990,** *62* (20), 2162-2172.

58. Paul, W.; Steinwedel, H., *Ein Neues Massenspektrometer Ohne Magnetfeld. *Zeitschrift Fur Naturforschung Section a-a Journal of Physical Sciences* **1953,** *8* (7), 448-450.

59. Catinella, S.; Traldi, P.; Jiang, X. W.; Londry, F. A.; Morrison, R. J. S.; March, R. E.; Gregoire, S.; Mathurin, J. C.; Tabet, J. C., Negative-ion mass-spectrometry in a commercial gas-chromatography ion-trap mass-spectrometer system. *Rapid Communications in Mass Spectrometry* **1995,** *9* (13), 1302-1309.

60. Mathieu, E., Memoire sur le mouvement vibratoire d'une membrane de former eiiptique. *Journal Mathematics Pure Applied* **1868,** *13*, 137-203.

61. Paul, W., Steinwedel, H., US Patent, 2,939,952. **1960**.

62. Dawson, P. H., and Whetten, N.R., US Patent 5,527,939. **1970**.

63. Stafford, G. C.; Kelley, P. E.; Syka, J. E. P.; Reynolds, W. E.; Todd, J. F. J., Recent improvements in and analytical applications of advanced ion trap technology. *International Journal of Mass Spectrometry and Ion Processes* **1984,** *60* (Sep), 85-98.

64. Stafford, G., Ion trap mass spectrometry: A personal perspective. *Journal of the American Society for Mass Spectrometry* **2002,** *13* (6), 589-596.

65. Goeringer, D. E.; Whitten, W. B.; Ramsey, J. M.; McLuckey, S. A.; Glish, G. L., Theory of high-resolution mass-spectrometry achieved via resonance ejection in the quadrupole ion trap. *Analytical Chemistry* **1992,** *64* (13), 1434-1439.

66. Whitten, W. B.; Reilly, P. T. A.; Ramsey, J. M., High-pressure ion trap mass spectrometry. *Rapid Communications in Mass Spectrometry* **2004,** *18* (15), 1749-1752.

67. Pau, S.; Pai, C. S.; Low, Y. L.; Moxom, J.; Reilly, P. T. A.; Whitten, W. B.; Ramsey, J. M., Microfabricated quadrupole ion trap for mass spectrometer applications. *Physical Review Letters* **2006,** *96* (12).

68. Fico, M.; Yu, M.; Ouyang, Z.; Cooks, R. G.; Chappell, W. J., Miniaturization and geometry optimization of a polymer-based rectilinear ion trap. *Analytical Chemistry* **2007,** *79* (21), 8076-8082.

69. Dehmelt, H. G., Radiofrequency spectroscopy of storedions I: storage. *Advances in Atomic and Molecular Physics* **1967,** *3*, 53-72.

70. Ouyang, Z., Guangxiang Wu, Yishu Song, Hongyan Li, Wolfgang R. Plass, and R. Graham Cooks, Rectilinear ion trap: concepts, calculations, and analytical performance of a new mass analyzer. *Analytical Chemistry* **2004,** *76*, 4595-4605.

71. Pau, S.; Whitten, W. B.; Ramsey, J. M., Planar geometry for trapping and separating ions and charged particles. *Analytical Chemistry* **2007,** *79* (17), 6857-6861.

72. Austin, D. E.; Wang, M.; Tolley, S. E.; Maas, J. D.; Hawkins, A. R.; Rockwood, A. L.; Tolley, H. D.; Lee, E. D.; Lee, M. L., Halo ion trap mass spectrometer. *Analytical Chemistry* **2007,** *79* (7), 2927-2932.

73. Ouyang, Z.; Wu, G. X.; Song, Y. S.; Li, H. Y.; Plass, W. R.; Cooks, R. G., Rectilinear ion trap: Concepts, calculations, and analytical performance of a new mass analyzer. *Analytical Chemistry* **2004,** *76* (16), 4595-4605.

74. Bonner, R. F.; Fulford, J. E.; March, R. E.; Hamilton, G. F., Cylindrical ion trap .1. general introduction. *International Journal of Mass Spectrometry and Ion Processes* **1977,** *24* (3), 255-269.

75. Wells, J. M.; Badman, E. R.; Cooks, R. G., A quadrupole ion trap with cylindrical geometry operated in the mass selective instability mode. *Analytical Chemistry* **1998,** *70* (3), 438-444.

76. Kornienko, O.; Reilly, P. T. A.; Whitten, W. B.; Ramsey, J. M., Electron impact ionization in a microion trap mass spectrometer. *Review of Scientific Instruments* **1999,** *70* (10), 3907-3909.

77. Kornienko, O.; Reilly, P. T. A.; Whitten, W. B.; Ramsey, J. M., Micro ion trap mass spectrometry. *Rapid Communications in Mass Spectrometry* **1999,** *13* (1), 50-53.

78. Ramsey, J. M., and Schultze, K., US Patent 2,014,064,001. **2014**.

79. March, R. E.; Todd, J. F. J., Quadrupole ion trap mass spectrometry, 2nd edition. *Quadrupole Ion Trap Mass Spectrometry, 2nd Edition* **2005,** *165*, 1-351.

80. Wang, Y.; Franzen, J., The nonlinear resonance quistor .1. potential distribution in hyperboloidal quistors. *International Journal of Mass Spectrometry and Ion Processes* **1992,** *112* (2-3), 167-178.

81. Wang, Y.; Franzen, J.; Wanczek, K. P., The nonlinear resonance ion trap .2. A general theoretical-analysis. *International Journal of Mass Spectrometry and Ion Processes* **1993,** *124* (2), 125-144.

82. Moxom, J.; Reilly, P. T. A.; Whitten, W. B.; Ramsey, J. M., Double resonance ejection in a micro ion trap mass spectrometer. *Rapid Communications in Mass Spectrometry* **2002,** *16* (8), 755-760.

83. Wu, G. X.; Cooks, R. G.; Ouyang, Z., Geometry optimization for the cylindrical ion trap: field calculations, simulations and experiments. *International Journal of Mass Spectrometry* **2005,** *241* (2-3), 119-132.

84. Chaudhary, A.; van Amerom, F. H. W.; Short, R. T., Experimental evaluation of micro-ion trap mass spectrometer geometries. *International Journal of Mass Spectrometry* **2014,** *371*, 17-27.

85. Moxom, J.; Reilly, P. T. A.; Whitten, W. B.; Ramsey, J. M., Analysis of volatile organic compounds in air with a micro ion trap mass analyzer. *Analytical Chemistry* **2003,** *75* (15), 3739-3743.

86. Moxom, J.; Reilly, P. T. A.; Whitten, W. B.; Ramsey, J. M., Sample pressure effects in a micro ion trap mass spectrometer. *Rapid Communications in Mass Spectrometry* **2004,** *18* (6), 721-723.

87. Blain, M. G.; Riter, L. S.; Cruz, D.; Austin, D. E.; Wu, G. X.; Plass, W. R.; Cooks, R. G., Towards the hand-held mass spectrometer: design considerations, simulation, and fabrication of micrometer-scaled cylindrical ion traps. *International Journal of Mass Spectrometry* **2004,** *236* (1-3), 91-104.

88. Austin, D. E.; Cruz, D.; Blain, M. G., Simulations of ion trapping in a micrometer-sized cylindrical ion trap. *Journal of the American Society for Mass Spectrometry* **2006,** *17* (3), 430-441.

89. Xu, W.; Song, Q. Y.; Smith, S. A.; Chappell, W. J.; Ouyang, Z., Ion trap mass analysis at high pressure: A theoretical view. *Journal of the American Society for Mass Spectrometry* **2009,** *20* (11), 2144-2153.

90. Song, Q. Y.; Xu, W.; Smith, S. A.; Gao, L.; Chappell, W. J.; Cooks, R. G.; Zheng, O. Y., Ion trap mass analysis at high pressure: an experimental characterization. *Journal of Mass Spectrometry* **2010,** *45* (1), 26-34.

91. Hendricks, P.; Duncan, J.; Noll, R. J.; Ouyang, Z.; Cooks, R. G., Performance of a low voltage ion trap. *International Journal of Mass Spectrometry* **2011,** *305* (1), 69-73.

92. Major, F. G.; Dehmelt, H. G., Exchange-collision technique for Rf spectroscopy of stored ions. *Physical Review* **1968,** *170* (1), 91-107.

CHAPTER 2: DEVELOPING HPMS WITH HELIUM BUFFER GAS

2.1 Introduction

To study the effects of high pressure on mass resolution, helium buffer gas was chosen for initial proof of concept experiments. This choice was made since ions are scattered less by collisions with a smaller neutral buffer gas thereby reducing collisional effects. The resulting mass spectra should have better mass resolution and sensitivity compared to the larger nitrogen or air buffer gases.[1] The ion trap chosen was a r_o = 500 µm and z_o = 645 µm CIT previously used in low pressure experiments with helium buffer gas.[2] While helium is not an ideal buffer gas for a handheld instrument because of the need for an external tank, the information gathered here is still directly applicable to cases where mass resolution concerns outweigh SWaP concerns. Note that the ion traps could still operate at elevated pressures and reduce pumping requirements relative to current luggable mass spectrometers.

To investigate ion traps for operation at elevated pressures at and above 1 Torr, ionization and detection concerns must be addressed. Figure 2.1a shows a schematic for a custom differentially pumped mass spectrometer designed specifically for ion trap development along with an exploded view of the system (Figure 2.1b).[2] The ionization source (1) and ion trap (2) are housed in a mass analysis chamber separated from a detector chamber. The two chambers can be operated at equalized pressures or with pressure differentials up to three orders of magnitude via a bypass valve. Electron multipliers (3) are

well-established as detectors for QIT instruments due to their high sensitivity and sampling bandwidth, but they do not tolerate buffer gas pressures above ~ 10 mTorr.[3] With differential pumping we take advantage of their high sensitivity and bandwidth while focusing on ionization source and trap development. For a potential handheld device with a single vacuum chamber, pressure insensitive Faraday cups are the best option for detection[4] however further development is needed to improve the electrical circuitry that currently limits the gain and bandwidths of Faraday cup detectors.

While high pressure detection presents a significant challenge for developing ion trap technology, ionization sources covering wide ranges of pressures are available. For low pressures, thermionic emitters are well-developed and commercialized. In the 1 Torr regime, glow discharge electron sources have been developed, while ambient ionization sources have also been demonstrated for miniature ion traps.[5-6] Housing the ionization source in the same chamber as the mass analyzer simplifies the design, two versus three chambers, and minimizes the separation between the ionization source and mass analyzer. The short separation between ionization source and ion trap reduces the difficulties with ion transport at high pressures. This small separation is also advantageous for handheld instrument in terms of minimizing size and weight. Even though ionization sources have been widely optimized for high pressures up to ambient pressure, power and size optimization must also be considered for use in a handheld instrument.

2.2 Experimental

For the HPMS system, two separate pumping systems (TPS Bench and TPS Compact, Agilent) were used to differentially pump the chambers to desired pressures. A conduction-limiting valve between the high-pressure chamber and turbopump was used to limit pump

conductance. At 1 Torr in the mass analysis chamber, the detector chamber pressure ranged from 10 and 30 mTorr depending on experimental setup and gas flow.

Headspace samples of mesitylene, 2-chloro ethyl ethyl sulfide (CEES) and octane (all from Sigma Aldrich, Milwaukee, WI), as well as xenon gas (99.999%, Nova Gas Technologies) were introduced to the ionization and mass analysis chamber with an uncorrected pressure of approximately $1x10^{-5}$ Torr with a precision leak valve (ULV-150, MDC Vacuum Products) and measured with a FRG-700 Agilent vacuum gauge. Helium buffer gas was introduced to the high pressure chamber with a FMA5402 Omega mass flow controller and measured with a NIST traceable MKS 627D capacitance manometer which is accurate to ± 0.12% of the pressure reading. To increase the operating pressure, the helium flow rate was increased while maintaining the same analyte partial pressure.

Custom LabVIEW software was used to synthesize control waveforms using an 8-channel analog out card (PXI-6733, National Instruments). The CIT was constructed from three electrodes that were chemically etched from sheet metal. The ring electrode was copper and had a thickness of 790 µm and trap radius of 500 µm. The two endcap electrodes were 250 µm thick and had 400 µm apertures. To form the ion trap from the electrodes as shown in Figure 1.3, the three electrodes were stacked and separated by #2 Teflon washers that were 250 µm thick. The Teflon washers both electrically isolate the ring from the endcap electrodes and determine the z_o dimension.[7] The critical dimensions for the CIT were r_o = 500 µm and z_o = 645 µm.

To achieve the RF voltages required to perform mass analysis with a r_o = 500 µm CIT, a custom RF system was optimized for RF drive frequencies above 1 MHz. Figure 2.2 shows the block diagram of the RF trapping voltage generation. A commercially available

RF signal generator (HP 8648A, Hewlett Packard) produced an amplitude modulated 6 to 10 MHz RF drive waveform with amplitudes ranging from -1 to 1 V (p-p). That voltage was amplified by approximately a factor of 30 with a custom RF preamplifier. The signal was then amplified up to 1000 V (p-p) through a RF power amplifier and air core inductor, which was used to create a resonant circuit. An oscilloscope (TDS3034C, Tektronix) monitored and measured the RF signal during MS experiments. Scan rates were approximately 15,000 Da/s. For double resonance ejection, a Tektronix AFG3022b signal generator was used to directly apply a 1 to 10 V (p-p) to the endcap electrode nearest the ionization source. The second endcap electrode was permanently grounded against the chamber wall.

Tungsten filaments were used to generate ions for internal electron impact ionization. A pair of benchtop DC power supplies provided the heating current and bias from -70 V to -125 V to drive the filament. Power draw was approximately 4.8 W (2.2 V, 2.2 A) for the tungsten filament. During mass analysis a gate lens between the ionization source and trap was pulsed from 0 V to -150 V to prevent further electron introduction into the CIT. The microionizer, a new silicon-based ionization source for HPMS was also developed (using deep reactive ion etching) and tested.

For detection, a Detech 2300 electron multiplier was pulsed from 0 V to -1600 V during mass analysis. The signal output was amplified at 200 nA/V by a current preamplifier (SR570, Stanford Research Systems) then digitized with a 16 bit analog input card (PXI-6122, National Instruments) at 500 kHz. Each mass spectrum was recorded as an average of 1000 mass spectra and 4 scans were averaged to produce error bars, plotted as standard error. The data was digitally low pass filtered at 30 kHz with in-house data processing software to remove high frequency noise components.

2.3 Ionization Source

The ionization source requires optimization at higher pressures. Tradeoffs between generating ions externally and internally relative to the ion trap should be considered. The short mean free path from high pressure operation scales favorably for trapping of externally generated ions. Ions generated externally to the ion trap are cooled by collisions with neutral buffer gas molecules to kinetic energies below the pseudopotential well depth and trapped.[8-9] However, the ion-neutral collisions can result in ions being scattered and never reaching the ion trap, which limits sensitivity. Ion optics such as einzel lenses and ion guides to focus ions into the trap can be used to increase signals[10-11] but they add complexity to a potential instrument through size, weight, and power concerns.

Electron ionization (EI) sources are used to inject electrons directly into the ion trap where ions are formed and trapped internally. Since the ions are formed internally, they have low kinetic energy and do not require high ion trap D_z values to mass analyze ions. At high pressures, the decreased mean free path and separation needed between an ionization filament and CIT due to temperature considerations reduces the electron energy and flux reaching the trap and thus reducing signal strength.[12] Electrons with -70 eV kinetic energy have traditionally been used to match the DeBroglie wavelength of the carbon-carbon bond to promote fragmentation.[13-15] A simple solution for low signal level is to increase the power to the filament improving emission current, resulting in more electrons and thereby improving signal strength. Such trends have been previously reported with microscale CITs and xenon analyte at buffer gas pressures below 1 mTorr.[16] With higher pressures, increasing the power to the filament to account for emission loss will compromise its lifetime, of concern for portable instrument use in the field.

2.3.1 Ionization Source Optimization

Initial attempts at HPMS were severely limited by low signal strength with reduced flux of electrons reaching the trap. Several strategies were attempted unsuccessfully to improve sensitivity. The filament power was increased beyond the rated limits and long signal averages were acquired to try and improve signal to noise at the expense of analysis time. The ionization time was also increased to introduce more electrons into the trap. Despite these efforts, successful mass analysis was not realized, presumably from the failure to ionize enough of the analyte in the trap. Since the mean free path of both ions and electrons decrease linearly with increasing pressure, electron-accelerating energy was studied as a new variable for signal enhancement.

The electron energy used for ionization was initially not an obvious variable for high pressure operation since mass spectral libraries have used -70 eV electrons for creating reference spectra. The elevated pressures exceeding three orders of magnitude above commercial instruments will significantly lower the mean free path for electrons and decrease their kinetic energy at the trap. This can have significant affects on sensitivity. For these reasons, changes in the electron energy were pursued as an experimental variable for HPMS.

The effect of electron energy was tested at -70 eV, -100 eV and -125 eV for both xenon and mesitylene at helium buffer gas pressures of 1.0 and 1.2 Torr and RF drive frequencies of 6.3 and 6.73 MHz. The resulting spectra are shown in Figures 2.3 and 2.4. As a noble gas, xenon fragmentation is impossible so xenon isotope ions will be observed irrespective of the pressure. Any changes in signal as a function of electron energy can be

attributed to more efficient xenon ionization. Mesitylene is a small volatile organic compound (VOC) with a molecular mass of 120 grams per mole. Changes in electron energy are known to cause different fragmentation patterns for small VOCs and could be of interest for their identification. Signal intensities improved for both xenon and mesitylene as the electron energy increased. For xenon, the signal improved by a factor of 15 for a 78% increase in electron energy. While the xenon isotopes were indistinguishable due to poor signal strength at -70 eV, five isotopes (129 Da, 131 Da, 132 Da, 134 Da, and 136 Da) are seen at -125 eV. Since xenon has an ionization energy of approximately 12 eV, this suggests that electrons lost significant kinetic energy to collisions with neutral molecules between the source and the ion trap.[17]

For the simple VOC mesitylene, signal improved by a factor of 5 over the same 55 V increase in electron energy. This was a factor of 3 lower signal improvement compared to xenon. Two possibilities for these signal level differences include the 200 mTorr operating pressure difference, and differences in collisional properties between an atom (xenon) and a molecule (mesitylene). Fragmentation patterns and relative peak intensities between 105 Da and 120 Da mesitylene peaks were indistinguishable between electron energies. Using accelerating voltages above -125 eV could potentially improve signal strength but at the risk of electrical breakdown. Additionally, operating at higher bias voltages would shorten filament lifetime. This could cause increased operational downtimes and costs as instrument maintenance needs are met.

2.3.2 Effect of Pressure on Mass Resolution

The detection of VOCs is a prime target area for a potential handheld instrument as are chemical warfare agents (CWA). Two model analytes (CEES and octane) were therefore used to demonstrate the ability to measure these classes of compounds. CEES is a chemical warfare agent simulant for mustard gas[18] and octane is a constituent in gasoline. The spectra were normalized for presentation to account for filament cooling and lower current density at the CIT with increasing pressure. Axial RF conditions were re-optimized with pressure to maintain resonance ejection and to minimize peak broadening effects.[19] Using the -125 eV bias on the ionization source, CEES was detected at pressures of 62 mTorr, 540 mTorr and 1.21 Torr with a drive RF of 6.73 MHz as seen in Figure 2.5. Despite a factor of 20 increase in pressure, the main peaks seen at 124 Da (molecular ion), 89 Da (loss of chlorine), and 75 Da (loss of methyl chloride), are present in all spectra. As pressure increased, the 89 Da peak increased in signal intensity with a second shoulder peak appearing. The peak at 124 Da remained strong over the entire pressure regime. Each peak also broadened with increasing pressure due to more frequent ion-neutral collisions, with the 126 Da peak becoming a shoulder of the 124 Da peak at 1.2 Torr.

Because the number of ion-neutral collisions scales proportionally with pressure, mass resolution is a key concern. Full-width at half maximum (FWHM) peak widths for 75 Da were experimentally determined as a function of buffer gas pressure (Figure 2.6). The 75 Da peak was chosen for analysis since there were no strong-overlapping peaks that would interfere with peak fitting. Overall, peak widths increased 40% from 0.75 Da at 62 mTorr to 1.26 Da at 1.2 Torr. From 280 mTorr to 1.2 Torr the trend was quite linear with pressure, but leveled off below 200 mTorr. At lower buffer gas pressures, pressure effects no longer limits

mass resolution. Instead, other characteristics of the CIT including higher order field components and imperfections in the electrode fabrication limit resolution.[20-22] The more frequent ion-neutral collisions at pressures above 200 mTorr determined peak widths in the pressure range studied up to 1.2 Torr

In addition to experimentally investigating the trend between peak width and pressure, the anticipated increase in peak width was modeled. Building off the work by Goeringer *et al.* (Equation 1.6) describing how increasing the RF drive frequency should improve mass resolution, Arnold *et al.* showed that mass resolution for an ion trap also varies as a function of scan rate (a_m), secular frequency ($\omega_o = 0.5\ \Omega$), thermal energy (kT), and neutral mass (M) (Equation 2.1):[23]

$$\frac{\Delta m}{m} = \frac{\sqrt{\frac{\pi a_m \Omega z_0}{m} + 8/\tau^2}\sqrt{\frac{kT}{m r_0^2 \omega_0^2} + \frac{1}{3}\frac{M}{m}}}{\Omega/2} \tag{2.1}$$

with τ calculated as 2/c, where c is the collisional frequency defined by Equation 2.2:

$$c = P\frac{M}{m+M}\Gamma \tag{2.2}$$

where Γ is a constant factor held at 1 for these calculations.[24] Langevin collision theory was used to determine the probability of a collision (P) [25-26] and the CIT temperature was approximated as ambient temperature of 20 °C. Equation 2.1 incorporates the effect of ion-neutral collisions on peak broadening but does not account for the effect of higher order fields or electrode imperfections, which can dominate at lower pressures since they are pressure independent. As such, an offset taking these factors into consideration is necessary

to fit the data. Equation 2.3 describes a model linear fit that accounts for both contributions to peak width:

$$\Delta m = \propto P + \beta \qquad (2.3)$$

where $\propto$ is the slope of peak width vs. pressure generated by Equation 2.1 and β is the peak width contribution from higher order fields and electrode imperfections. The value of β was determined by fitting a line to the linear region of the experimental data (pressures > 300 mTorr) with a slope of $\propto$. By extending this line to zero, the y-intercept was the contribution attributed to peak broadening caused by higher order fields and electrode imperfections. The β value was 0.56 Da for CEES.

At higher pressures where ion-neutral collisions effects dominate peak width, good agreement was observed between the experimental data and theoretical model (Figure 2.6). This concordance was anticipated since Equation 2.1 was developed specifically to address high pressure effects on trap operation. The theoretical data agreed best with the experimental data at 1.0 Torr and 1.2 Torr with the experimental and theoretical peak widths varying by just 3% and 0.7%. At pressures above 300 mTorr where mass resolution is collision limited, a linear increase of 0.52 Da-Torr^{-1} for the peak widths is observed. The calculated peak width trend over this pressure range increased by 0.62 Da-Torr^{-1}, or 17% different from the experimental data. As a point of reference, Xu *et al*. predicted a 32 Da-Torr^{-1} increase in peak width for their RIT.[19] Note that their model used lower RF drive frequencies and ambient air as the buffer gas, meaning a higher slope would result. The higher RF drive frequency used here (6.72 MHz) as predicted helps prevent peak broadening as pressures increase.

In addition to CEES, octane was also analyzed over the pressure range of 110 mTorr to 1.0 Torr at 9.43 MHz drive RF (Figure 2.7) with several peaks observed over the 41 Da to 85 Da range, corresponding to the fragment peak $C_6H_{13}^+$ and subsequent methyl group losses. The individual peaks are well-defined at 110 mTorr, while the peaks are still present at 1.0 Torr with sufficient resolution that they could easily be handled by peak matching software for identification. Peak fitting utilized the 41 Da peak as minimal peak overlap with the 42 Da signal was seen and there was no detectable signal at 40 Da.

Peak widths increased from 0.46 Da at 110 mTorr to 0.82 Da at 1.0 Torr, a 77% increase (Figure 2.8). Linear modeling of the peak width vs. pressure from 0.30 Torr to 1.0 Torr showed a peak width increase rate of 0.51 Da-Torr^{-1}. This compares well with the Arnold model (offset = 0.39 Da) where peak widths were predicted to increase by 0.56 Da-Torr^{-1} or ~10% higher (fitted line in Figure 2.8). As with CEES, the significant peak width variation between theory and experiment was seen at lower buffer gas pressures where trap properties dominate. For pressure regions where collisional broadening limited mass resolution, good agreement was seen between calculation and experiment for both CEES and octane.

2.4 The Microionizer

Thermionic emitters including tungsten filaments were chosen for initial HPMS demonstration since they are commercially available and have successfully been coupled with miniature ion traps. Since they are only reliable at low pressures below 1 mTorr of inert gasses and require high power (4 to 6 W), their inclusion in a handheld instrument is disadvantageous.[27-28] Glow discharge whether used to generate ions or electrons is a low

power (0.1 W), oxygen-tolerant alternative electron source to thermionic emitters.[5] The typical dimensions (3 cm diameter plates separated by a 1 cm insulator) required to produce the glow discharge near 1 Torr are a fundamental limitation for miniaturization. While glow discharge sources are feasible with handheld mass spectrometry, a more scalable source would still be ideal for further size and pumping volume optimization. Ambient ionization sources including electrospray ionization and atmospheric pressure chemical ionization have been demonstrated for in situ applications but have size and power concerns for inclusion in a portable instrument.[6, 29] With ion traps that have been scaled to the microscale dimensions, having an ionization source with micron dimensions would be ideal.

Alternatives to thermionic emitters are field emission and field ionization devices. These devices have the potential to decrease physical size and power requirements by several orders of magnitude. In field emission, electrons tunnel from the surface of a conductor or semi-conductor into vacuum under the presence of a strong electric field.[30] Field ionization occurs when a molecule is ionized in the presence of an electric field exceeding 10^7 V/cm produced at a conducting surface. The electron released from the ionized molecule subsequently tunnels through vacuum to the conducting material.[30-31]

Several miniaturized ionization sources that have significant size advantages over filament and glow discharge ionization sources have been proposed using both mechanisms. A soft ionization membrane (SIM) has been developed by the Jet Propulsion Laboratory using field ionization.[32] The structure consists of two 0.03 μm gold layers separated by a 0.3 μm silicon nitride layer. There are apertures for gas flow through the high field region. A potential of 10 V applied across the gold layers produces an electric field above 10^7 V/cm,

enough to field ionize nearly 100 % of ions that pass through the holes in the membrane forming a molecular ion.

Field emission devices have been fabricated with a variety of materials including carbon nanotubes,[33] diamond,[34-35] silicon,[36] and diamond coated silicon whiskers.[37] Sharp tip devices produce large electric fields at low operating voltages, minimizing voltage and power requirements compared to devices without field enhancements. Field emission and ionization devices have similar shortcomings. Since many of these devices rely upon sharp tips, poor pressure tolerance, electrical breakdown, tip erosion, and limited lifetimes have been encountered.[38] Reducing the operational duty cycle by running the devices in pulsed mode improves lifetime considerations. It also eliminates the need for a gate lens electrode required for thermionic emitters. Manufacturing costs creating the sharp tips can be high, and some devices still require high voltages.[39-40] There still remains a need to develop new devices that realize power and size savings while maintaining cheap production cost and long lifetimes.

2.4.1 Microionizer Concept and Operation

A silicon-based microionizer was developed in collaboration with Stanley Pau at the University of Arizona. Figure 2.9a-c shows the layout of one device. The device itself is 1 cm^2 (Figure 2.9a) with a thickness of approximately 400 μm, small enough to easily fit into a miniaturized vacuum system. Within the device there are 16 regions of etched features (Figure 2.9b), with the four by four array layout design improving structural stability of the devices. Figure 2.10c shows an SEM image of a 20 μm cylindrical feature. The sidewalls are visibly scalloped from the Bosch deep reactive ion etch (DRIE) fabrication process.[41-42]

Sharp points formed by the Bosch process on the sidewalls serve as field emission points. The device is made with a silicon-on-insulator (SOI) wafer consisting of two N-doped silicon semiconductive layers separated by a 500 nm SiO_2 insulating layer. DRIE is used to etch features into the device, which included 5 µm, 10 µm, 20 µm, and 100 µm diameter cylinders. Trench features that were 2 µm by 90 µm were also fabricated. The devices were through etched to introduce gas flow through the devices, and potentially improve sensitivity. Figure 2.10 shows a schematic of the physical layout and operational process. When a small voltage pulse (≈ 35 V) is applied across the two silicon layers, a 7 x 10^5 V/ cm electric field is generated excluding any field enhancement effects at the emission tips. This field strength is sufficient to cause electron emission. After emission, the electrons are accelerated towards the ion trap by biasing the microionizer layer closest to the trap with the desired kinetic energy.

A PCB-based mounting platform was developed to make a pressure based electrical contact to the microionizer. The pressure contacts proved sufficient for proof of concept experiments with limited quantities of devices. As a cold electron emission source, the microionizer was pulsed on during ionization to minimize power draw and improve device lifetime. A PVA3354 photovoltaic relay switch was used to control the ionization pulse while the input and output ionizer signals were monitored and measured by a Tektronix TDS2022B oscilloscope.

2.4.2 Microionizer Generated High Pressure Mass Spectra

The first demonstration of the microionizer as an electron source (-75 eV electrons) is shown in Figure 2.11 where xenon was mass analyzed at a helium buffer gas pressure of 1.3

Torr. Major xenon isotope peaks at 129, 131, 132, 134, and 136 Da were observed despite the elevated pressure with peak widths of approximately 1.4 Da. The ion trap was a 19-element CIT array (r_o = 500 μm) chosen to improve sensitivity and was operated at a 6.72 MHz RF drive frequency. Filaments have concentrated emission from the tip of the device that covers a small surface area approximately 12 mm^2, or 7 elements of a 19-element array. The microionizer is a planar electron emitting array designed to emit over the 36 mm^2 region that encompasses the ion trap array. The separation of the ionization source to the trap was decreased from approximately 20 mm with the filament to 5 mm with the microionizer in an attempt to improve sensitivity.

Despite the efforts to optimize microionizer signal, the signal strength generated by the microionizer was still lower than spectra acquired with a filament. Filaments were routinely used to characterize the operating parameters of CITs before coupling to a microionizer. When the microionizer was coupled to a previously characterized CIT there was small signal above the noise baseline. This is not surprising since filaments are a well-developed technology while the microionizer is in its initial development stages. Sensitivity could be further addressed through continued development of the microionizer and geometry changes such as lowering the separation of the microionizer and ion trap.

While the microionizer is capable of operating at high pressures with helium buffer gas, power draw is also important. For the xenon spectra, the microionizer was run with a 1.5 ms ionization time and had an average power draw of 0.14 W (35 V, 4 mA). The duty cycle of the microionizer was 3% and drew 188% less power than the tungsten filament. The current draw for the microionizer was higher than anticipated and limited the field strengths that were achieved. The electric field strength could be higher with improved leakage

current, which has the potential to bridge the signal gap between the filament and microionizer performance.

The microionizer was further tested with dimethyl methylphosphonate (DMMP), a CWA simulant for the nerve gas VX, as the analyte (Figure 2.12).[43] The same CIT array was used although the helium buffer gas pressure was raised to 1.7 Torr, the maximum pressure possible for this instrumental setup. The molecular ion (124 Da) was the major peak, while the two most abundant fragments (109 Da and 94 Da) resulted from subsequent methyl group losses. Signal intensity was higher for DMMP than xenon, suggesting more efficient ionization under HPMS conditions. The power draw was higher for DMMP than xenon by 35% at 0.20 W (34 V, 6 mA) although still 182% lower than a tungsten filament.

Several operational limitations with the microionizer were encountered. Electrical breakdown was observed between the ion trap and the microionizer destroying several devices. The main cause of breakdown is the presence of high RF voltages applied near the microionizer and an abundance of charges produced by the microionizer. Improved electrical contacts and shielding of the ion trap from the microionizer could address these limitations. These initial microionizers also had lifetimes on the order of a few hours. Although lifetime was often compromised to determine the limits of operating parameters, lifetimes of weeks to months are desirable, particularly if they could be easily replaced in portable instruments. Since lifetimes currently limit widespread use of field emitters in mass spectrometry, this device characteristic was not surprising. An additional limitation noted was leakage current, which resulted from poor SiO_2 insulating properties that increased the power draw significantly.[44] While a 500 nm insulating layer was expected to have minimal leakage current, this turned out not to be the case. However, even with leakage currents

inflating power draw, the power draws were comparable to well-optimized glow discharge power requirements (0.1 W).

While the microionizer has limitations and therefore requires further development, it was the first miniaturized ionization source coupled to HPMS. The potential to reduce the size and power consumption of a final instrument with the use of a microionizer is important. Thermionic emitters operate at temperatures exceeding 1,200 ^{o}C and require physical separation from the ion trap.[45] Furthermore, they cannot be effectively cycled on the millisecond time scale and require a gate lens, which adds size and power consumption. From Paschen's curve, a glow discharge source at 1 Torr should have plate separations near 1 cm for minimal voltage activation.[46] The microionizer with a thickness of 400 μm is 184 % less than the separation between two glow discharge electrodes. This represents a significant decrease in the volume size of the instrument.

Operation of the microionizer as a cold cathode field emission device at high pressures is uncommon for field emission devices. Field emission devices are damaged by ion bombardment at elevated pressures unless the device dimensions are shorter than the mean free path, and operating voltages are below the ionization energies of molecules present.[47] Since the microionizer has simplified emission tips compared to those found in many field emission devices, it has the potential to survive ion bombardment better than current devices and improve lifetime despite pressures six orders of magnitude above normal operating pressures for field emission.[35, 40]

2.5 Conclusions

A differentially pumped mass spectrometer with a 500 μm CIT was used to demonstrate mass analysis at elevated helium buffer gas pressures up to 1.2 Torr. Experimental considerations for ionization, mass analysis, and detection as a function of buffer gas pressure are reported. Factors of 15 and 5 integrated signal improvements were seen by increasing the electron energy from -70 eV to -125 eV for xenon and mesitylene in 1.2 Torr and 1.0 Torr of helium. Peak widths were characterized as a function of buffer gas pressure and found to increase 40% for CEES and 77% for octane over the studied ranges. With peak widths near unit resolution at 1 Torr of buffer gas, the feasibility of operating CITs at high pressures with elevated RF frequencies in a portable instrument was demonstrated.

A field emission based microionizer designed and developed for high pressure operation was demonstrated with a 500 μm 19-element CIT array for xenon and DMMP at pressures of 1.3 Torr and 1.7 Torr. Power draws were improved by 180 % compared to tungsten filaments. The fundamental size and volume advantages for the microionizer over different ionization sources were also discussed. By demonstrating mass spectrometry at buffer gas pressures over 1 Torr of helium, the theoretical scaling of QITs with size and pressure was confirmed.

2.6 Figures:

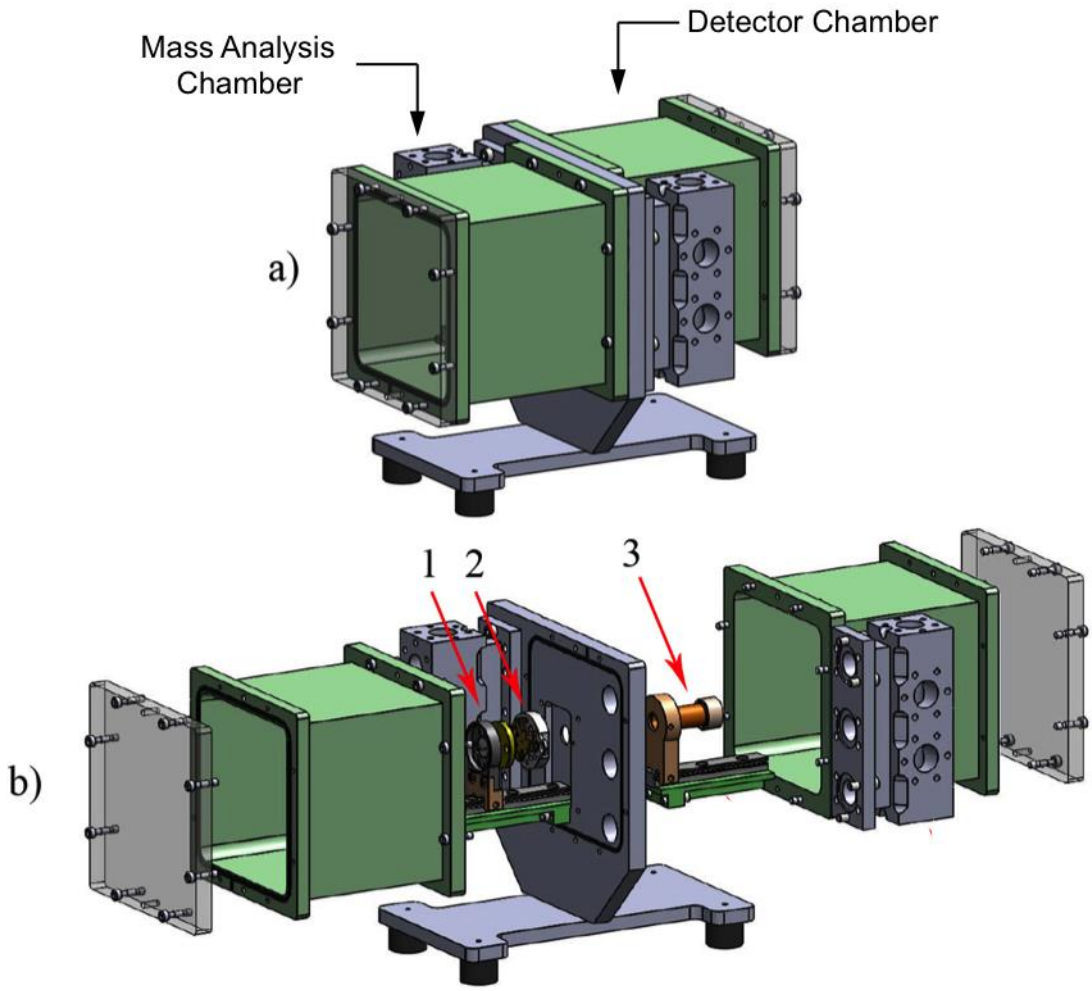

Figure 2.1 (a) Schematic for a differentially pumped mass spectrometer showing the mass analysis chamber and detection chamber plus exploded view of system (b) The ionization source (1) and the mass analyzer (2) are operated at elevated pressures while the detector (3) is maintained at low pressures (≤ 30 mTorr). Each chamber is pumped by a separate pumping system for maximum pressure control.

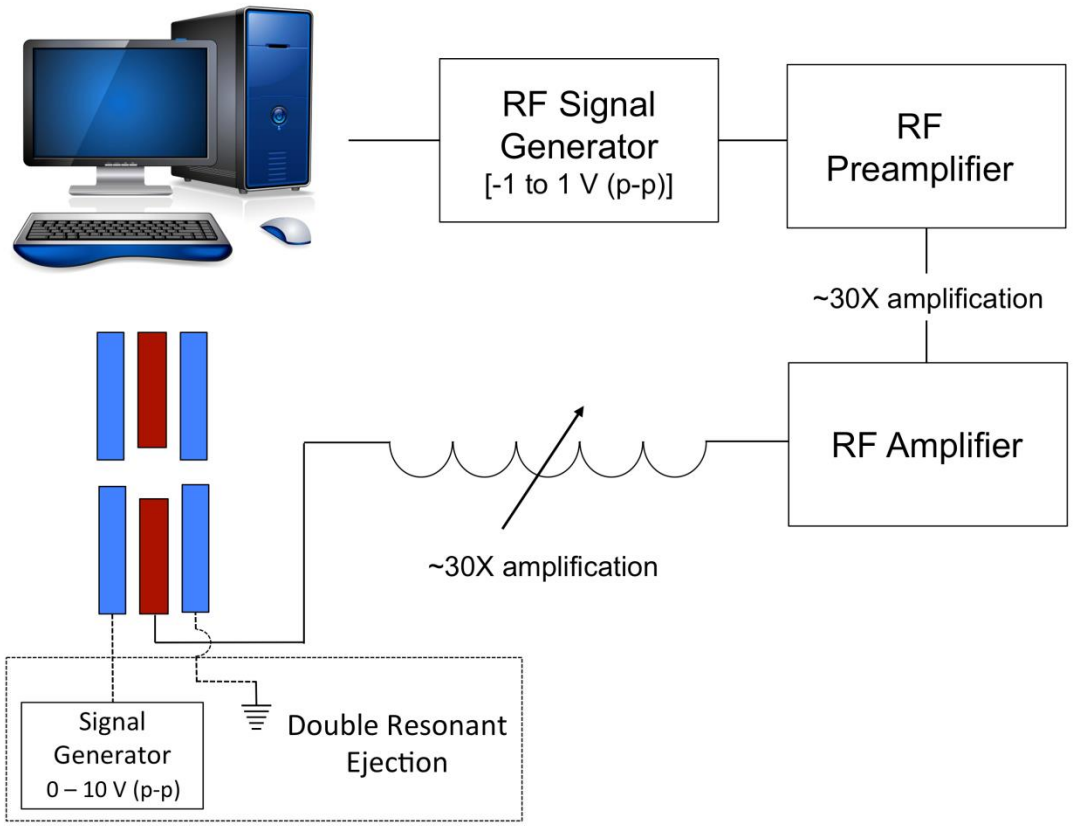

Figure 2.2: Schematic for the instrumentation used to generate RF drive frequency voltages to perform mass analysis with microscale ion traps. For double resonant ejection experiments the connections in the dashed boxed area are also used.

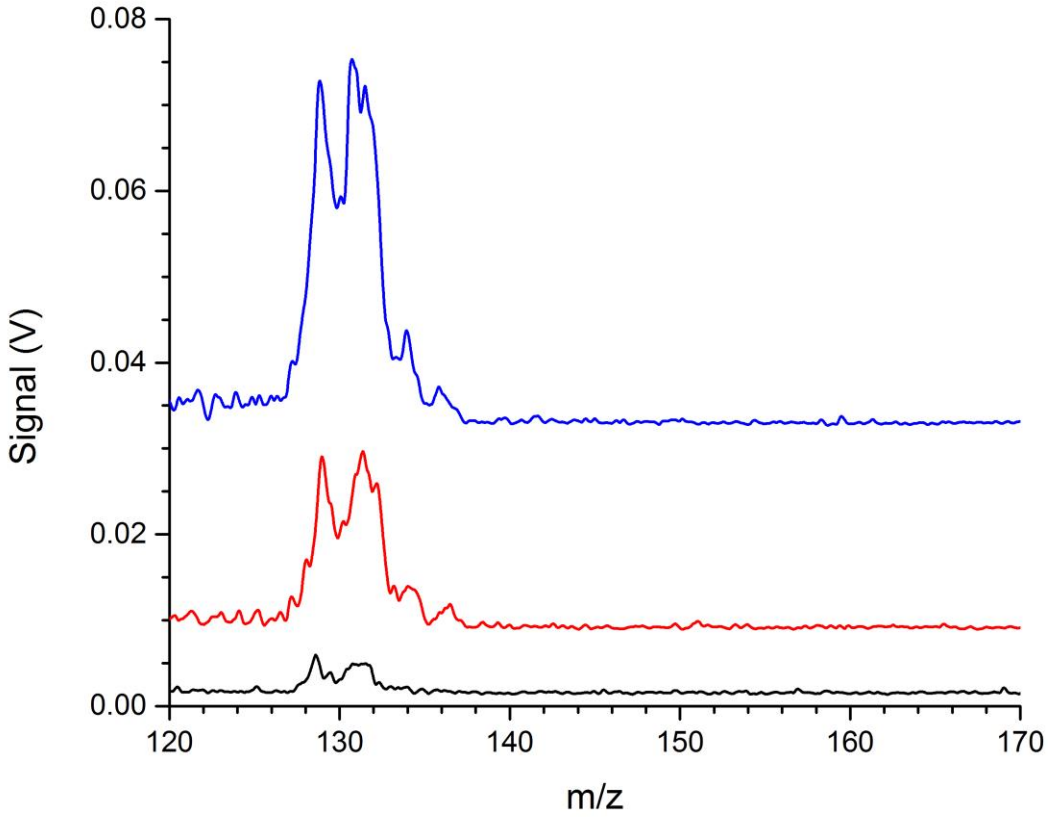

Figure 2.3: Mass spectra of xenon in 1.2 Torr of helium with increasing electron energy for internal election impact ionization -70 eV (——), -100 eV (——), and -125 eV (——). Integrated signal increased by a factor of 15 over the -55 eV span.

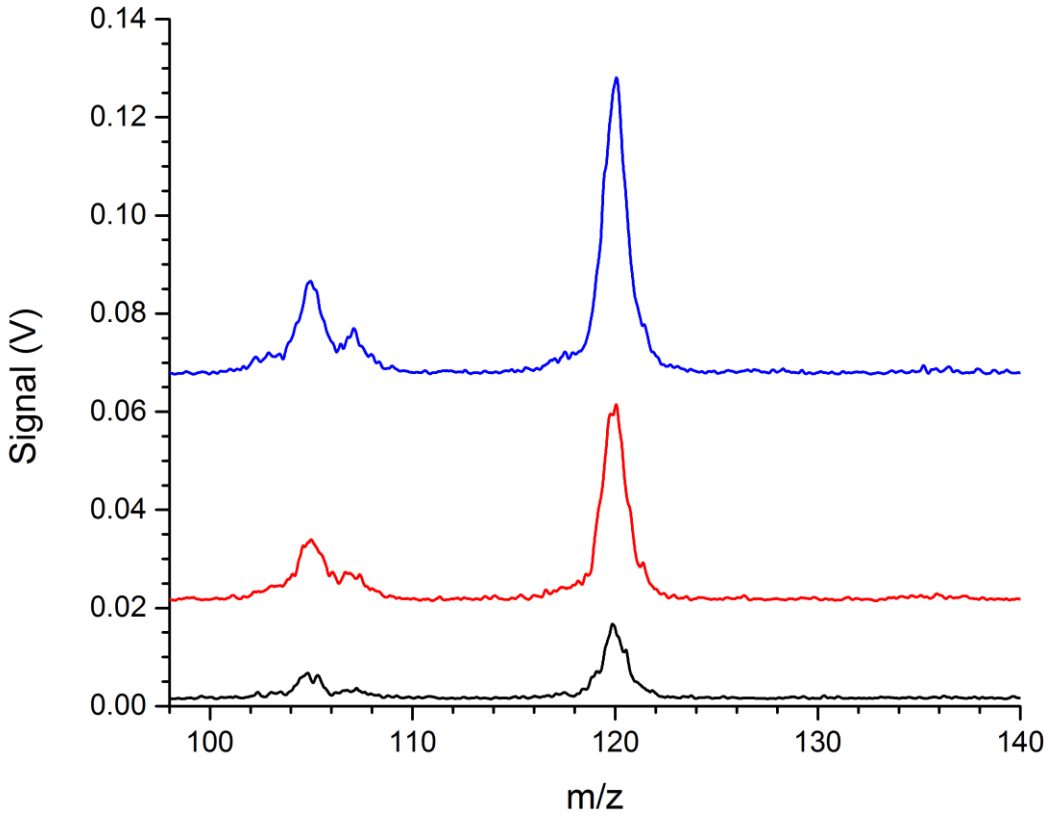

Figure 2.4: Mass spectra of mesitylene in 1.0 Torr of helium with increasing electron energy for internal election impact ionization -70 eV (——), -100 eV (——), and -125 eV (——). Fragment peak ratios remain similar despite the change in electron energy, although overall signal intensity increases with electron energy.

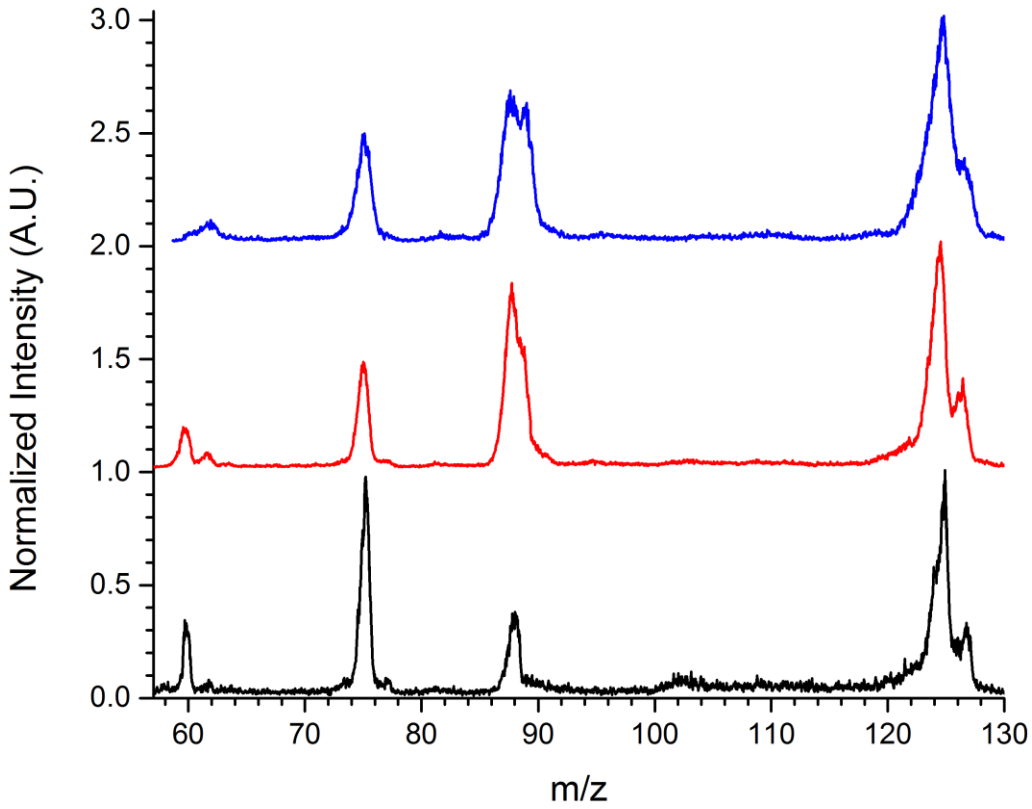

Figure 2.5: Mass spectra of 2-chloro ethyl ethyl sulfide (CEES) at 6.73 MHz drive RF with increasing buffer gas pressures of 62 mTorr (——), 540 mTorr (——), and 1.2 Torr (——).

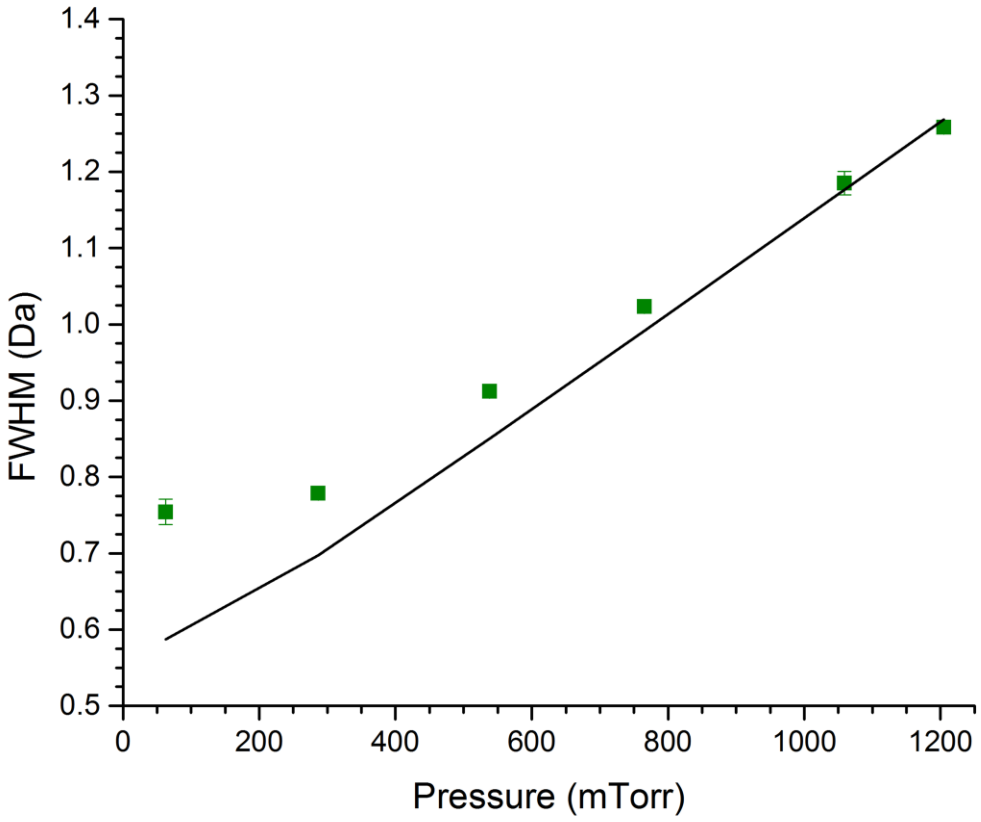

Figure 2.6: Peak widths (FWHM) for the CEES peak at 75 Da as a function of buffer gas pressure (■) and fit with Equation 2.1 (——).

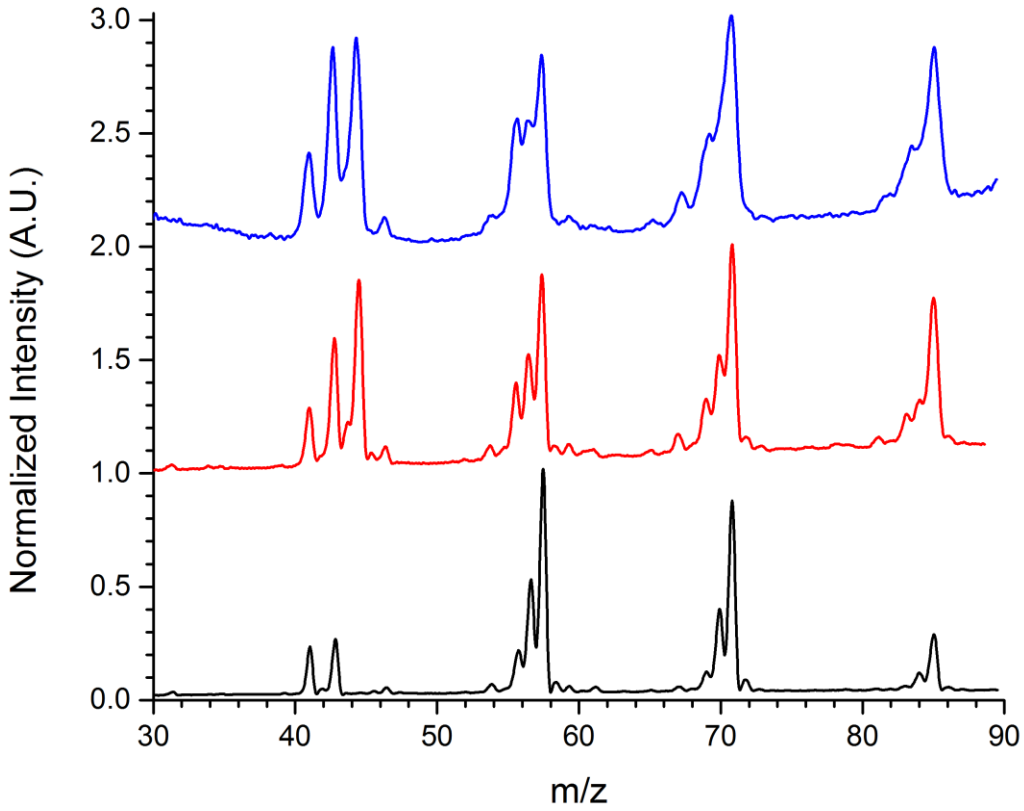

Figure 2.7: Mass spectra of octane at 9.43 MHz drive RF with increasing buffer gas pressure at 110 mTorr (——), 570 mTorr (——), and 1.0 Torr (——).

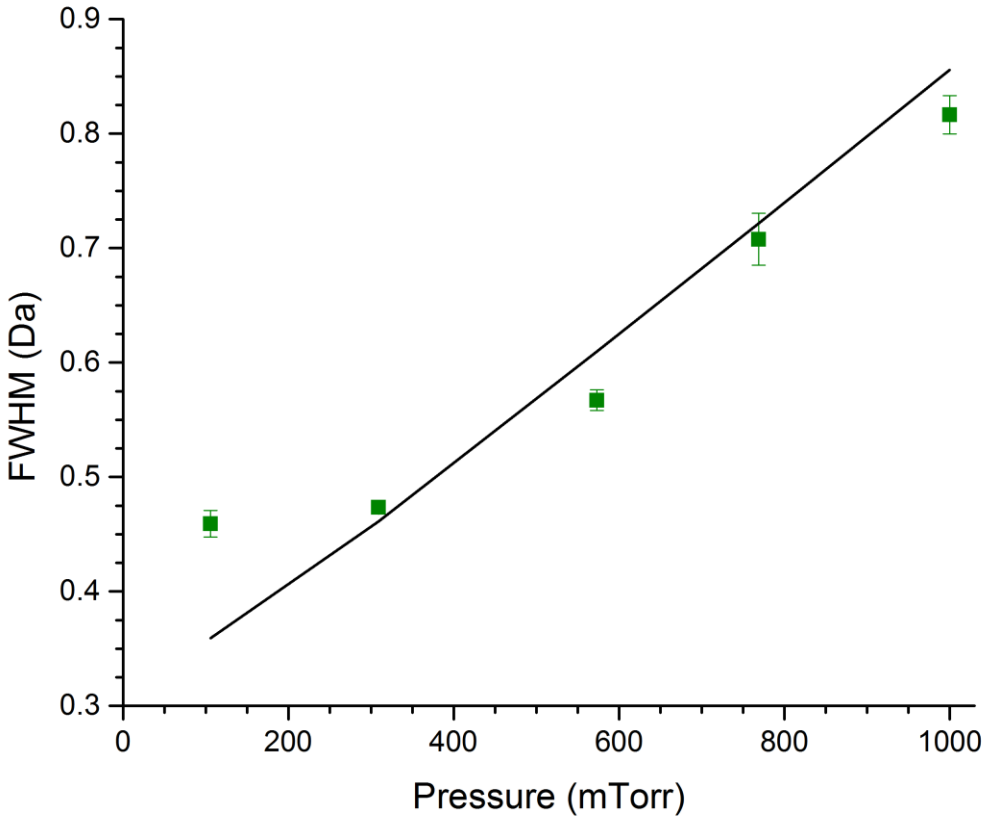

Figure 2.8: Peak widths (FWHM) for the octane peak at 41 Da as a function of buffer gas pressure (■) and fit with Equation 2.6 (——).

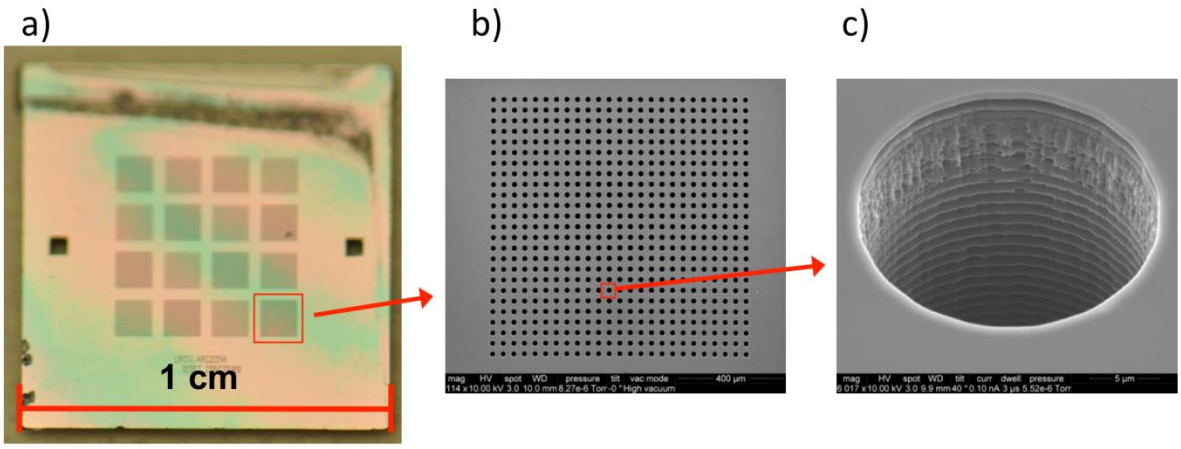

Figure 2.9: Images of the microionizer. a) Optical image showing the dimensions of the overall device and the 4 x 4 array of active features, b) SEM of one array of active features and, c) SEM image of a single microionizer feature where the scalloped sidewalls from DRIE Bosch serve as the emission points.

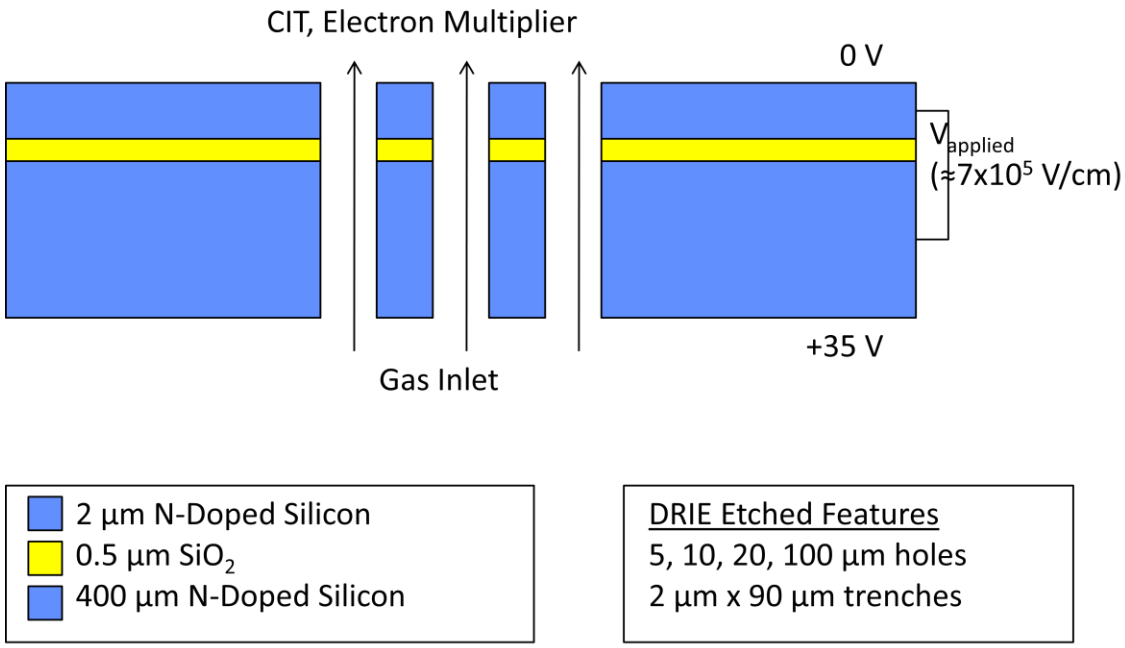

Figure 2.10: Schematic of microionizer. Two silicon layers are separated by a thin oxide layer to produce large electric fields suitable for inducing field emission. Through holes are etched by the DRIE Bosch process, producing scalloping that serves as emission points for field emission.

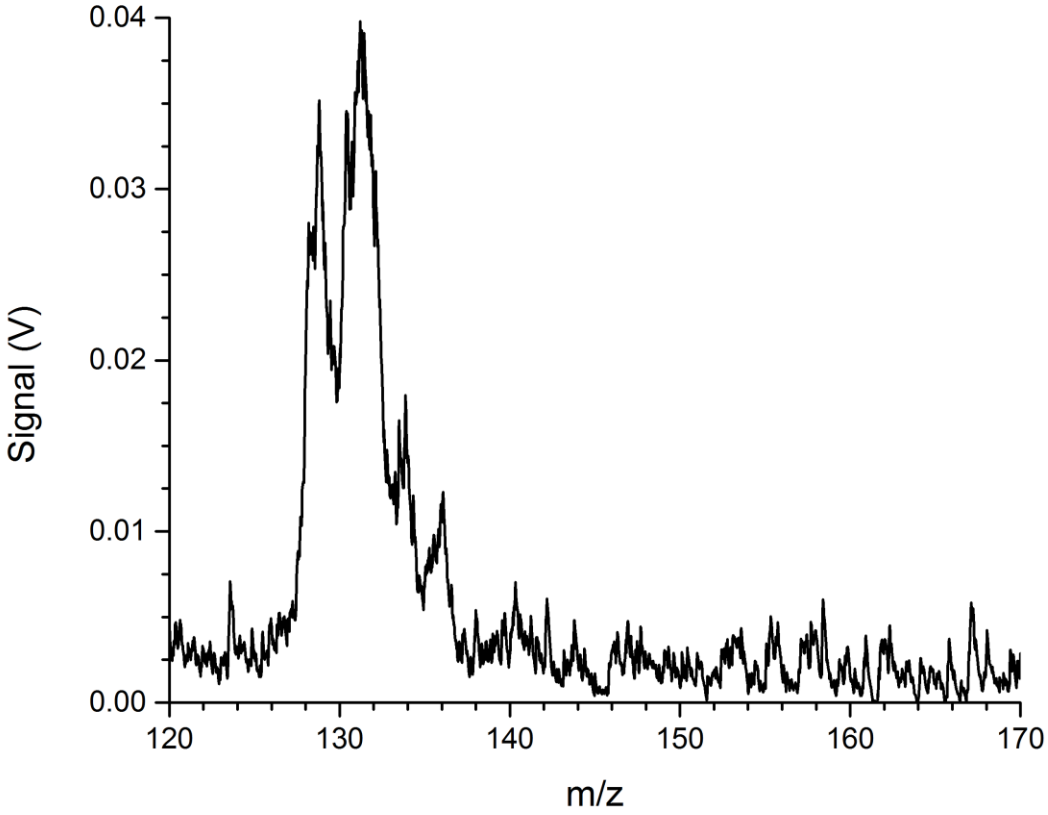

Figure 2.11: Mass spectra of xenon taken with microionizer and a r_o = 500 μm 19-element CIT array. Despite the helium pressure of 1.3 Torr, five xenon isotope peaks at 128, 129, 130, 132, and 134 Da are observed.

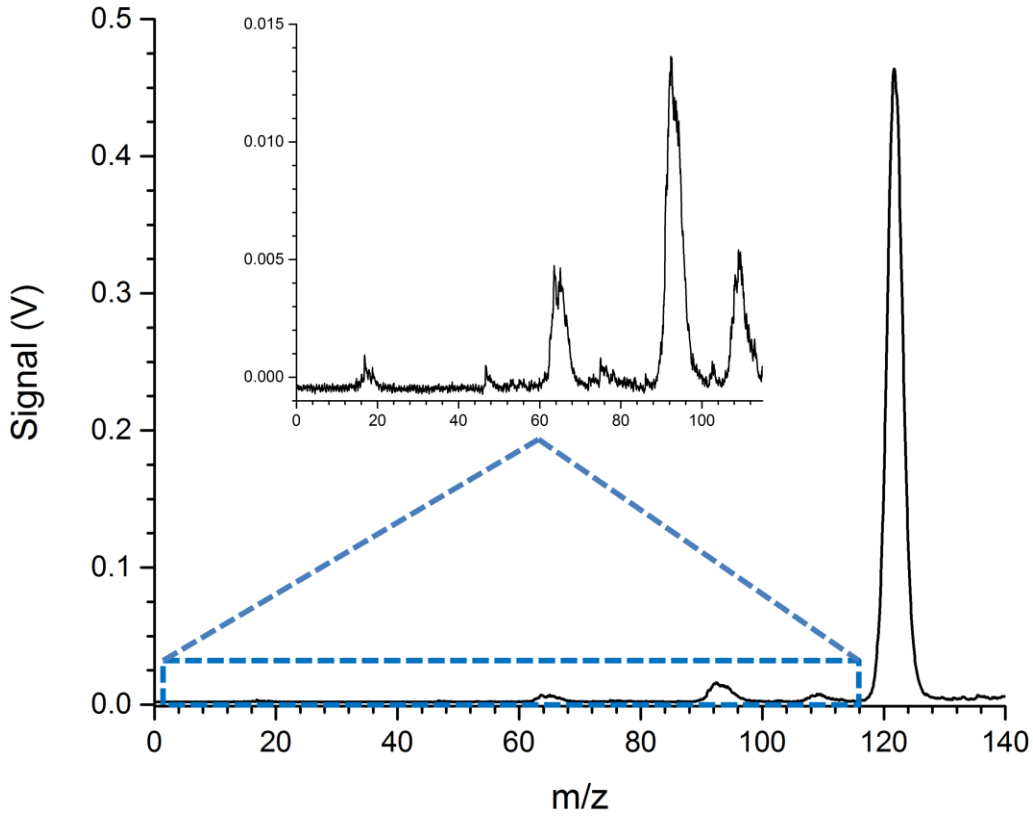

Figure 2.12: Mass spectra of DMMP, a chemical warfare agent simulant for the nerve gas VX taken with the microionizer at 1.3 Torr helium.

2.7 References

1. Lammert, S. A.; Wells, J. M., Experimental investigation into the performance of ion traps using air versus helium as the buffer gas. *Rapid Communications in Mass Spectrometry* **1996,** *10* (3), 361-371.

2. Wolfe, D. W., High-Pressure Cylindrical Ion Trap Mass Spectrometry Ph.D Dissertation, *UNC at Chapel Hill, North Carolina* **2012**.

3. Collins, R. D., Use of Electron Multipliers in Mass Spectrometry. *Vacuum* **1969,** *19* (3), 105-111.

4. Knight, A. K.; Sperline, R. P.; Hieftje, G. M.; Young, E.; Barinaga, C. J.; Koppenaal, D. W.; Denton, M. B., The development of a micro-Faraday array for ion detection. *International Journal of Mass Spectrometry* **2002,** *215* (1-3), 131-139.

5. Gao, L.; Song, Q. Y.; Noll, R. J.; Duncan, J.; Cooks, R. G.; Zheng, O. Y., Glow discharge electron impact ionization source for miniature mass spectrometers. *Journal of Mass Spectrometry* **2007,** *42* (5), 675-680.

6. Keil, A.; Talaty, N.; Janfelt, C.; Noll, R. J.; Gao, L.; Ouyang, Z.; Cooks, R. G., Ambient mass spectrometry with a handheld mass spectrometer at high pressure. *Analytical Chemistry* **2007,** *79* (20), 7734-7739.

7. Kornienko, O.; Reilly, P. T. A.; Whitten, W. B.; Ramsey, J. M., Electron impact ionization in a microion trap mass spectrometer. *Review of Scientific Instruments* **1999,** *70* (10), 3907-3909.

8. McLuckey, S. A.; Van Berkel, G. J.; Goeringer, D. E.; Glish, G. L., Ion-Trap Mass-Spectrometry - Using High-Pressure Ionization. *Analytical Chemistry* **1994,** *66* (14), A737-A743.

9. McLuckey, S. A.; Van Berkel, G. J.; Goeringer, D. E.; Glish, G. L., Ion-Trap Mass-Spectrometry of Externally Generated Ions. *Analytical Chemistry* **1994,** *66* (13), A689-A696.

10. Gill, L. A.; Amy, J. W.; Vaughn, W. E.; Cooks, R. G., In situ optimization of the electrode geometry of the quadrupole ion trap. *International Journal of Mass Spectrometry* **1999,** *188* (1-2), 87-93.

11. Tabert, A. M.; Griep-Raming, J.; Guymon, A. J.; Cooks, R. G., High-throughput miniature cylindrical ion trap array mass spectrometer. *Analytical Chemistry* **2003,** *75* (21), 5656-5664.

12. Curran, R. K., Mass-Spectrometer Investigation of Electron-Impact Processes at Pressures to 1 Mm Hg. *Journal of Chemical Physics* **1963,** *38* (12), 2974-2978.

13. Bleakney, W., A new method of positive ray analysis and its application to the measurement of ionization potentials in mercury vapor. *Physical Review* **1929,** *34* (1), 157-160.

14. Nier, A. O., A Mass Spectrometer for Isotope and Gas Analysis. *Review of Scientific Instruments* **1947,** *18* (6), 398-411.

15. Beran, J. A.; Kevan, L., Molecular Electron Ionization Cross Sections at 70-Ev. *Journal of Physical Chemistry* **1969,** *73* (11), 3866-3876.

16. Moxom, J.; Reilly, P. T. A.; Whitten, W. B.; Ramsey, J. M., Sample pressure effects in a micro ion trap mass spectrometer. *Rapid Communications in Mass Spectrometry* **2004,** *18* (6), 721-723.

17. Agostini, P.; Fabre, F.; Mainfray, G.; Petite, G.; Rahman, N. K., Free-Free Transitions Following 6-Photon Ionization of Xenon Atoms. *Physical Review Letters* **1979,** *42* (17), 1127-1130.

18. Bartelt-Hunt, S. L.; Knappe, D. R. U.; Barlaz, M. A., A review of chemical warfare agent simulants for the study of environmental behavior. *Critical Reviews in Environmental Science and Technology* **2008,** *38* (2), 112-136.

19. Xu, W.; Song, Q. Y.; Smith, S. A.; Chappell, W. J.; Ouyang, Z., Ion Trap Mass Analysis at High Pressure: A Theoretical View. *Journal of the American Society for Mass Spectrometry* **2009,** *20* (11), 2144-2153.

20. Xu, W.; Chappell, W. J.; Cooks, R. G.; Ouyang, Z., Characterization of electrode surface roughness and its impact on ion trap mass analysis. *Journal of Mass Spectrometry* **2009,** *44* (3), 353-360.

21. Wu, G. X.; Cooks, R. G.; Ouyang, Z., Geometry optimization for the cylindrical ion trap: field calculations, simulations and experiments. *International Journal of Mass Spectrometry* **2005,** *241* (2-3), 119-132.

22. Koizumi, H.; Whitten, W. B.; Reilly, P. T. A.; Koizumi, E., The effect of endcap electrode holes on the resonant ejection from an ion trap. *International Journal of Mass Spectrometry* **2009,** *281* (3), 108-114.

23. Arnold, N. S.; Hars, C.; Meuzelaar, H. L., Extended theoretical considerations for Mass resolution in the resonance ejection mode of quadrupole Ion Trap Mass Spectrometry. *Journal of the American Society for Mass Spectrometry* **1994,** *5* (7), 676-88.

24. Goeringer, D. E.; Whitten, W. B.; Ramsey, J. M.; McLuckey, S. A.; Glish, G. L., Theory of High-Resolution Mass-Spectrometry Achieved Via Resonance Ejection in the Quadrupole Ion Trap. *Analytical Chemistry* **1992,** *64* (13), 1434-1439.

25. Su, T.; Bowers, M. T., Theory of Ion-Polar Molecule Collisions - Comparison with Experimental Charge-Transfer Reactions of Rare-Gas Ions to Geometric Isomers of Difluorobenzene and Dichloroethylene. *Journal of Chemical Physics* **1973,** *58* (7), 3027-3037.

26. Londry, F. A.; Alfred, R. L.; March, R. E., Computer simulation of single-ion trajectories in paul-type ion traps. *Journal of the American Society for Mass Spectrometry* **1993,** *4* (9), 687-705.

27. Kornienko, O.; Reilly, P. T. A.; Whitten, W. B.; Ramsey, J. M., Micro ion trap mass spectrometry. *Rapid Communications in Mass Spectrometry* **1999,** *13* (1), 50-53.

28. Wells, J. M.; Badman, E. R.; Cooks, R. G., A quadrupole ion trap with cylindrical geometry operated in the mass selective instability mode. *Analytical Chemistry* **1998,** *70* (3), 438-444.

29. Gao, L.; Cooks, R. G.; Ouyang, Z., Breaking the pumping speed barrier in mass spectrometry: Discontinuous atmospheric pressure interface. *Analytical Chemistry* **2008,** *80* (11), 4026-4032.

30. Gomer, R., *Field emission and field ionization*. Harvard University Press: Cambridge,, 1961; p 195 p.

31. O'Donnell, A. F., L., Thomsen, D.J., O'Conner, P., C. Dastoor, Field ionization detectors: a comparative model. *Measurement Science and Technology* **2011,** *22*, 015901-.

32. Hartley, F. T. K., I., A nanoscale soft-ionization membrane: A novel ionizer for ion mobility spectrometers for space applications. *Procedings of the International Society for Optics and Photonics* **2002,** *4936*, 43-49.

33. Sheridan, S.; Bardwell, M. W.; Morse, A. D.; Morgan, G. H., A Carbon Nano Tube electron impact ionisation source for low-power, compact spacecraft mass spectrometers. *Advances in Space Research* **2012,** *49* (8), 1245-1252.

34. Kang, W.; Davidson, J. L.; Wong, Y. M.; Holmes, K., Diamond vacuum field emission devices. *Diamond and Related Materials* **2004,** *13* (4-8), 975-981.

35. Subramanian, K.; Kang, W. P.; Davidson, J. L.; Wong, Y. M.; Choi, B. K., Nanocrystalline diamond lateral field emission diode fabrication by dual micropatterning technique. *Diamond and Related Materials* **2007,** *16* (4-7), 1408-1412.

36. van Amerom, F. H. W. C., A., Cardenas, M., Bumgarner, J., and Short, R. T., Microfabrication of Cylindrical Ion Trap Mass Spectrometer Arrays For Handheld Chemical Analyzers. *Chemical Engineering Communications* **2007,** *195* (2), 98-114.

37. Kornienko, O.; Reilly, P. T. A.; Whitten, W. B.; Ramsey, J. M., Field-emission cold-cathode El source for a microscale ion trap mass spectrometer. *Analytical Chemistry* **2000,** *72* (3), 559-562.

38. Chen. L.Y.; Velasquez-Garcia, L. F., Wang, X., Teo, K., and Akinwande, A. I., A Micro Ionizer for Portable Mass Spectrometers using Double-gated Isolated Vertically Aligned Carbon Nanofilter Arrays. *Electron Devices Meeting, 2007. IDEM 2007. IEEE International* **2007**, 843-846.

39. Ghodsian, B., Parameswaran, M., Syrzycki, M., Gas detector with low cost micromachined field emission tips. *IEEE Electron Device Letters* **1998,** *19*, 241-243.

40. Einfled, W., Environmental Technology Verification Report Field-Portable Gas Chromatograph/Mass Spectrometer. *EPA/600/R-98/142* **1998**.

41. Laermer, F., Schilp, Andrea., U.S. Patent 5,501,893. **1996**.

42. Jansen, H. V.; de Boer, M. J.; Unnikrishnan, S.; Louwerse, M. C.; Elwenspoek, M. C., Black silicon method X: a review on high speed and selective plasma etching of silicon with profile control: an in-depth comparison between Bosch and cryostat DRIE processes as a roadmap to next generation equipment. *Journal of Micromechanics and Microengineering* **2009,** *19* (3).

43. Smith, J. N.; Noll, R. J.; Cooks, R. G., Facility monitoring of chemical warfare agent simulants in air using an automated, field-deployable, miniature mass spectrometer. *Rapid Communications in Mass Spectrometry* **2011,** *25* (10), 1437-1444.

44. Satake, H.; Toriumi, A., Common Origin for Stress-Induced Leakage Current and Electron Trap Generation in Sio2. *Applied Physics Letters* **1995,** *67* (23), 3489-3490.

45. Beck, A. H. W., High-Current-Density Thermioic Emitters: A Survey. *The Institution of Electrical Engineers* **1958,** *A paper No. 2750 R*.

46. Paschen, F., Ueber die zum Funkenübergang in Luft, Wasserstoff und Kohlensäure bei verschiedenen Drucken erforderliche Potentialdifferenz. *Annals of Physics* **1889,** *273* (5), 69-96.

47. DriskillSmith, A. A. G.; Hasko, D. G.; Ahmed, H., Nanoscale field emission structures for ultra-low voltage operation at atmospheric pressure. *Applied Physics Letters* **1997,** *71* (21), 3159-3161.

CHAPTER 3. DEVELOPING HPMS WITH NITROGEN AND AIR BUFFER GASES

3.1 Introduction

Mass resolution and SWaP concerns play an important part in developing a handheld MS instrument. As such, the choice of buffer gas is important since it helps determine possible ionization sources and affects instrument size and weight. Helium is primarily used in mass spectrometry because of its low mass which results in largely inelastic collisions that reduce ion kinetic energy without significant momentum changes.[1] This results in better mass resolution than can be achieved with larger buffer gases such as nitrogen or air. In a laboratory setting, maximizing the analytical performance of the instrument is crucial so the large gas tanks required for long experimental runs is not a significant limitation. For a handheld mass spectrometer, the instrument metrics change and SWaP concerns play a more prominent role.

Using helium for handheld operation would require an external tank, sized and/or pressurized proportionally to gas flow through the instrument and run time desired. This would add significantly to the size and weight of the instrument.[2-3] Nitrogen and air are attractive buffer gases as they can be easily obtained in the field. Nitrogen generators can be used for filling nitrogen canisters attached to the instrument, extending their field run time capability but at the cost of higher power requirements.[4-5] In terms of MS performance, nitrogen has a larger molecular mass, collisional cross section, and polarizability compared to

helium. Thus, more momentum is transferred to analyte ions corresponding to decreased mass resolution.

Air as a buffer gas has nearly identical collisional properties as nitrogen with similar effects on mass resolution.[6-7] The use of air does eliminate the need for gas cylinders or gas generation equipment to supply the buffer gas thereby improving the SWaP parameters. A potential drawback is the presence of chemically reactive oxygen, limiting ionization sources to oxygen tolerant sources. For example, thermionic emitters widely used for helium operation cannot tolerate air operation. Ambient air is readily available in the field and analytes can be analyzed directly without dilution, improving sensitivity. Concerns for ambient air operation include potential humidity effects on ion trap performance, and the need for particle filtration.

The same microscale ion traps (r_o = 500 µm, z_o = 645 µm) discussed in Chapter 2 were used to explore operation with nitrogen and air buffer gasses at high pressures.[8] Previous work with millimeter scale ion traps has demonstrated MS with nitrogen and air buffer gases, although only up to 50 mTorr.[9-11] For this work in characterizing and developing MS operations in nitrogen and air buffer gasses, the differential chamber design was once again used. Tungsten filaments were initially used to explore nitrogen buffer gas effects since they are cost effective and have been successfully used with high pressure helium operation. Ultimately, due to their limitations of finite lifetimes at elevated operating pressures, incompatibility with air due to oxygen reactivity, and reduced signal strength, filament ionizers are not suitable for use with a handheld instrument. To address these limitations, a glow discharge electron source compatible with air buffer gas and high pressures was incorporated into the system as the ionization source.

3.2 Filament Electron Source

While the ultimate goal is to operate the microscale ion traps at high pressures of ambient air, there are several intermediate development steps. The first step is to demonstrate microscale CIT operation at low pressures of nitrogen. Nitrogen was used since filaments do not tolerate oxygen. The CWA simulant CEES was initially used as the analyte since sufficient MS signal was achieved at low and elevated helium pressures. Mass spectra for CEES was acquired at 7 mTorr for both helium and nitrogen buffer gases (Figure 3.1). For the helium mass spectra, major peaks were observed at 126 Da (chlorine isotope peak), 125 Da (carbon-13 isotope of the molecular ion), 124 Da (molecular ion), 89 Da (loss of chlorine), and 75 Da (loss of methyl chloride). Switching to nitrogen buffer gas, the peaks at 125 Da and 89 Da are no longer distinguishable with the reduced mass resolution.[12-13] However, three of the five peaks are still clearly visible at 126 Da, 124 Da, and 75 Da making identification still a possibility. The signal intensities for the largest peaks in both buffer gases (75 Da) were 230 mV for helium and 190 mV for nitrogen, or 19% lower for nitrogen. This loss in signal intensity and mass resolution for mass spectra acquired with nitrogen buffer gas was anticipated because of the larger neutral molecule size.

For high pressure nitrogen experiments, the signal strength decreased more significantly compare to the signal strength decrease seen with higher helium buffer gas pressure. This is probably due to the larger nitrogen gas molecules (28 Da vs. 4 Da for helium) where more electrons are lost to collisions with nitrogen gas molecules between the filament and ion trap than with helium. To overcome this loss in signal, the electron energy was further increased from -125 V to -200 V. Increasing the electron energy by this additional -75 eV was enough to compensate for the increased collisional scattering. The

ionization filaments also tolerated the more negative biases better in nitrogen than helium. However, lifetimes were on the order of 10 to 30 hours at 1 Torr, compared to months for filaments operated at pressures near 1 mTorr.

Methyl salicylate (MES, wintergreen oil), a chemical warfare agent simulant for mustard gas and soman, was used to characterize mass spectra up to 1.0 Torr of nitrogen.[14] A series of spectra were recorded as a function of nitrogen pressure from 130 mTorr to 1.0 Torr (Figure 3.2). The molecular ion (152 Da) and two fragment peaks at 120 Da ($C_6H_4CO_2^+$) and 92 Da ($C_6H_4CO_2^+$) were observed at each pressure. Peak widths approximately tripled over the pressure range, even with optimized axial RF conditions at each operating pressure.[10, 15] Signal strength remained sufficient to acquire mass spectra across the pressure range. The key challenge for generating mass spectra in high pressure nitrogen conditions was achieving sufficient ionization. This limitation required improved electron coupling to the CIT plus frequent filament replacement, several times per week, as filaments were run at higher powers significantly reducing lifetimes. These limitations establish the need for development of a reliable ionization source with better electron emission, longer lifetimes, and lower power requirements.

3.3 Glow Discharge-Electron Ionization (GD-EI)

The microscale CIT was operated at high pressures of nitrogen with filaments, but as noted, there are several drawbacks to filaments including sensitivity, lifetime, and incompatibility with air. Glow discharge ionization is an attractive ionization source since it draws low power (~100 mW) and is compatible with ambient pressures of air. Mass spectrometers with glow discharge sources have been applied to elemental analysis of solid

materials with applications ranging from nuclear materials to trace material analysis in semiconductors.[16-17] Atmospheric sampling glow discharge has been used to study atmospheric VOCs from pollutants and explosives.[18-19] Glow discharge can also be used as an electron impact ionization source (GD-EI). GD-EI has previously been coupled to millimeter scale ion traps to detect chemical warfare agent simulants and toxic industrial compounds.[11, 20-22] With higher efficiency and pressure tolerance, GD-EI has promise as a HPMS ionization source.

The glow discharge source consists of two electrodes (brass or stainless steel). Each electrode has a diameter of 3 cm and thicknesses of 2 mm (electrode furthest from the ion trap) and 3 mm (electrode nearest the ion trap). The aperture in the electrode near the ion trap was 360 μm (diameter). The two electrodes are separated by a 1 cm teflon spacer. For a glow discharge source operated at 1 Torr, the 1 cm separation minimizes the voltage required to form a plasma as described by Paschen's Law.[23] The glow discharge source is adaptable for other pressure regimes by either increasing the electrode separation (lower pressures) or decreasing the separation (higher pressures).

3.3.1 Emission Studies

Figure 3.3a shows the adaptation of the differential chamber mass spectrometer incorporating the glow discharge source for the nitrogen/air buffer gas experiments. For electron emission, the electrode nearest the CIT or electron multiplier was biased at -175 V and approximately 300 V was pulsed to the second electrode during ionization to produce the electrical fields necessary for glow discharge. The minimum voltage required for stable emission at each pressure tested was used.

Emission characteristics for the glow discharge source were compared to tungsten filaments. A new experimental setup was used to characterize current density by measuring the current at the ring electrode (Figure 3.3b). Ionization pulses were applied to the glow discharge electrodes to generate electrons directed into the CIT. A SRS570 Standard Research Systems preamplifier attached to the ring electrode was then used to amplify and convert the current to voltage that was recorded using a data acquisition card.

Performance of the glow discharge source was characterized at high buffer gas pressures (500 mTorr to 2 Torr) in both nitrogen and air and compared to a tungsten filament operated in helium. Figure 3.4 shows the current densities measured at the ring electrode as a function of helium (filament), nitrogen (glow discharge) and air (glow discharge) pressures. The glow discharge source in air and nitrogen produced higher current densities than the tungsten filament in helium over the range of pressures. The highest current density for the filament was 35 nA/cm^2 at 200 mTorr while the lowest current densities were approximately 100 nA/cm^2 for both nitrogen and air at 500 mTorr. Over the pressure range measured, maximum current densities were 190 nA/cm^2 for air at 600 mTorr and 130 nA/cm^2 for nitrogen at 800 mTorr. The current density in both air and nitrogen decreases at pressures beyond roughly 800 mTorr with the glow discharge current density in air favored over nitrogen by less than a factor of 2. At the target pressure of 1.0 Torr for a handheld instrument, the current density for helium was 5 nA/cm^2 or 184 % lower than nitrogen (110 nA/cm^2) and 189 % lower than air (170 nA/cm^2). Based on these current density measurements its clear the lack of ionization energy emitted by the filament impairs acquiring spectra at high pressure with helium buffer gas.

While current density available for ionization largely affects signal strength, there are other experimental variables available for improving signal. The current densities achieved in both nitrogen and air buffer gases using glow discharge could lead to ionization times on the order of a few milliseconds. With just under 2x the ionization strength as air, using a slightly longer ionization time under nitrogen conditions should lead to higher signals without adding significant analysis time. In both cases, sufficient current densities using the glow discharge ionizer are generated at the pressures of interest near 1 Torr to be a viable option in a handheld device.

A comparison between the SWaP of a GD source and filament source is more favorable in the GD source direction. A handheld mass spectrometer with minimal power draw associated with ionization while still capable of generating signal would be preferable. The glow discharge source produces higher current densities with lower power draw since the source can be pulsed while a filament is operated continuously. At 1 Torr nitrogen and air, average power requirements for glow discharge were 160 and 61 mW, respectively. The difference in power requirements between nitrogen and air was likely due to electrode fouling from extended use. In comparison, the tungsten filament required 5.3 W at 1 Torr helium buffer gas and in addition creates high temperatures as a condition of operation. The reduction in power requirements when using the glow discharge source will prolong battery life in a handheld portable device.

3.3.2 High Pressure Comparison with Different Buffer Gases

Mass spectra for *p*-xylene were taken with helium, nitrogen, and air buffer gases at elevated pressures. First, mass spectra were obtained with helium buffer gas as a point of

reference from 510 mTorr to 1.0 Torr (Figure 3.5). The spectra were normalized to account for ionization differences with pressure. The pressure range was chosen to cover the lowest pressures where the glow discharge source can operate with nitrogen and air, while the highest pressures were determined by electrical breakdown limitations. For helium, a tungsten filament was used for ionization since arcing was observed with the glow discharge source, likely an effect of instabilities near the electrode surface.[26] Across the pressure range the molecular ion peak was observed at 106 Da, and a fragment peak was seen at 91 Da (loss of a methyl group) with a slight increase in peak widths with higher pressures.

Figures 3.6 and 3.7 show mass spectra with increasing nitrogen (490 mTorr to 1.9 Torr) and air pressures (490 mTorr to 1.7 Torr). The mass spectra are normalized for visual comparison. The mass spectra have the same peaks including the molecular ion peak (106 Da) and two fragment peaks (91 Da and 77 Da, loss of two methyl groups). Relative peak intensities remain nearly constant despite a factor of 4 increase in operating pressure. A comparison of spectra between the buffer gases at 1.0 Torr is shown in Figure 3.8. At 1 Torr, isotopic peaks were resolved with helium but not nitrogen and air buffer gas. The 77 Da peak was not observed with helium, although different fragmentation with different buffer gases is not unexpected.[27] The different ionization source and conditions could also have large effects on mass spectra. The key difference between helium and nitrogen and air was the larger mass resolution loss observed with elevated nitrogen and air pressures,

The resolution loss at these higher pressures is not unexpected primarily due to increased ion-neutral collisions and the increase in buffer gas size. The peak width for the molecular ion peak (106 Da) was characterized as a function of buffer gas pressure (Figure 3.9). The 106 Da peak was chosen since the 91 Da and 92 Da relative intensities were found

to change with operating conditions such as ionization time and pressure. The axial RF amplitudes were experimentally optimized for each pressure. Peak widths of *p*-xylene in helium buffer gas were also analyzed for comparison with the nitrogen and air buffer gas results. A roughly linear increase in peak width with pressure was seen for each buffer gas. The *p*-xylene peak widths are inherently larger with nitrogen and air buffer gases due to the more inelastic collisions between trapped ions and neutral buffer gasses compared to helium.[28] Comparing peak widths for the 106 Da peak at 1.0 Torr, in helium the peak width was 0.62 Da compared to 5.15 Da in nitrogen. This corresponds to approximately a factor of 8 broader peaks. In comparison, the 106 Da peak width with air buffer gas was 5.04 Da, only 2.2 % different than nitrogen, which was expected since both air and nitrogen buffer gases have similar collisional properties.[28] These results matched previous theoretical and experimental research for helium buffer gas that showed a linear peak width increase with pressure (Chapter 2).

Although increased peak widths make chemical analysis more difficult, sufficient resolution for chemical identification is retained using the larger mass buffer gases. This reduction in mass resolution is a necessary tradeoff to achieve lower pumping requirements needed for handheld portability. Chemometric techniques currently employed in other areas of mass spectrometry could be implemented to improve chemical analysis.[29] To offset the lower resolution, tandem mass spectrometry techniques would help with identification by improving background noise and deconvoluting complicated mixtures.[8] The RF drive frequency could also be increased to improve peak widths with the tradeoff of higher RF power, as will be discussed in more detail in Chapter 4.

Sensitivity was also considered because when ion traps are miniaturized, charge capacity fundamentally decreases linearly with z_o. Charge capacity is also lost when ion traps are operated with decreased pseudopotential well depths.[30-31] Furthermore, for a handheld instrument where fast analysis times are important, very short ionization times are desired to increase the duty cycle. To characterize sensitivity with nitrogen and air buffer gases, peak areas and signal-to-noise ratios were calculated for *p*-xylene as a function of pressure (Figures 3.10 and 3.11). With the high current densities generated by the GD source in both nitrogen and air (Figure 3.4), short ionization times were possible. While air has a higher current density than nitrogen at buffer gas pressures above 600 mTorr, the ionization time for both was 2 ms, corresponding to only a 14% duty cycle for the glow discharge source. Therefore, peak areas were expected to be greater in air than in nitrogen at buffer gas pressures above 600 mTorr though the signal strength with nitrogen could be improved by increasing the ionization time.

Peak area was found to be a function of both current density and CIT trapping characteristics at higher pressures. Near 500 mTorr buffer gas pressure, integrated peak areas were almost equivalent as are the glow discharge current densities between gases (Figure 3.4). From 800 mTorr to 1.5 Torr there was a linear increase in integrated peak area for both buffer gases with air having a slightly larger peak area, likely related to higher current densities relative to nitrogen at these pressures. Figure 3.4 shows that current densities for air at pressures above 1.5 Torr are approximately a factor of 2 larger than nitrogen. However, Figure 3.10 shows this did not translate to double the integrated peak area. A possible explanation is that the miniaturized ion traps are approaching their charge capacity and are no longer trapping additional ions efficiently. While current density

decreases above 800 mTorr for both buffer gases, integrated peak area continued to increase until the pressure reached 1.5 Torr, suggesting decreased mean free paths and more collisions between ions and buffer gas molecules causing improved trapping efficiency in this range. A second reason could be higher order fields present in the cylindrical geometry becoming more important to signal strength at high buffer gas pressures.[32-34]

Signal-to-noise was calculated as the ratio of integrated peak area to the standard deviation of the baseline over a 10 Da mass range from 60 to 70 Da. Signal-to-noise increased by a factor of 4 when operating pressure increased from 500 mTorr to 1.7 Torr for both buffer gases. Above 1 Torr instrument instabilities became a larger factor with both buffer gases. Of particular note, the electron multiplier was operating above its pressure rating that resulted in an increase in baseline noise, indicated by the larger error bars. A higher-pressure tolerant detector such as a Faraday cup would alleviate these problems.[35-37] Despite the increase in noise, improved sensitivity and signal-to-noise were achieved operating at higher pressures. This has several benefits for a handheld mass spectrometer including lower limits of detection and shorter analysis times, both of which contribute to lower SWaP requirements.[38]

A mixture of VOCs (toluene, 2,6-lutidine, N,N-dimethylaniline, naphthalene) was analyzed in 1 Torr room air buffer gas to demonstrate chemical identification despite the loss of resolution at higher pressures. A continuous atmospheric inlet was used to introduce analytes and room air at 1 Torr to the ionization and mass analysis chamber. Figure 3.12 shows mass spectra of the four-analyte mixture along with the four individual samples. The individual spectra were normalized to account for different ionization and trapping efficiencies. Of the four, naphthalene and toluene were ionized and trapped less efficiently

than N,N-dimethylaniline and 2,6-Lutidine. This is evident in the four-analyte mixture spectra where the peak heights for naphthalene and toluene are smaller compared to N,N-dimethylaniline and 2,6-lutidine. Each of the four components had characteristic peaks: 91 Da (toluene), 107 Da (2,6-lutidine), 120 Da (N,N-dimethylaniline), and 128 Da (naphthalene). Based on those peaks being present or absent, the individual components found in this mixture could be identified.

For more complex mixtures, fragmentation ratios and patterns could be used for analysis, while chromatographic coupling to add another separation and identification dimension would further improve ion trap tolerance to resolution losses. Figure 3.13 shows mass spectra for five simple VOCs (acetophenone, limonene, mesitylene, *o*-xylene, and *p*-xylene) sampled in 1.0 Torr ambient air. For each molecule 3-5 characteristic peaks are seen over the 70 Da mass range from 70 Da to 140 Da. There are distinct differences in the m/z values between acetophenone, limonene, and mesitylene. Even though *p*-xylene and *o*-xylene have the same peaks at 106 Da, 91 Da, and 77 Da, with *o*-xylene the molecule ion peak (106 Da) is consistently the largest peak in its spectra, while the 91 Da fragment peak is consistently the largest for *p*-xylene. Relative peak intensities are still useful for differentiating acetophenone and mesitylene since the mass resolution makes accurate mass assignments difficult, while limonene had five peaks instead of three peaks. Identification of these components in ambient air could be accomplished more reliably with improved mass resolution.[12] This should achieve by increasing the RF frequency beyond 10 MHz and is the subject of Chapter 4.

3.4 Conclusions

HPMS with nitrogen and air buffer gasses covering a pressure range suitable for hand held mass spectrometry was shown. Initial buffer gas studies demonstrated HPMS with tungsten filaments. CEES spectra were recorded at 7 mTorr in both nitrogen and air and found to have similar mass spectra though spectra with helium demonstrated better mass resolution and signal strength as expected. The electron energy was increased from -125 eV to -200 eV to overcome the reduction in electron current density reaching the ion traps due to collisions effects. As with helium, mass spectra characteristics including peak locations and fragmentation were similar spanning from 500 mTorr up to 1 Torr, while peak widths increased by a factor of 3.

To address filament limitations at high pressures of nitrogen, and to study air as a buffer gas, a glow discharge electron ionization source was incorporated into the instrumentation. It offers lower power requirements and operates well with high pressures of nitrogen and air. HPMS of *p*-xylene were acquired in nitrogen and air up to pressures near 2 Torr. The best sensitivity and signal-to-noise ratios were near the highest pressures (2 Torr) studied though peak widths increased by a factor of 2 from 500 mTorr to 2 Torr buffer gas. A 4-component analyte mixture was analyzed in 1 Torr of ambient air and each component was easily distinguished by the microscale ion trap. Mass spectra of five analytes were also characterized at 1 Torr of ambient air. The results and previous theoretical work discussed in Chapters 1 and 2 suggest the potential importance of using higher RF drive frequencies for improvement of mass resolution at these operating pressures. Continuing to scale towards smaller trap sizes should significantly lower RF voltage amplitude requirements, making higher frequency operation practical.

3.5 Figures

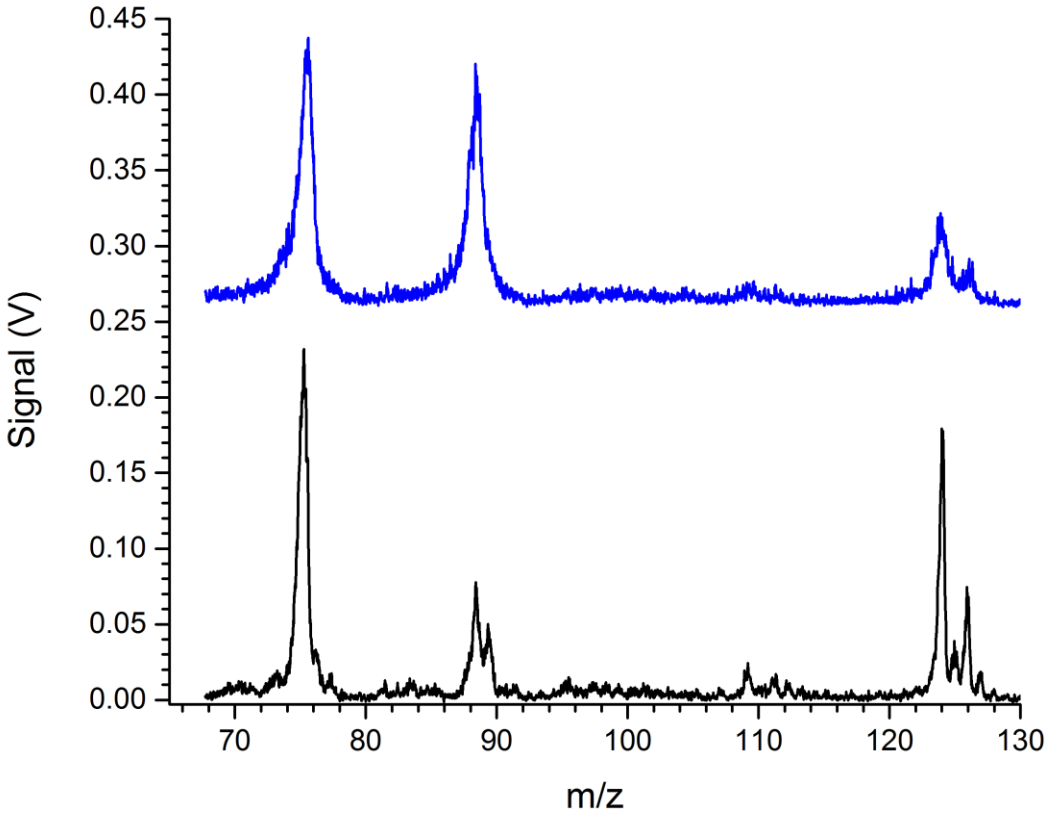

Figure 3.1: Comparison of CEES mass spectra taken at 7 mTorr helium (——) and nitrogen (——) buffer gases. Significant peak broadening because of ion-neutral collisions is seen due to the larger nitrogen molecules (28 Da) compared to helium molecules (4 Da).

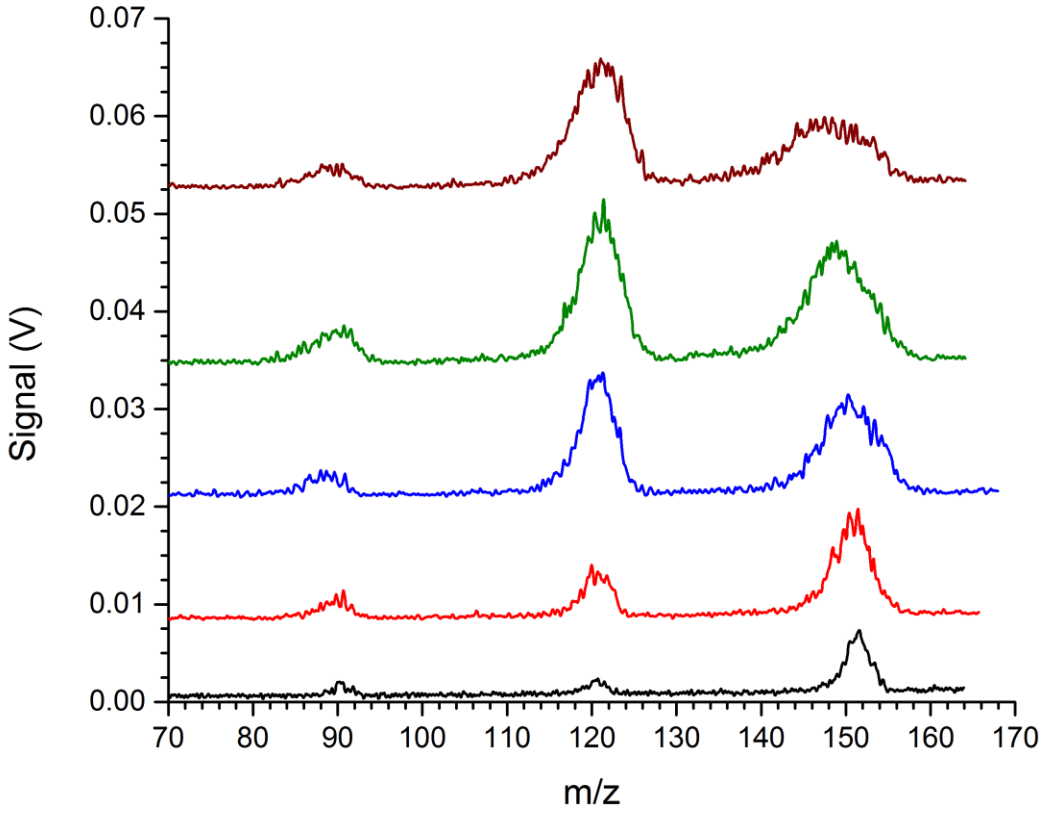

Figure 3.2: Mass spectra of MES, a chemical warfare agent simulant for mustard gas and soman with increasing nitrogen buffer gas pressures at 130 mTorr (——), 320 mTorr (——), 510 mTorr (——), 700 mTorr (——), and 1.0 Torr (——).

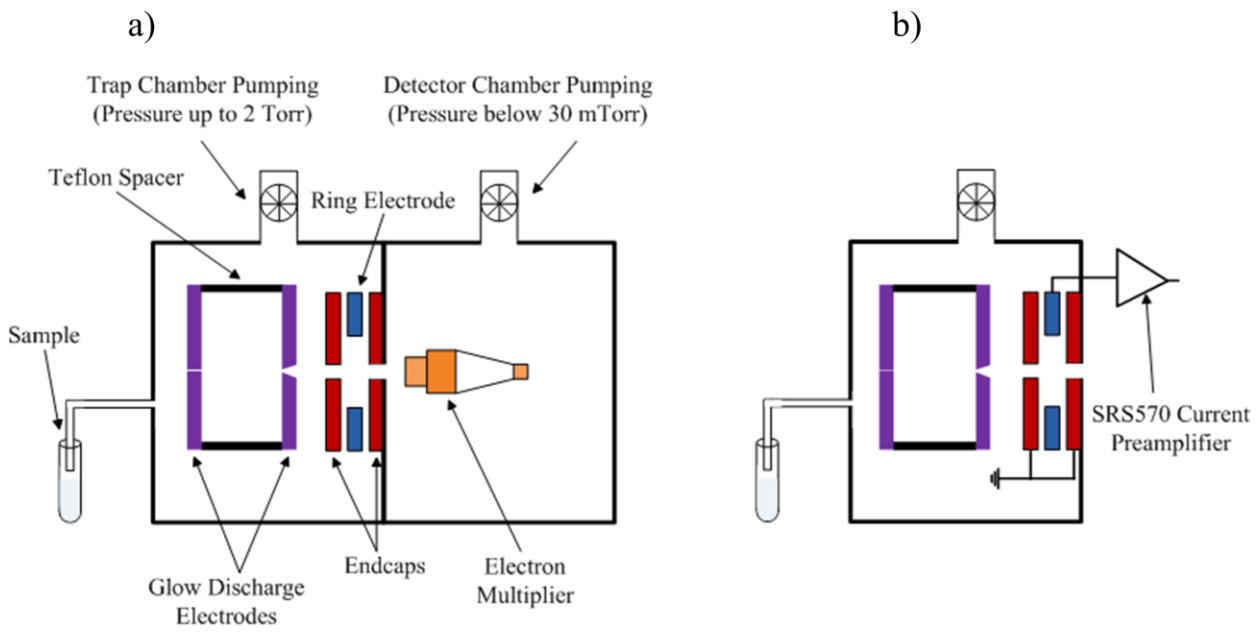

Figure 3.3: Instrument setup for glow discharge as the ionization source (ions and electrons) showing critical components (a) differential chamber with glow discharge ionization source, CIT, and electron multiplier detection (b) experimental setup for glow discharge current density measurements.

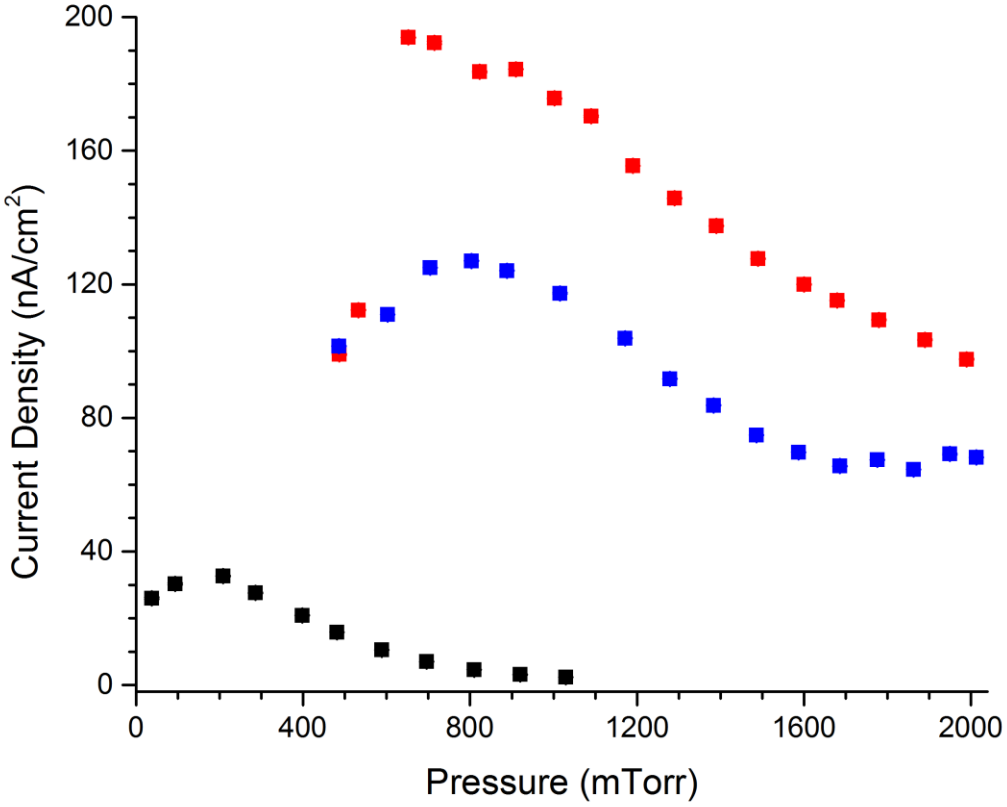

Figure 3.4: Current density characteristics for glow discharge electron impact ionization source in nitrogen (■), air (■), and emission from a tungsten filament in helium (■)buffer gas at increasing pressures.

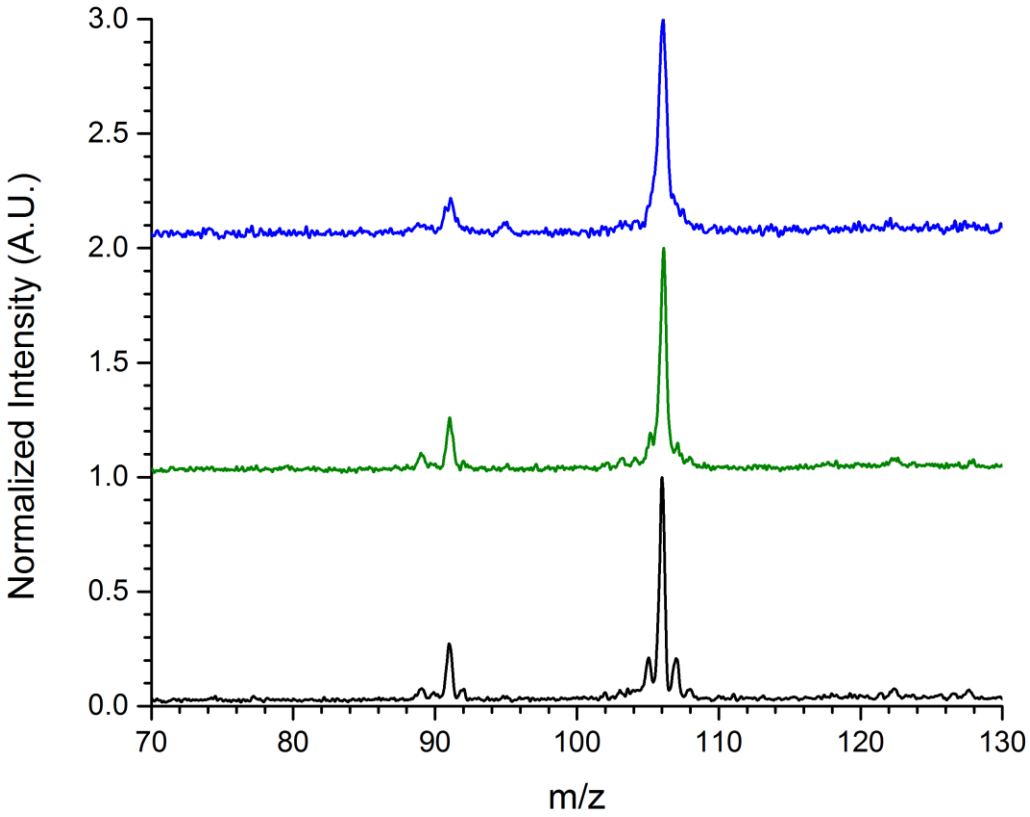

Figure 3.5: Mass spectra of *p*-xylene with increasing helium buffer gas pressures at 510 mTorr (———), 820 mTorr (———), and 1.0 Torr (———).

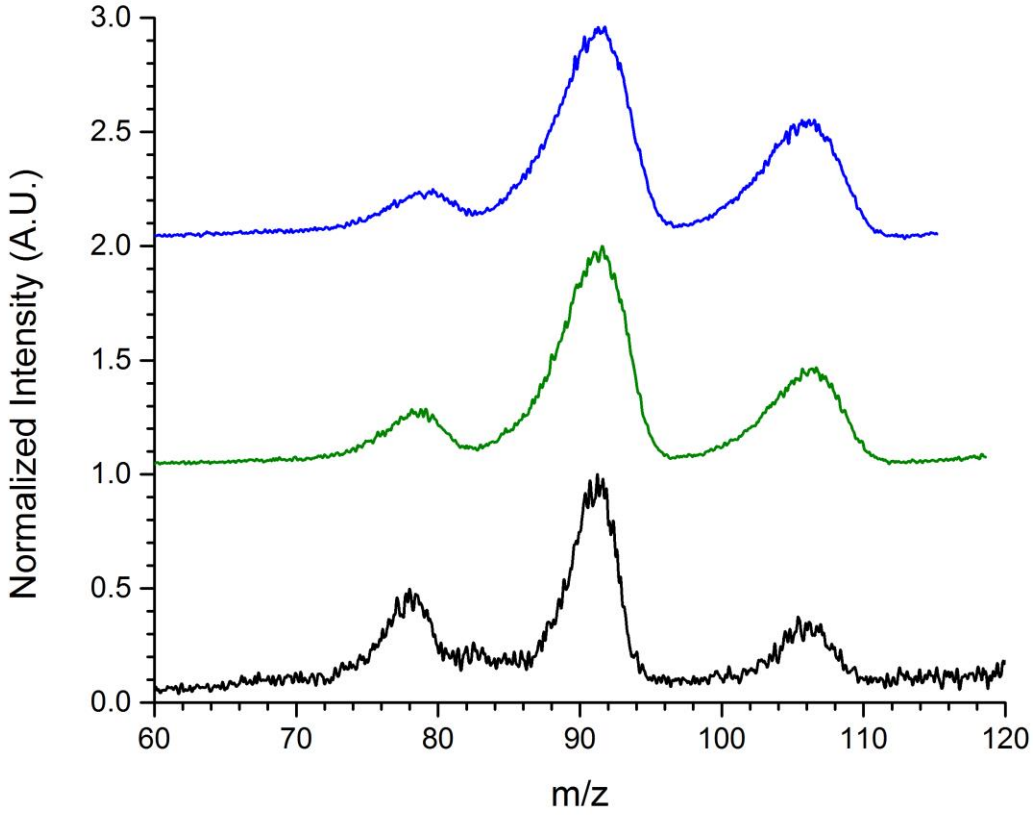

Figure 3.6: Mass spectra of *p*-xylene with increasing nitrogen buffer gas pressures at 490 mTorr (———), 1.3 Torr (———), and 1.9 Torr (———).

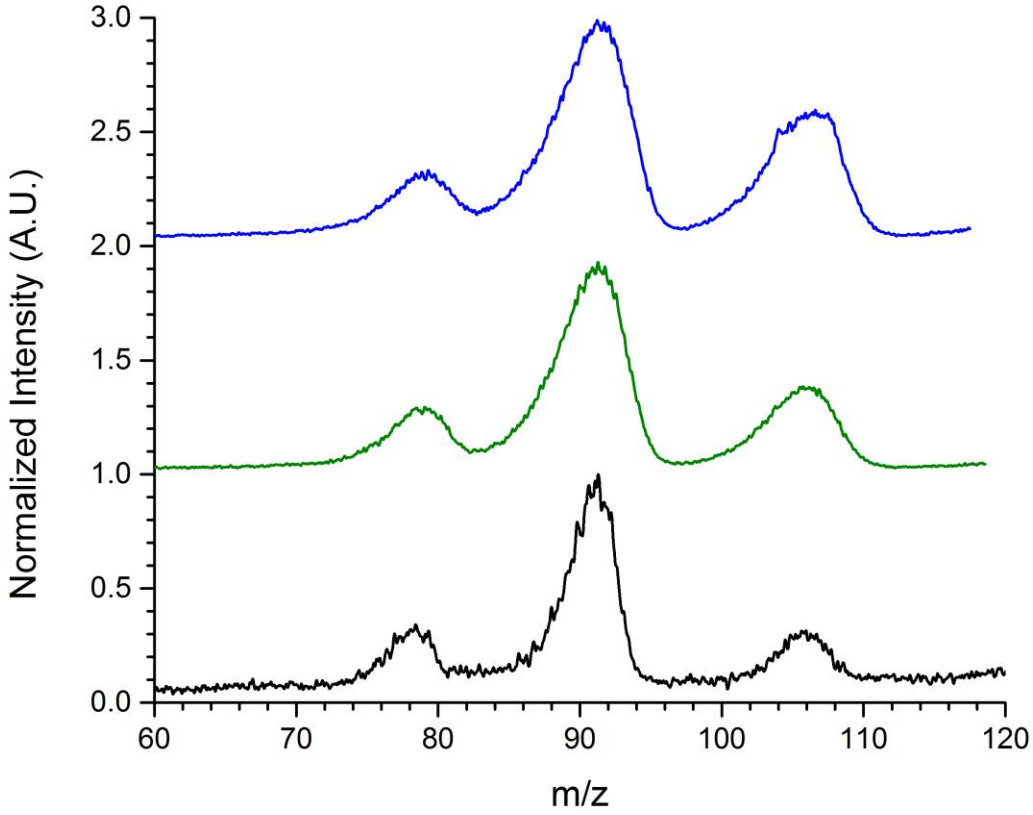

Figure 3.7: Mass spectra of *p*-xylene with increasing air buffer gas pressures at 490 mTorr (———), 1.3 Torr (———), and 1.7 Torr (———).

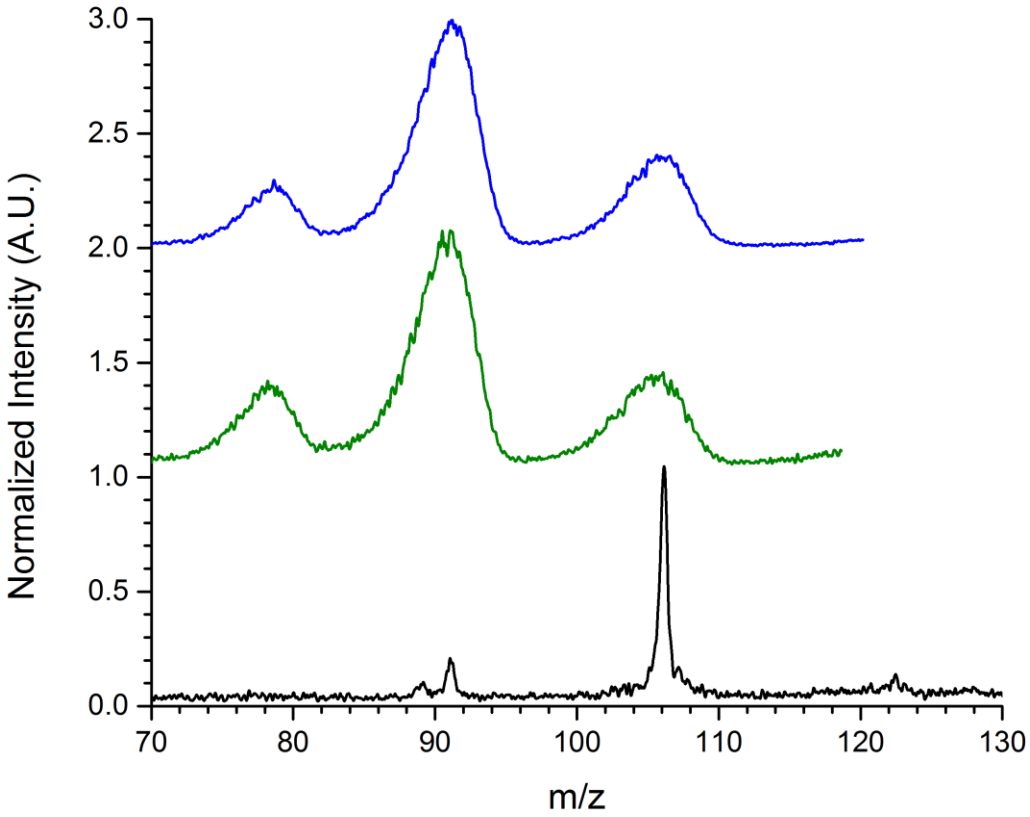

Figure 3.8: Comparison of mass spectra of *p*-xylene in 1.0 Torr buffer gas for helium (——), nitrogen (——), and air (——).

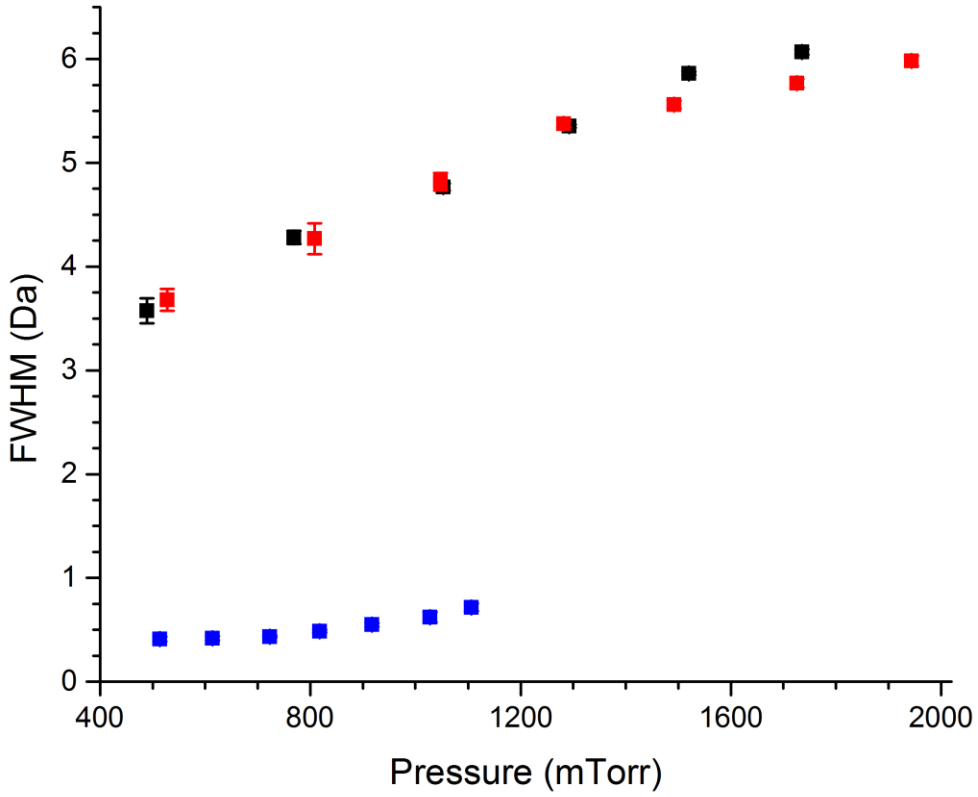

Figure 3.9: Peak widths for *p*-xylene 106 Da in helium (■), nitrogen (■) and air (■) buffer gases as a function of increasing pressure.

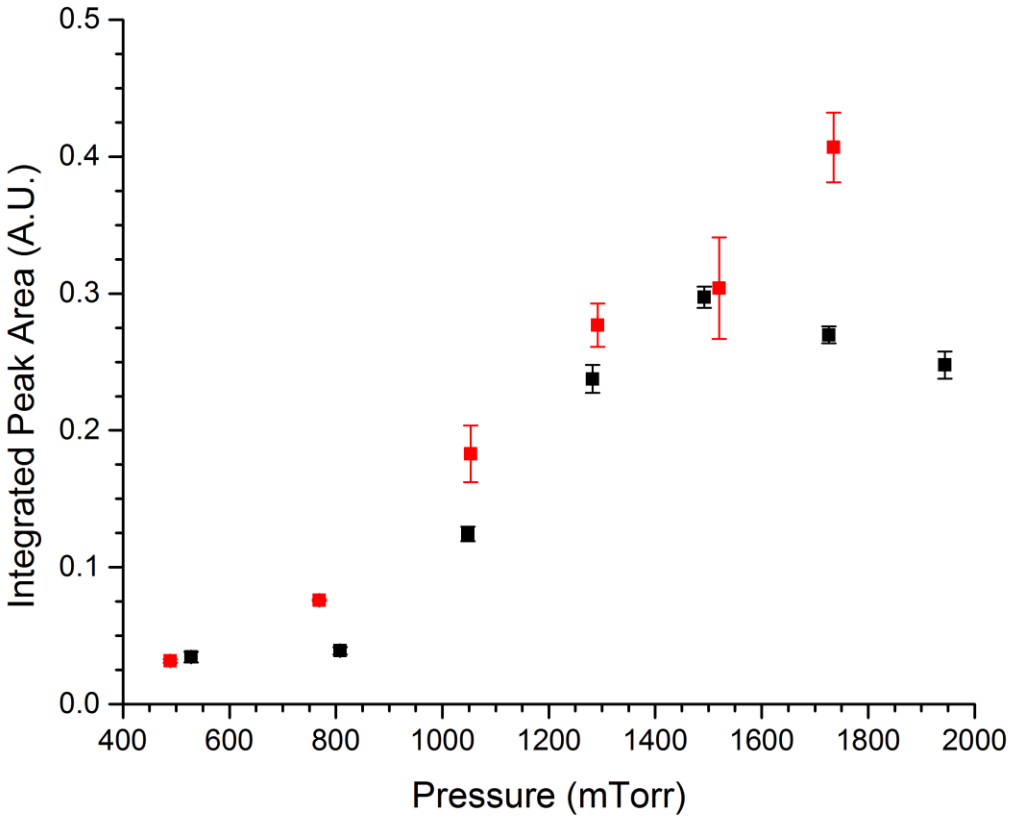

Figure 3.10: Integrated peak area as a function of pressure with glow discharge ionization in nitrogen (■) and air (■) buffer gases.

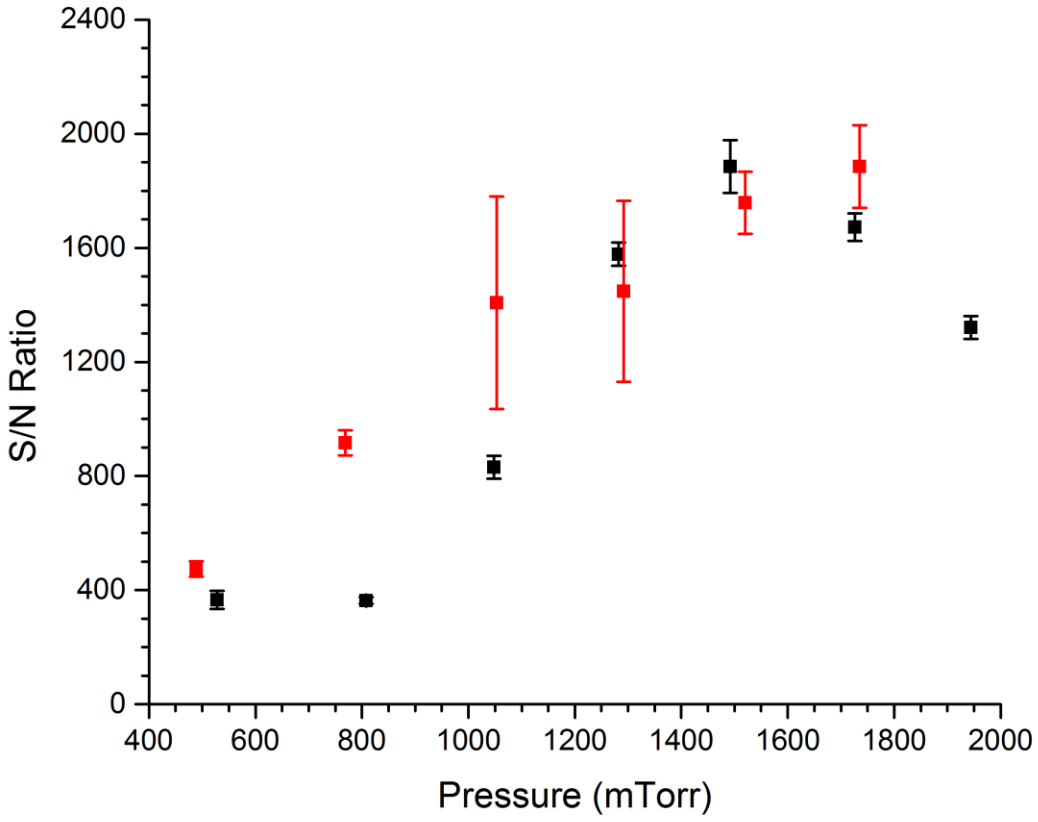

Figure 3.11: Signal-to-noise ratio as a function of pressure with glow discharge ionization in nitrogen (■) and air (■) buffer gases.

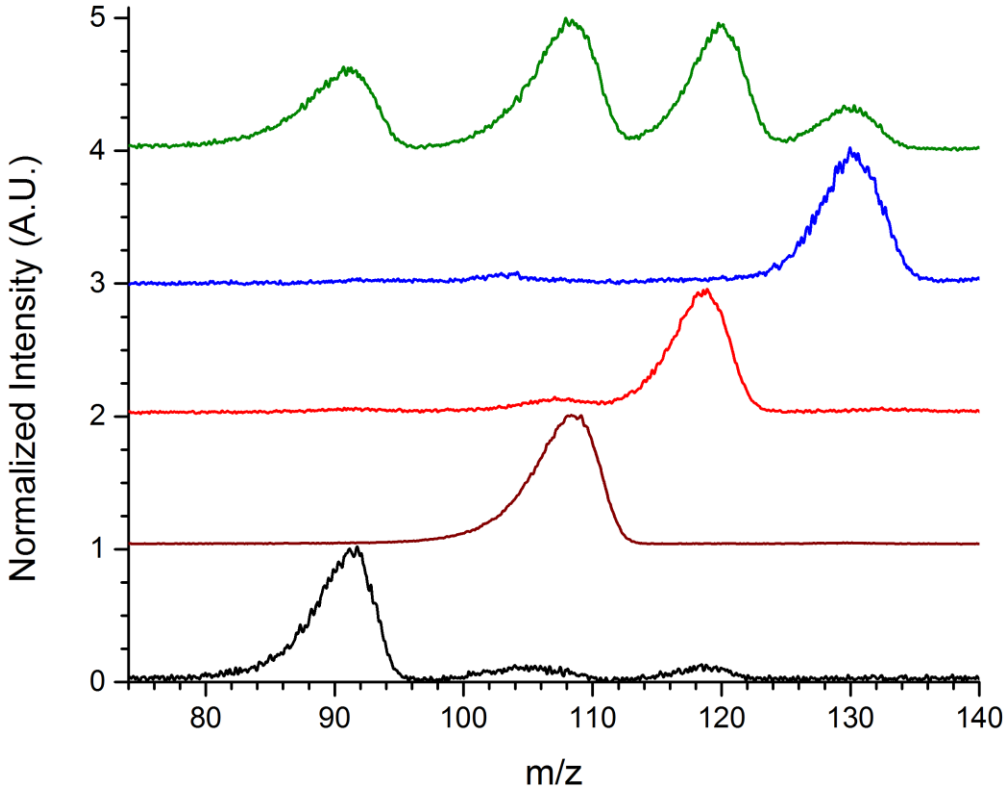

Figure 3.12: Mass spectra of a VOC mixture in 1 Torr ambient air buffer gas, Toluene (——), 2,6-Lutidine (——), N, N Dimethylaniline (——), Napthalene (——), and a mixture of all 4 components (——).

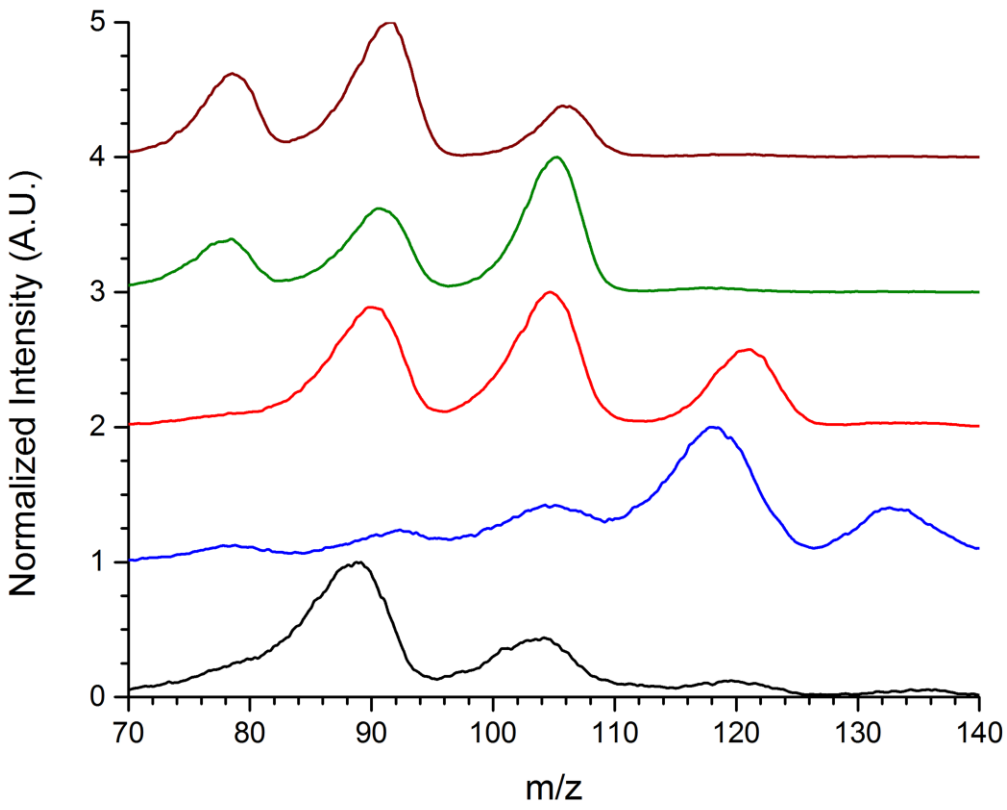

Figure 3.13: Mass spectra of VOCs sampled in 1 Torr ambient air buffer gas, Acetophenone (——), Limonene (——), Mesitylene (——), *o*-xylene (——), and *p*-xylene (——).

3.6 References

1. Savard, G.; Becker, S.; Bollen, G.; Kluge, H. J.; Moore, R. B.; Otto, T.; Schweikhard, L.; Stolzenberg, H.; Wiess, U., A new cooling technique for heavy-ions in a penning trap. *Physics Letters A* **1991,** *158* (5), 247-252.

2. Mulligan, C. C.; Talaty, N.; Cooks, R. G., Desorption electrospray ionization with a portable mass spectrometer: in situ analysis of ambient surfaces. *Chemical Communications* **2006,** (16), 1709-1711.

3. Sinha, M. P.; Gutnikov, G., Development of a miniaturized gas-chromatograph mass-spectrometer with a microbore capillary column and an array detector. *Analytical Chemistry* **1991,** *63* (18), 2012-2016.

4. Barbe, C., Masurel, D., Generators for nitrogen with membranes or conduits. *US Patent 5,383,957* **1995**.

5. Allard, J. E., Rink, L. M., Nitrogen gas generator. *US Patent 5,104,466* **1992**.

6. Su, T.; Bowers, M. T., Theory of ion-polar molecule collisions - comparison with experimental charge-transfer reactions of rare-gas ions to geometric isomers of difluorobenzene and dichloroethylene. *Journal of Chemical Physics* **1973,** *58* (7), 3027-3037.

7. Londry, F. A.; Alfred, R. L.; March, R. E., Computer simulation of single-ion trajectories in paul-type ion traps. *Journal of the American Society for Mass Spectrometry* **1993,** *4* (9), 687-705.

8. Moxom, J.; Reilly, P. T. A.; Whitten, W. B.; Ramsey, J. M., Analysis of volatile organic compounds in air with a micro ion trap mass analyzer. *Analytical Chemistry* **2003,** *75* (15), 3739-3743.

9. Sokol, E.; Edwards, K. E.; Qian, K.; Cooks, R. G., Rapid hydrocarbon analysis using a miniature rectilinear ion trap mass spectrometer. *Analyst* **2008,** *133* (8), 1064-1071.

10. Song, Q. Y.; Xu, W.; Smith, S. A.; Gao, L.; Chappell, W. J.; Cooks, R. G.; Zheng, O. Y., Ion trap mass analysis at high pressure: an experimental characterization. *Journal of Mass Spectrometry* **2010,** *45* (1), 26-34.

11. Gao, L.; Sugiarto, A.; Harper, J. D.; Cooks, R. G.; Ouyang, Z., Design and characterization of a multisource hand-held tandem mass spectrometer. *Analytical Chemistry* **2008,** *80* (19), 7198-205.

12. Goeringer, D. E.; Whitten, W. B.; Ramsey, J. M.; McLuckey, S. A.; Glish, G. L., Theory of high-resolution mass-spectrometry achieved via resonance ejection in the quadrupole ion trap. *Analytical Chemistry* **1992,** *64* (13), 1434-1439.

13. Arnold, N. S.; Hars, C.; Meuzelaar, H. L., Extended theoretical considerations for mass resolution in the resonance ejection mode of quadrupole ion trap mass spectrometry. *Journal of the American Society for Mass Spectrometry* **1994,** *5* (7), 676-88.

14. Bartelt-Hunt, S. L.; Knappe, D. R. U.; Barlaz, M. A., A review of chemical warfare agent simulants for the study of environmental behavior. *Critical Reviews in Environmental Science and Technology* **2008,** *38* (2), 112-136.

15. Xu, W.; Song, Q. Y.; Smith, S. A.; Chappell, W. J.; Ouyang, Z., Ion trap mass analysis at high pressure: A theoretical view. *Journal of the American Society for Mass Spectrometry* **2009,** *20* (11), 2144-2153.

16. Hoffmann, V.; Kasik, M.; Robinson, P. K.; Venzago, C., Glow discharge mass spectrometry. *Analytical and Bioanalytical Chemistry* **2005,** *381* (1), 173-88.

17. Robinson, K.; Hall, E. F. H., Glow-discharge mass-spectrometry for nuclear-materials. *Journal of Metals* **1987,** *39* (4), 14-16.

18. Mcluckey, S. A.; Glish, G. L.; Asano, K. G.; Grant, B. C., Atmospheric sampling glow-discharge ionization source for the determination of trace organic-compounds in ambient air. *Analytical Chemistry* **1988,** *60* (20), 2220-2227.

19. Gordon, S. M.; Callahan, P. J.; Kenny, D. V.; Pleil, J. D., Direct sampling and analysis of volatile organic compounds in air by membrane introduction and glow discharge ion trap mass spectrometry with filtered noise fields. *Rapid Communications in Mass Spectrometry* **1996,** *10* (9), 1038-1046.

20. Gao, L.; Song, Q. Y.; Noll, R. J.; Duncan, J.; Cooks, R. G.; Zheng, O. Y., Glow discharge electron impact ionization source for miniature mass spectrometers. *Journal of Mass Spectrometry* **2007,** *42* (5), 675-680

21. Smith, J. N.; Noll, R. J.; Cooks, R. G., Facility monitoring of chemical warfare agent simulants in air using an automated, field-deployable, miniature mass spectrometer. *Rapid Communications in Mass Spectrometry* **2011,** *25* (10), 1437-1444.

22. Smith, J. N.; Keil, A.; Likens, J.; Noll, R. J.; Cooks, R. G., Facility monitoring of toxic industrial compounds in air using an automated, fieldable, miniature mass spectrometer. *Analyst* **2010,** *135* (5), 994-1003.

23. Paschen, F., Ueber die zum funkenübergang inluft, wasserstoff und kohlensäure bei verschiedenen drucken erforderliche potentialdifferenz. *Annals of Physics* **1889,** *273* (5), 69-96.

24. Sismanoglu, B. N. A., J., Microhollow cathode discharge and breakdown in micron separation. *European Physical Journal of Applied Physics* **2008,** *41*, 165-172.

25. Carazzetti, P. R., Ph., Shea, H. R, Experimental study of electrical breakdown in MEMS devices with micrometer scale gaps. *Proceedings of SPIE* **2008,** *6884*, 688404-1-688404-11.

26. Andrade, F. J.; Wetzel, W. C.; Chan, G. C. Y.; Webb, M. R.; Gamez, G.; Ray, S. J.; Hieftje, G. M., A new, versatile, direct-current helium atmospheric-pressure glow discharge. *Journal of Analytical Atomic Spectrometry* **2006,** *21* (11), 1175-1184.

27. Louris, J. N.; Cooks, R. G.; Syka, J. E. P.; Kelley, P. E.; Stafford, G. C.; Todd, J. F. J., Instrumentation, applications, and energy deposition in quadrupole ion-trap tandem mass-spectrometry. *Analytical Chemistry* **1987,** *59* (13), 1677-1685.

28. Whitten, W. B.; Reilly, P. T. A.; Ramsey, J. M., High-pressure ion trap mass spectrometry. *Rapid Communications in Mass Spectrometry* **2004,** *18* (15), 1749-1752.

29. Gardner, W. P.; Shaffer, R. E.; Girard, J. E.; Callahan, J. H., Application of quantitative chemometric analysis techniques to direct sampling mass spectrometry. *Analytical Chemistry* **2001,** *73* (3), 596-605.

30. Dehmelt, H. G., Radiofrequency spectroscopy of stored ions I: storage. *Advances in Atomic and Molecular Physics* **1967,** *3*, 53-72.

31. Major, F. G.; Dehmelt, H. G., Exchange-collision technique for Rf spectroscopy of stored ions. *Physical Review* **1968,** *170* (1), 91-107.

32. Wu, G. X.; Cooks, R. G.; Ouyang, Z., Geometry optimization for the cylindrical ion trap: field calculations, simulations and experiments. *International Journal of Mass Spectrometry* **2005,** *241* (2-3), 119-132.

33. Moxom, J.; Reilly, P. T. A.; Whitten, W. B.; Ramsey, J. M., Double resonance ejection in a micro ion trap mass spectrometer. *Rapid Communications in Mass Spectrometry* **2002,** *16* (8), 755-760.

34. Wang, Y.; Franzen, J.; Wanczek, K. P., The nonlinear resonance ion trap .2. A general theoretical-analysis. *International Journal of Mass Spectrometry and Ion Processes* **1993,** *124* (2), 125-144.

35. Knight, A. K.; Sperline, R. P.; Hieftje, G. M.; Young, E.; Barinaga, C. J.; Koppenaal, D. W.; Denton, M. B., The development of a micro-Faraday array for ion detection. *International Journal of Mass Spectrometry* **2002,** *215* (1-3), 131-139.

36. Darling, R. B.; Scheidemann, A. A.; Bhat, K. N.; Chen, T. C., Micromachined Faraday cup array using deep reactive ion etching. *Sensors and Actuators a-Physical* **2002,** *95* (2-3), 84-93.

37. Scheidemann, A. A.; Darling, R. B.; Schumacher, F. J.; Isakharov, A., Faraday cup detector array with electronic multiplexing for multichannel mass spectrometry. *Journal of Vacuum Science & Technology a-Vacuum Surfaces and Films* **2002,** *20* (3), 597-604.

38. Stafford, G. C.; Kelley, P. E.; Syka, J. E. P.; Reynolds, W. E.; Todd, J. F. J., Recent improvements in and analytical applications of advanced ion trap technology. *International Journal of Mass Spectrometry and Ion Processes* **1984,** *60* (Sep), 85-98.

CHAPTER 4. HIGH RF DRIVE FREQUENCY TRAP OPERATION FOR IMPROVED MASS RESOLUTION

4.1 Introduction

With the goal of developing handheld mass spectrometry, HPMS was demonstrated at pressures where the turbopump is no longer required and with air as the buffer gas, thereby significantly reducing instrumental SWaP. A glow discharge ionization source compatible with high pressures of nitrogen and air was successfully coupled to a 500 μm CIT further improving SWaP. While high pressure mass spectra were acquired, significantly broader peaks due to increased collisional effects are the tradeoff for eliminating the turbopump. In comparison, peak widths were above 5 Da for nitrogen and air buffer gases while near unit mass resolution was seen in helium.

Since the primary goal of a handheld MS system is detection and not discovery, the wider peak widths observed with nitrogen and air are not a deterrent for potential field use, as sufficient chemical information remains for detection purposes. However, to realize the full potential of HPMS with ambient air as the buffer gas, achieving unit mass resolution would expand the capability of the technique beyond field use and because no turbopump is required, reduced instrumental costs are possible. Unit mass resolution would help in effectively determining nominal mass, isotope ratios, and in differentiation between molecules with similar fragmentation patterns.[1-3] Improved mass resolution also improves the efficiency of tandem mass spectrometry, further improving identification capabilities.[4] Some applications that would benefit from better HPMS resolution include identification of

biological molecules and environmental contaminants, where more chemical structural similarities between analytes are expected than with safety and security applications.

Recalling Equation 1.6, peaks widths are directly related to the operating pressure and inversely related to the RF drive frequency. Therefore, in order to improve peak widths under air operation, the RF drive frequency needs to be increased. However, as shown in Equation 1.5 and reproduced here as Equation 4.1:

$$\frac{m}{e} = \frac{8V}{q_z(r_o^2 + 2z_o^2)\Omega^2} \tag{4.1}$$

the mass range (m/e) scales inversely with the RF frequency (Ω) squared, reducing the span mass range where chemical structural information can be acquired. This loss in mass range can be regained by miniaturizing the ion trap dimensions (r_o and z_o).[5-7]

While most ion trap miniaturization efforts have used 1 MHz RF frequency, higher RF frequencies are needed to offset mass resolution losses at high pressures (Equation 1.6), which relates to the number of ion-neutral collisions a trapped ion experiences per RF cycle.[5-9] In- house RF amplifiers were developed to achieve amplitude modulated RF voltage scans reaching up to 1.5 kV (p-p) at 60 MHz. The amplifiers were designed to operate over the 6 to 60 MHz range with minimal changes to the experimental setup. While the ultimate goal is miniature RF sources, benchtop RF sources were used to develop the ion traps and their operation. Both miniature and benchtop RF generators require power optimization to reach the target voltages. The RF power scales as the RF frequency squared, the RF voltage squared, and the ion trap capacitance squared.[10] First focusing on RF frequency, an HPMS operating at 10 MHz would have expected power requirements two orders of magnitude higher than 1 MHz operation. Since the mass resolution for an ion trap

is dependent on RF frequency, this increased power draw can only be offset by optimizing other parameters such as capacitance or RF amplifier efficiency.

RF trapping voltages are also important to power consumption. Referring to Equation 4.1, the voltage (V) required to mass analyze a single m/e ratio scales inversely with the RF drive frequency squared.[10] As with the RF drive frequency, miniaturizing the ion traps will lower RF voltage requirements, albeit at a tradeoff of lower well depth and loss in sensitivity (Equation 1.7). Another limitation for these traps operated at high voltages is susceptibility to electrical breakdown and field emission with microscale critical dimensions.[5, 11]

Reducing capacitance from the ion trap is another strategy that can contribute toward lowering RF power requirements. For planar ion trap electrodes, capacitance scales inversely with z_o.[12-14] To compensate for higher capacitance resulting from lower electrode spacing, the surface area of the ion trap can be minimized. The capacitance of the entire ion trap electrical circuit can also be reduced through a careful layout of electrical components that minimizes path lengths.[15-17] Fabrication of miniature ion trap chambers, utilizing RF components that lower electrical path lengths in conjunction with increasing high RF drive frequencies are necessary for HPMS system configuration. Designing the ion trap and supporting electronics to minimize capacitance can significantly decrease power and make miniaturized RF generators that operate within SWaP restrictions possible. The tradeoff to lower capacitance is the requirement for larger inductance (L) to maintain the resonant frequency. However, there has been significant progress towards miniaturized inductors in the 10 to 100 MHz range with high efficiency, so this is easier to address than high capacitance.[18]

To investigate the effects of RF drive frequencies, the first experiments focused on increasing the RF frequency with 500 µm CITs in low pressures of helium buffer gas as proof of concept experiments. The helium pressure was then increased up to 1.0 Torr to characterize peak widths as a function of RF frequency and pressure. Experiments with 1.0 Torr of ambient air started with the 500 µm CIT, but smaller CITs (100 µm to 500 µm) were used to investigate higher RF frequencies while maintaining mass range and limiting ejection voltages (voltages at which ions are ejected from the ion trap during the RF ramp) below 1300 V (p-p). Single SLITs and 7-element CIT arrays were used to improve signal strength and determine if RF frequency affects mass resolution. The RF source used four different air core inductors to create resonant circuits at the RF frequencies tested. To minimize capacitance and improve power draw, all cabling was eliminated after the RF power amplifier, and a miniaturized vacuum chamber was used. The miniaturized vacuum chamber eliminated cabling previously used to make electrical connections in vacuum.[19]

4.2 Proof of Concept Experiments

Although the ultimate goal is to operate the microscale ion traps with ambient air, initial proof of concept studies of RF frequency scaling were performed in helium. Helium offered several advantages including less risk of electrical breakdown at high pressures and voltages, and a lower low mass cutoff (LMCO). High frequency experiments with helium were used to demonstrate improved mass resolution while simultaneously providing a testbed for developing solutions to electrical breakdown.

4.2.1 Low Pressure Helium

Hexane was the first molecule studied and was chosen for its strong low mass peaks from 30 to 60 Da that require only modest RF voltages to detect at elevated RF frequencies. Figure 4.1 shows mass spectra of hexane as a function of RF drive frequency from 8.20 MHz to 18.5 MHz at 20 mTorr of helium buffer gas with a 500 µm CIT. For the spectra at 8.20 MHz and 10.6 MHz, fragment peaks are seen at 55 Da, 56 Da, and 57 Da ($C_4H_9^+$). No lower mass ions beyond these were detected until the RF drive frequency was increased to 13.0 MHz, where peaks appeared between 39 Da through 43 Da ($C_3H_7^+$). At 18.5 MHz, additional peaks appeared between 30 Da through 32 Da ($C_2H_8^+$) in addition to the 39 Da through 43 Da peaks.

Several trends are seen as the RF drive frequency is increased. First, peak widths narrow with increasing RF frequency. Average peak widths (55 Da, 56 Da, and 57 Da) decreased from 0.68 Da at 8.20 MHz to 0.41 Da at 10.6 MHz, a 49% decrease. From 13.0 MHz to 18.5 MHz average peak widths (55 Da, 56 Da, and 57 Da) further decreased from 0.22 Da to 0.18 Da, a 20% decrease. A quantitative study of peak widths over the RF drive frequency range was not undertaken since peak widths should decrease with increasing atomic mass due to diminished scattering from buffer gas molecules, and a common peak was not detected across the frequency range.[20]

A second experimental trend was that as the RF drive frequency increased, the LMCO decreased. Since the LMCO scales inversely with the RF drive frequency squared, this trend was expected.[21] At 8.20 MHz the 55 Da peak was only observed near the beginning of the ramp. Better signal intensity for the 57 Da through 59 Da peaks as well as

lower mass peaks at 50 Da and 53 Da were observed when the RF Frequency was increased to 10.6 MHz. While the mass range covered 34 Da to 70 Da for 13.0 MHz, the peaks at 57 Da through 59 Da were not observed, which is an effect of a low well depth for the higher mass ions.[22-23] The LMCO advantage of a strong potential well depth was clear at 18.5 MHz since peaks down to 30 Da were detected, a 59% improvement in LMCO for a 77 % increase in RF Frequency. Electrical breakdown and RF voltage requirements beyond current RF amplifier capabilities limited the mass range. However, peak widths and LMCO improved with higher RF frequencies as predicted.

High RF frequencies exceeding 10 MHz, an order of magnitude above 1 MHz commercial instruments, were also used to detect larger ions at low pressures of helium. Figure 4.2 shows mass spectra of toluene at a RF drive frequency of 13.1 MHz at 20 mTorr of helium buffer gas with a 500 μm CIT. Two characteristic peaks for toluene were observed at 92 Da (molecular ion) and 91 Da (loss of hydrogen). Peak widths for both are below 0.1 Da. A concern for miniaturizing ion traps are higher order fields associated with simplified geometries that could have detrimental effects on mass resolution.[24-26] These narrow peak widths suggest this was not the case with the additional factor that dimensional tolerances for trap fabrication exceed requirements for unit mass resolution.

For perspective, these peak widths compare favorably with some early commercial instrumentation. The initial Finnigan MAT ion trap instrument had peak widths near 0.5 Da, while MS instruments into the mid 1990s were limited to peak widths near 0.2 Da.[10] The Finnigan used a scan rate of 5,555 $Da \cdot sec^{-1}$, compared to 6,800 $Da \cdot sec^{-1}$ used here or 20 % slower. The faster scan rate improves signal strength while still maintaining high mass resolution. While current commercial ion traps have demonstrated peak widths near 10^{-5} Da,

this has been achieved by significantly decreasing the scan rate which increases the analysis time and lowers throughput.[27] For a field portable MS used in applications where analysis time is critical, operating at high scan rates that just achieve resolution needed for detection is a tradeoff that is made.

4.2.2 High Pressure Helium

To study the effects that helium pressure and RF drive frequency have on mass resolution, triethyl phosphate (TEP), a chemical warfare agent simulant for nerve agents tabun, sarin, and soman was chosen.[28] Figure 4.3 shows the mass spectra for TEP at a RF drive frequency of 17.2 MHz with increasing helium pressure from 41 mTorr to 1.0 Torr with a 500 µm CIT. Fragment peaks were seen at 43 Da ($C_3H_7^+$), 44 Da, and 45 Da for each pressure. As previously observed, signal intensity decreased as pressures increased, attributed to cooling of the tungsten filament.

TEP peak widths were analyzed as a function of pressure for three different RF drive frequencies (10.1 MHz, 13.6 MHz, and 17.2 MHz) and shown in Figure 4.4. Near 200 mTorr the average peak widths were 0.35 Da at 10.1 MHz (56 Da, 57 Da, 58 Da), 0.22 Da at 13.6 MHz (43 Da, 44 Da, 45 Da), and 0.18 Da at 17.2 MHz (43 Da, 44 Da, 45 Da). When the pressure was increased above 1.0 Torr, peak widths increased as expected. With 10.1 MHz, the average peak width increased 81% from 0.35 Da to 0.83 Da. For 13.57 MHz, average peak width increased by 86 % from 0.22 Da to 0.55 Da. Finally, at 17.2 MHz the average peak width increased from 0.18 Da to 0.40 Da, a 76% change. At 1 Torr the peak widths were 0.83 Da (10.1 MHz), 0.55 Da (13.6 MHz), and 0.40 Da (17.2 MHz). Increasing the RF frequency (1.0 Torr helium) by 3.5 MHz improved peak widths by 33%, while the

difference between peak widths at 10.1 MHz and 17.2 MHz was 70%. With the elevated RF drive frequencies above 10 MHz, sub-unit mass resolution was observed across the frequency range at 1 Torr of helium. When the RF drive frequency was at 13.6 MHz and above, mass resolution was below 0.6 Da, or comparable to commercial ion trap instruments.[10]

4.3 High RF Frequency Operation with Air Buffer Gas

While unit resolution at 1 Torr of helium buffer gas was accomplished with a 500 µm CIT, the larger peak widths detected with air buffer gas (Figure 3.9) will require significant scaling of the RF frequency to reach unit mass resolution. To minimize the risk of electrical discharge and to prevent instrumental damage, a 1300 V (p-p) maximum ejection voltage was empirically determined to be a reasonable high voltage limit. To operate within these voltage limitations, smaller CITs will be used to decrease the RF voltage requirements by r_o^2. Through proportional scaling of RF frequency and ion trap size, voltages that fall within the operating limits are possible.

4.3.1 Miniaturization of CITs

Four CITs were fabricated with r_o values of 350 µm, 225 µm, 165 µm, and 100 µm. Table 4.1 lists the critical dimensions of each trap. The z_o/r_o ratio were slightly different for each CIT ranging from 1.15 for the r_o = 100 µm CIT to 1.40 for the r_o = 225 µm CIT. These geometries were chosen to accommodate commercially available sheet metal and insulating spacer materials used to fabricate the traps. As seen in our early HPMS experiments with helium (Figures 2.6 and 2.8), these slight changes in the z_o/r_o ratio should not affect CIT performance at pressures above 200 mTorr of helium where collisional frequency determines

peak width.[20, 29] The endcap aperture was also only partially scaled relative to the largest CIT. The r_o = 500 µm CIT endcap hole size to r_o size ratio was 0.8. If this ratio was maintained for the r_o = 100 µm, the endcap hole size would be 80 µm, below practical limits for wet etching of sufficiently rigid sheet metal for endcap electrodes. The larger CIT's endcap hole size does not appear to affect mass resolution under high pressure conditions.

The first set of experiments focused on determining the RF drive voltage or ejection voltages that were possible for different CIT sizes and RF drive frequencies. Ejection voltages were characterized for *p*-xylene over the 6.14 to 59.44 MHz RF drive frequency range. There were three *p*-xylene peaks located at 77 Da, 91 Da, and 106 Da. Figure 4.5 shows the ejection voltages for the 106 Da peak as a function of RF drive frequency for the different CITs. The 106 Da peak was chosen over the more abundant 91 Da peak due to variations in fragmentation ratios between 91 Da and 92 Da as a function of RF drive frequency and pressure. Each ejection voltage was measured with resonance ejection using axial RF voltages and frequencies optimized for mass resolution.[30-31]

For the CITs with radii ranging from 225 µm to 500 µm, a linear relationship between RF drive frequency and ejection voltage was observed. While a quadratic relationship was expected (Equation 4.1), the linear relationship was plausible. Double resonance ejection was used for each RF frequency, and it ejects ions at lower RF voltages than Equation 4.1 predicts. The RF drive voltage was capped at less than 1300 V to minimize any electrical breakdown considerations and limit RF power requirements. For the 165 µm and 100 µm CITs, neither a quadratic or linear relationship was observed. For these CITs, the optimal axial RF conditions used lower q_z values compared to the larger CITs, changing the trend between RF drive frequency and ejection voltage by approximately 20%. The RF drive

frequency range used for the 100 µm CIT covered 40 to 60 MHz, at least a four times larger RF drive frequency range than is practical for a 500 µm CIT. The maximum RF voltages used for the 165 µm and 225 µm CITs were 900 V (p-p) since this was the maximum ejection voltage attainable for the RF amplifiers available at the time the experiments were performed.

To characterize mass resolution improvements with RF drive frequency, mass spectra of *p*-xylene were recorded as a function of RF drive frequency with the five different trap sizes at a pressure of 1.0 Torr of ambient air buffer gas. Figure 4.6 shows one representative mass spectra for each trap size covering the entire RF frequency range that was studied from 6.14 MHz to 59.44 MHz. The mass spectra were normalized for visual comparison since signal strengths varied between trap sizes. There were several factors that determined the RF frequency range studied for each trap. For the r_o = 500 µm CIT the lowest RF frequency of 6.14 MHz was chosen since this was a common RF frequency used to study this trap. The highest RF frequency of 10.64 MHz was chosen since higher RF frequencies would have risked electrical discharge. For the r_o = 350 µm, r_o = 225 µm, and r_o = 165 µm CITs the lowest RF frequency was chosen to overlap with the next largest CIT to compare mass resolution and ensure peak broadening from dimensional tolerances was not a problem. Again, the highest RF frequency was chosen based on experimental electrical breakdown limits. For the r_o = 100 µm CIT electrical breakdown was observed between 30 MHz and 40 MHz, so that RF frequency range was not investigated. Since electrical breakdown was not observed when the RF frequency reached 40 MHz, it was chosen as the lowest RF frequency for this trap. The 60 MHz cutoff was determined by the RF amplifier losing gain above 60 MHz.

There were changes in the mass spectra as a function of RF frequency. For the 500 µm CIT there are two peaks located at 106 Da (molecular ion) and 91 Da ($C_7H_7^+$) with minimal baseline resolution between them. For the four other mass spectra, a third peak appears at 77 Da ($C_6H_5^+$) as the LMCO scales inversely with the quadratic of RF drive frequency and proportionally with the pseudopotential well depth.[21] As the RF drive frequency is increased, a significant narrowing of the peak widths from the 500 µm trap (6.14 MHz RF) to the 100 µm trap (59.44 MHz RF) resulted. The improvement is such that with the 100 µm CIT, two shoulder peaks at 78 Da and 92 Da appear that are lost to peak broadening for the larger CIT.

The relationship between mass resolution and RF drive frequency is shown in Figure 4.7 where the peak widths (FWHM) are plotted as a function of the RF drive frequency. Each data point corresponds to between four and six duplicate spectra with error bars within the symbol if not otherwise seen. The conditions for double resonant ejection required precise tuning to maximize the mass resolution.[32] For these experiments, from 6 MHz to 20 MHz covering the 225 µm, 350 µm, and 500 µm trap CIT, the hexapolar resonance produced the best signal strength and mass resolution. An unexpected change in axial RF optimization was discovered for the 165 µm CIT. Above 20 MHz, the octopolar resonance had better sensitivity and mass resolution than the hexapolar resonance. Mass resolution improved by 13% when the octopolar resonance was used instead of the hexapolar resonance. From 22 MHz to 30 MHz, peak widths for both resonances are shown. For the 100 µm CIT, which was run at RF drive frequencies above 30 MHz, only the octopolar resonance was used since it gave the narrowest peak widths, although both axial RF resonances were considered over the entire RF drive frequency range.

The CIT critical dimensions (Table 5.1) including ratio of r_o to z_o and ring electrode thickness should have diminished effects on mass resolution at the high buffer gas pressures and RF drive frequencies being investigated, where peak widths are determined by the frequency of ion-neutral collisions. The general trend of improved mass resolution with increasing RF drive frequency is seen for all traps. For the individual traps, improvements of 26%, 20%, 13%, 31% and 49% were seen for the 500, 350, 225, 165, and 100 μm traps respectively. These improvements correspond to optimal mass resolutions of 4.1 Da, 3.8 Da, 3.3 Da, 1.9 Da and 0.8 Da for the individual traps. Taken as a whole, peak widths improved from 5.5 Da at 6.14 MHz to 0.8 Da at 59.44 MHz, or an 85% improvement.

While the change in resonant ejection behavior with respect to the hexapolar and octapolar resonance was unexpected, the most plausible explanation is that at the higher frequencies the ion cloud is more centrally located in the CIT and the octapolar component to the net trapping fields is stronger.[8] The ion cloud size is expected to decrease with RF frequency to the two-thirds power.[33] This results in a strong resonant ejection not seen at lower RF drive frequencies. Furthermore, since the octopolar resonance ejected ions earlier in the RF ramp, the high mass cutoff improved by 13%. The lower axial RF frequencies also scale favorably for low power RF electronics required to produce the voltages for double resonant ejection.

4.3.2 CIT Arrays and SLITs

As discussed in Chapter 1, one major limitation to reducing ion trap dimensions is sensitivity and ion storage capacity. Using an ion trap array is one way to overcome the loss in sensitivity. An ion trap array should increase integrated signal strength proportionally to

the number of array elements while maintaining mass resolution. There have been numerous examples of ion trap arrays demonstrated on the millimeter and micrometer scale.[6, 34-35] However, ion trap arrays have not been pursued under high RF drive frequencies above 10 MHz and high pressure conditions simultaneously.

To characterize the effects of an array on signal strength, a 7-element r_o = 100 μm CIT was constructed and run at 1.0 Torr of air with a RF drive frequency of 48.16 MHz. Subsequently, six out of seven array elements were masked off with copper tape, and the single ion trap signal was compared to the 7-element array trap (Figure 4.8). By masking off the trap elements, no critical dimensions or electrode alignment was changed, both significant factors that could affect the reproducibility of an ion trap. No changes in operating conditions were observed from adding conducting tape to the electrode surface. Experimental conditions that could change signal strength including gas pressure, ionization time and voltages, drive RF and axial RF voltages and frequencies were all kept constant. As expected, the signal intensity of the 7-element array was a factor of seven times that of the single CIT within experimental error.

The SLIT is another electrode design that has been introduced as a way to improve sensitivity with microscale ion traps.[36] A SLIT with x_o = 100 μm and y_o = 1.7 mm was constructed to compare to a r_o = 100 μm CIT. The RF frequency was 38 MHz while the pressure was 1.0 Torr of air. While it was possible to keep most experimental conditions constant between the CIT and CIT array, comparing two different traps required experimental changes to optimize performance. The RF was re-tuned for optimal efficiency for each ion trap. The RF voltages were chosen to maintain mass range, since the SLIT and CIT have different ejection voltages. The axial RF voltages and frequencies were optimized

for mass resolution. While ionization time was kept constant, the glow discharge ion accelerating voltage was optimized for maximum signal. Mass spectra comparing signal strength for the CIT and SLIT (Figure 4.9) showed that signal increased by a factor of 6 for the SLIT compared to the CIT with no loss in mass resolution. With both the CIT array and the SLIT, the improvement in signal strength over a single CIT was confirmed.

While the 7-element CIT arrays and SLITs improved sensitivity compared to the single CIT, loss of mass resolution from inadequate fabrication tolerances is a possibility. Peak widths were characterized for the CIT arrays and the SLITs and then compared to the single CITs. CIT array electrodes were fabricated with the same critical dimensions as the single CITs. The 7-element CIT arrays were run over a RF drive frequency range from 6.26 MHz to 50.46 MHz (Figure 4.10). Mass spectra were similar to the single CIT (Figure 4.6) as the 77 Da peak was weak at 6.26 MHz but clearly present as the RF drive frequencies increased. The peaks at 91 Da and 106 Da were also observed as with the single CIT. No fabrication tolerance problems were observed since the mass resolution for the different geometries were within experimental error.

Single SLITs were fabricated with four different sets of critical dimensions (Table 4.2) that covered the 100 µm to 500 µm dimension range. A 350 µm SLIT was not studied since the frequency range was well characterized by the 500 µm and 270 µm SLITs, and the peak widths were well-above the target values desired. Smaller SLIT aperture endcaps of 150 µm were used for each of the traps to improve differential pressure and to save on fabrication cost of one design, since no performance loss was seen for different aperture sizes in the CITs. Mass spectra for the SLITs were run from 6.86 MHz to 42.16 MHz (Figure

4.11). At 6.86 MHz the 77 Da peak was stronger compared to the CIT and CIT array, suggesting the geometry of the SLIT improved trapping of lower mass ions.[36]

Peak widths for *p*-xylene as a function of RF drive frequency at 1.0 Torr of air were compared between a single CIT, a CIT array, and a SLIT in Figure 4.12. The FWHM vs. RF frequency trends for CIT and CIT array are nearly identical. The CIT arrays were successfully scaled despite tighter dimensional requirements both from miniaturization and improved mass resolution with higher RF drive frequencies.[37] With the SLITs, peak widths were nearly identical at frequencies below 14 MHz and at frequencies above 24 MHz.

In the 14 MHz to 24 MHz range the optimal axial RF resonance for the CITs was the hexapole as opposed to the octopole for the SLITs. As previously discussed, smaller CITs operated at higher frequencies had better mass resolution when the octopole resonance was used instead of the hexapole resonance. With the SLITs, the octopole resonance was usable at 14 MHz instead of 23 MHz for the CITs. This difference in axial RF behavior between the CIT and SLIT is not well understood, but likely is due to the location of ions within the trap and their relative location to higher order field components. The SLIT feature will cause different relative field strengths compared to the cylindrical feature, so differences in axial RF behavior were not surprising.[38-39] Accessing the octopolar resonance at a lower RF drive frequency is beneficial. Peak widths below 3 Da with the SLIT trap are achieved at 18 MHz compared to 22 MHz with the CIT. This operational difference lowers the RF frequency required for sub-3 Da peak widths by 13%, improving RF voltage and power requirements for identical mass resolution.

4.3.3 Tradeoffs between Mass resolution, Pressure, and Frequency

While HPMS is defined as an operational pressure of ~1.0 Torr of ambient air as the buffer gas, some applications may introduce the flexibility to operate at lower pressures. For example, improvements in roughing pump technology may decrease SWaP demands and make lower pressure ion trap operation possible without sacrificing gas flow or analysis time.[40-41] Thus, understanding the effects of pressure at high RF drive frequencies is of interest.

Mass spectra of *p*-xylene were recorded from approximately 250 mTorr to 1.0 Torr of ambient air pressures with >30 MHz RF drive frequencies. The pressure range was chosen to accommodate the glow discharge operational pressure range, as below 250 mTorr pressure the glow discharge source is non-functional. Figure 4.13 shows representative *p*-xylene spectra taken at 59.44 MHz with a 100 µm CIT at buffer gas pressures of 1.02 Torr, 675 mTorr and 315 mTorr. The expected improvement in mass resolution as the pressure decreases is evident in the appearance of the m/z 76, 78, and 92 Da peaks as shoulders to the 77 Da and 91 Da peaks. For the 1.02 Torr spectra, the 78 and 92 Da peaks are visible but not the 76 Da peak. At 672 mTorr, the 76 Da peak appears with the 78 and 92 Da peaks readily apparent. Finally, at 313 mTorr, the 76 Da peak is resolved while the 78 and 92 Da peaks approach unit resolution. The main peaks at 77, 91 and 107 also narrow as the pressure decreases.

Peak widths for *p*-xylene were plotted as a function of ambient air pressure with RF drive frequency for 59.44 MHz (100 µm CIT), 47.24 MHz (100 µm CIT), and 30.34 MHz (165 µm CIT) (Figure 4.14). At 59.44 MHz, peak widths improved from 0.8 Da to 0.56 Da

when the ambient air pressure was dropped from 1.01 Torr to 329 mTorr. When the RF drive frequency was decreased to 47.24 MHz, the peak widths narrowed from 1.2 Da at 1.0 Torr to 0.62 Da at 300 mTorr, a 38% improvement. It is interesting to note that the peak widths for both frequencies were similar near 300 mTorr where the mass resolution was likely limited by CIT geometry instead of buffer gas pressure. When the RF frequency was further dropped to 30.34 MHz, peak widths decreased 56% from 1.8 Da at 1.0 Torr to 0.8 Da near 250 mTorr, with unit resolution possible near 300 mTorr.

Based on these results, tradeoffs between RF drive frequency, ambient air pressure, and pumping demands are apparent. If miniature pumping systems were more efficient and lower operating pressures possible, the RF drive frequency could be significantly lower while maintaining mass resolution. For example, at 1.0 Torr a RF drive frequency near 59 MHz was needed for unit mass resolution, but near 350 mTorr a RF drive frequency near 30 MHz achieved unit resolution. This lower pressure operation would improve power required to generate the lower RF drive frequency (30 MHz) by approximately a factor of 4. Alternatively, narrower peak widths would be possible with the same RF SWaP, improving the chemical characterization abilities of the instrument. Since roughing pump technology currently limits operational pressures but will likely improve with time, understanding these tradeoffs is useful for projecting future directions of HPMS.

4.4 Conclusions

Proof of concept experiments with microscale CITs (500 μm) showed mass resolutions below 0.1 Da for 20 mTorr helium, and 0.5 Da for 1 Torr of helium when increasing the RF frequency. The buffer gas was then changed to ambient air. Peak widths

improved from 5.5 Da to 0.8 Da (85%) when operated with 1.0 Torr and decreasing CIT trap size with increasing RF frequency. The microscale CITs were successfully scaled down by a factor of five while maintaining mass resolution performance with CITs operated over a RF drive frequency range from 6.14 to 59.44 MHz. To offset smaller ion capacity issues, 7-element CIT arrays, and single SLITs were fabricated with critical dimensions from 100 µm to 500 µm. The 100 µm CIT array and SLIT improved signal by factors of 7 and 6, respectively, compared to a single CIT, demonstrating that signal intensity lost to miniaturization can be regained through arrays and SLIT geometries. CIT 7-element arrays and single SLITs showed no loss in mass resolution despite tighter dimensional tolerances. Ambient air pressures down to 250 mTorr were investigated to better understand the tradeoffs between RF drive frequency and ambient air operating pressure. With current pumping technology, unit mass resolution at 1 Torr meets target specifications, while future developments in pumping technology could decrease operating pressures with no loss in gas throughput or analysis time.

4.5 Tables and Figures

r_o (μm)	z_o (μm)	Insulator Thickness z_o (μm)	Ring Electrode Thickness z_o (μm)	Endcap Hole Diameter z_o (μm)
500	645	250	790	400
350	455	200	510	200
225	315	125	380	200
165	200	75	255	200
100	115	50	130	165

Table 4.1 Critical dimensions for the CITs used to investigate high RF drive frequencies.

x_o (μm)	z_o (μm)	Insulator Thickness z_o (μm)	Ring Electrode Thickness z_o (μm)	Endcap Hole Diameter z_o (μm)
500	645	250	790	135
270	315	125	380	135
170	200	75	255	135
100	115	50	130	135

Table 4.2 Critical dimensions for the SLITs used to investigate high RF drive frequencies.

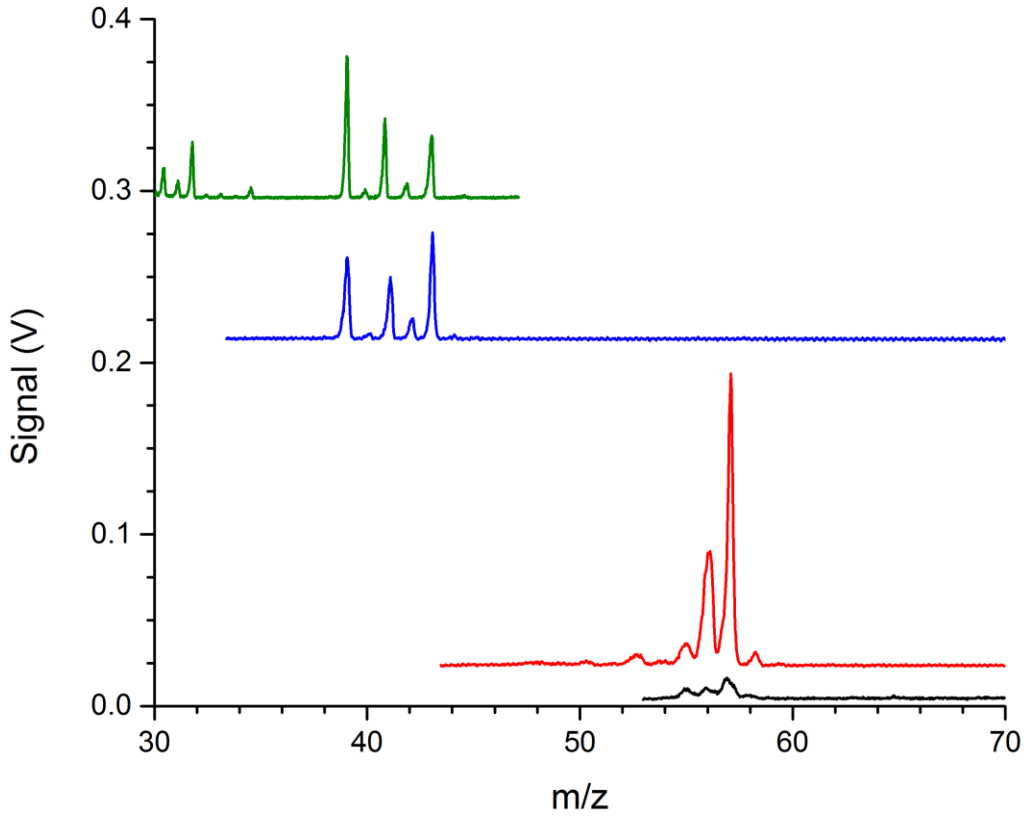

Figure 4.1: Mass spectra of hexane in 20 mTorr of helium buffer gas with increasing RF drive frequency at 8.20 MHz (——), 10.6 MHz (——), 13.0 MHz (——), and 18.5 MHz (——). Peak width and LMCO scale inversely with RF drive frequency.

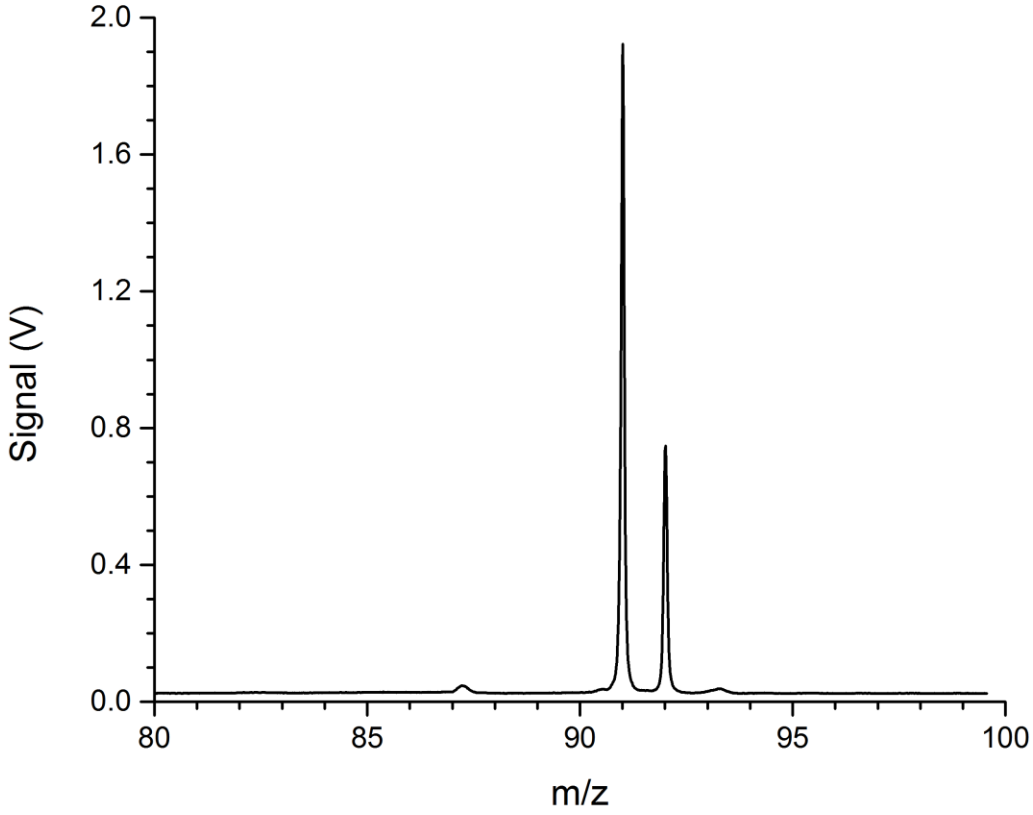

Figure 4.2: Mass spectra of Toluene taken at 20 mTorr helium and a RF drive frequency of 13.1 MHz. The molecular ion (92 Da) and fragment peak from the loss of hydrogen (91 Da) have peak widths below 0.1 Da.

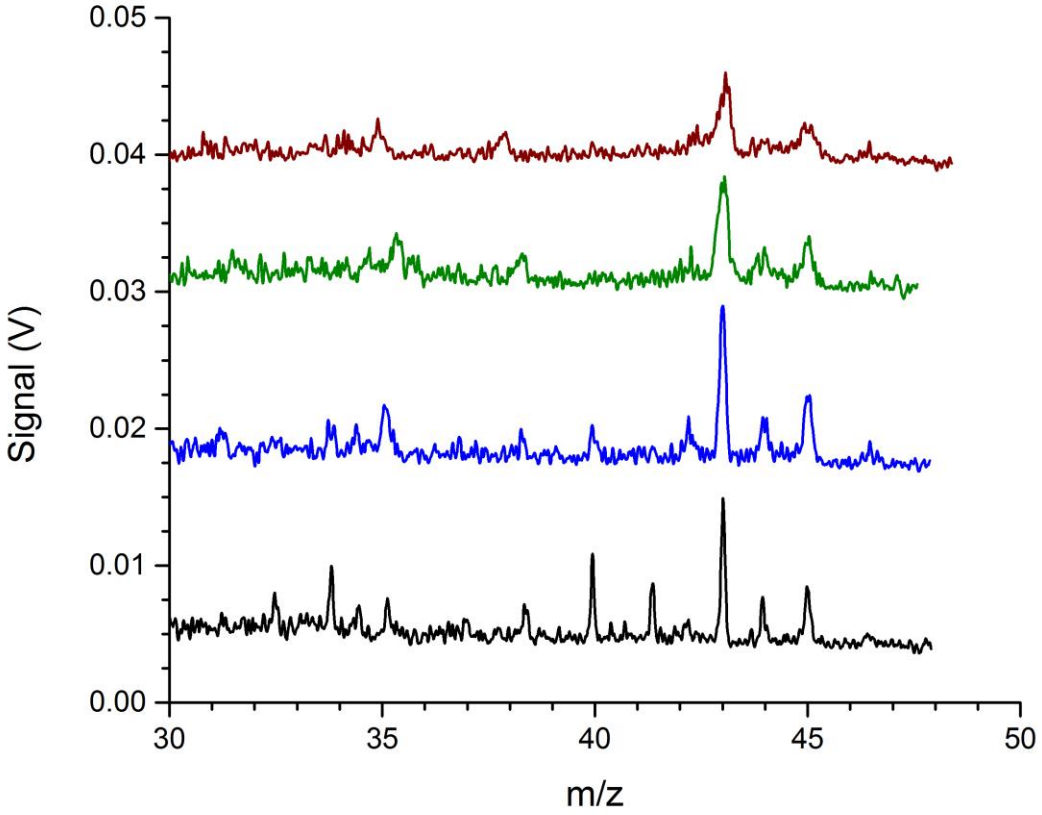

Figure 4.3: Mass spectra of TEP with increasing helium buffer gas pressure for 41 mTorr (——), 260 mTorr (——), 530 mTorr (——), and 1.0 Torr (——).

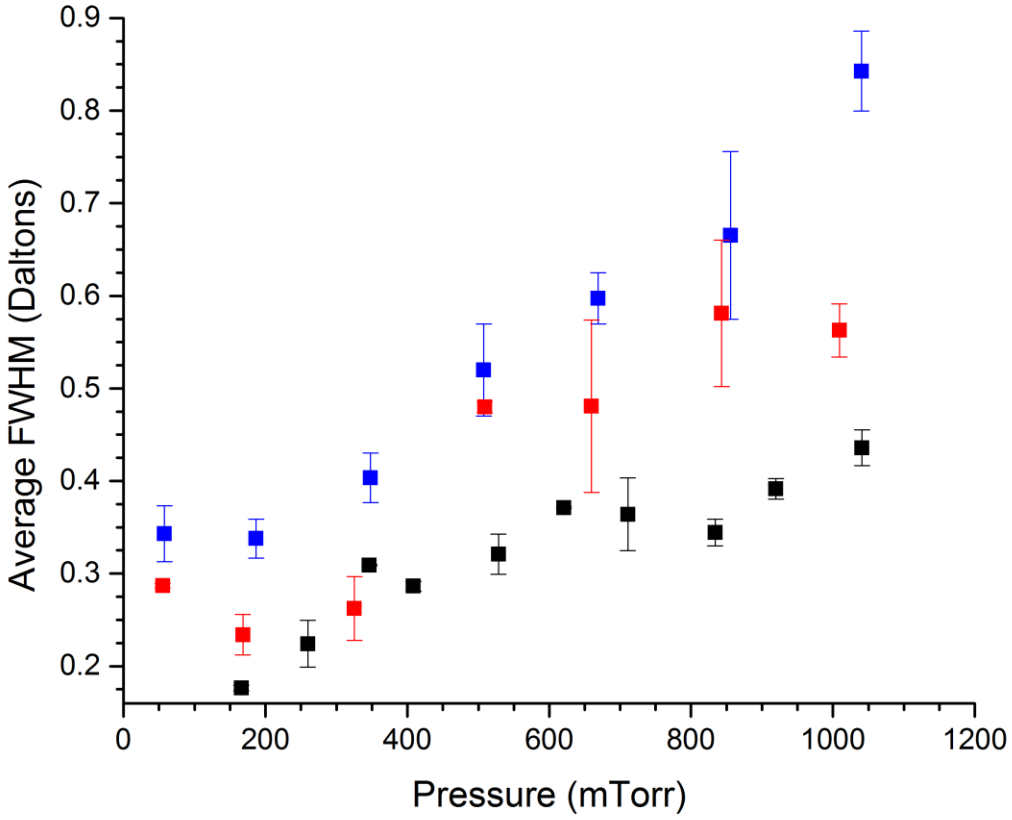

Figure 4.4: Average peak widths for TEP as a function of helium buffer gas pressure at 10.1 MHz (■), 13.6 MHz (■), and 17.2 MHz (■).

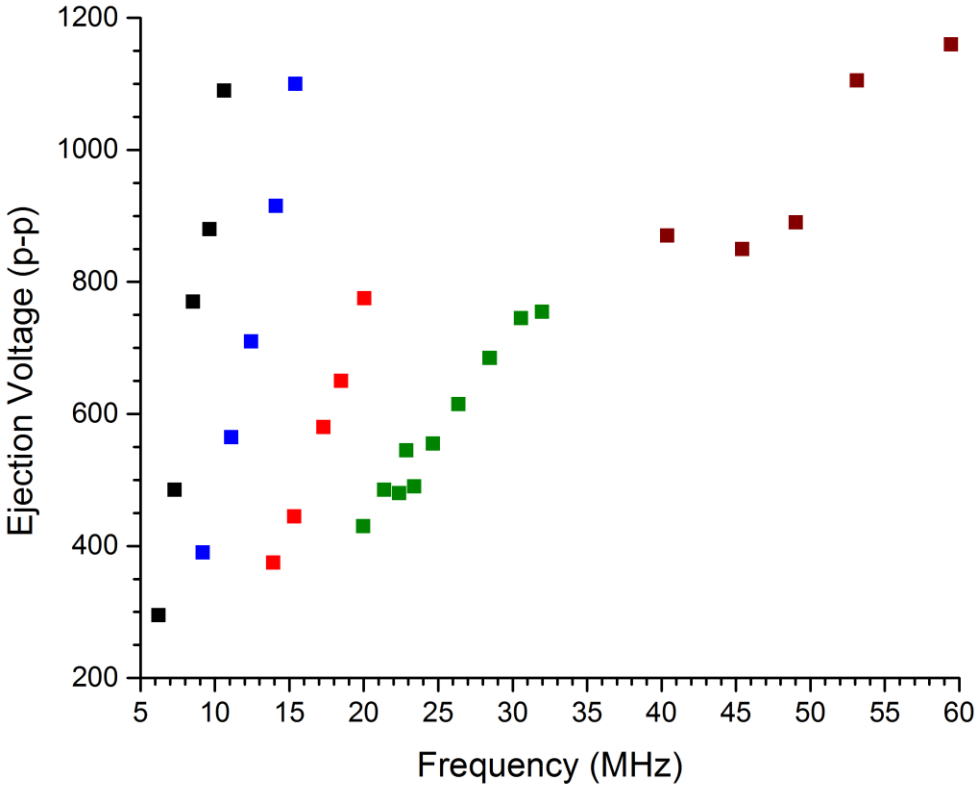

Figure 4.5: Ejection voltages for *p*-xylene 106 Da as a function of RF drive frequency with CIT radii of 500 µm (■), 350 µm (■), 225 µm (■), 165µm (■), and 100 µm (■). RF drive frequencies and CIT dimensions were chosen to maintain RF voltages below 1300 V (p-p).

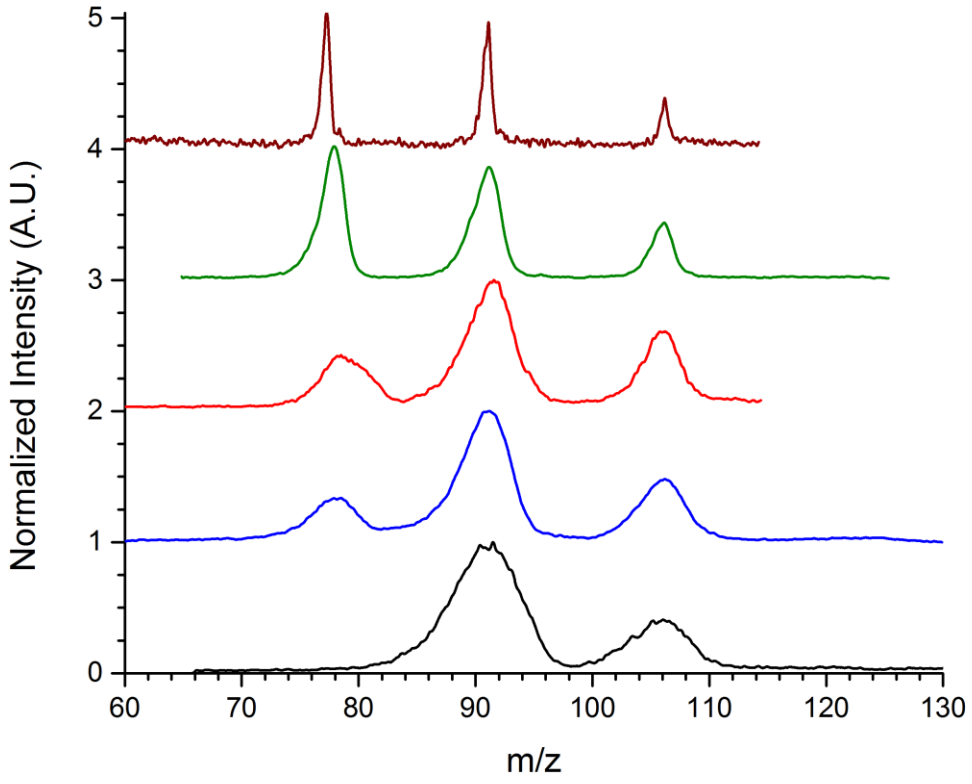

Figure 4.6: Mass spectra of *p*-xylene with increasing RF drive frequency and decreasing CIT radius for 6.14 MHz, r_o=500 µm (——), 12.43 MHz, r_o=350 µm (——), 20.10 MHz, r_o=225 µm (——), 28.46 MHz, r_o=165 µm (——), and 59.44 MHz, r_o=100 µm (——).

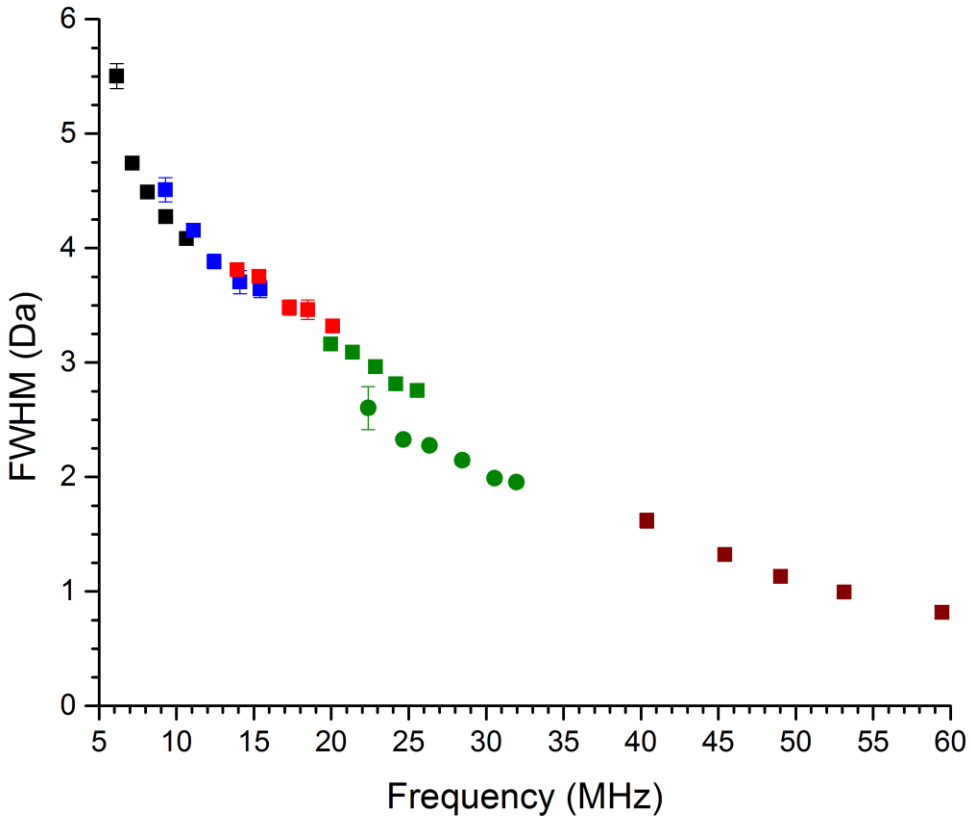

Figure 4.7: Peak widths for *p*-xylene 106 Da as a function of RF drive frequency with CIT radii of 500 µm (■), 350 µm (■), 225 µm (■), 165µm hexapole resonance (■),165µm octopole resonance (●), and 100 µm (■). Peak widths with sub-unit mass resolution are reached at RF drive frequencies above 50 MHz.

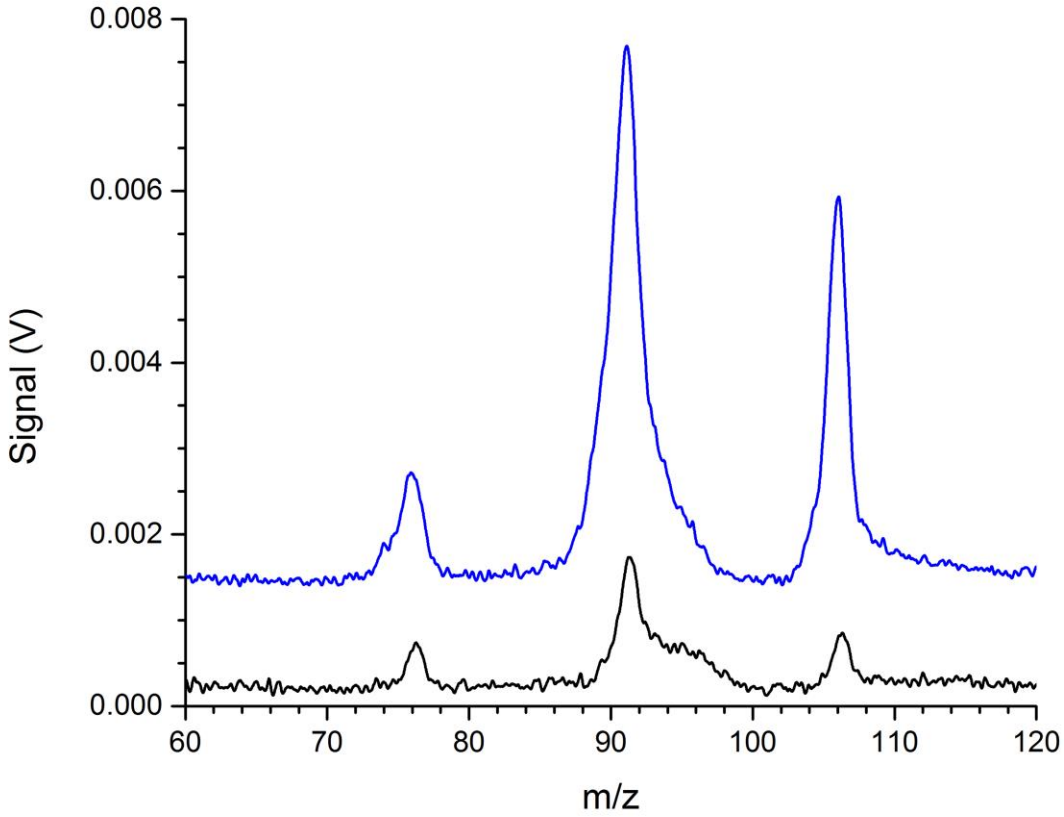

Figure 4.8: Mass spectra of *p*-xylene in 1.0 Torr of ambient buffer gas for a single CIT (——) and a 7-element array (——) showing a factor of 7 increase in signal for the array compared to the single element CIT.

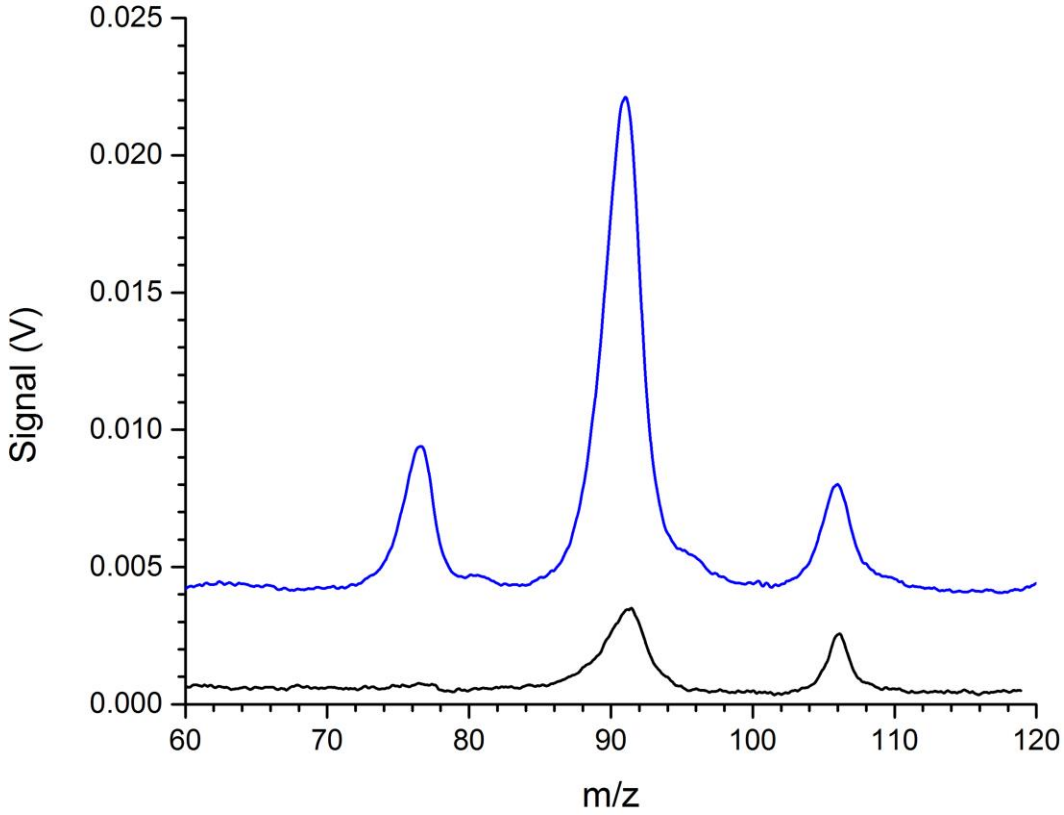

Figure 4.9: Mass spectra of *p*-xylene in 1.0 Torr of ambient buffer gas for a single CIT (——) and a SLIT (——) showing a factor of 6 increase in signal for the SLIT compared to the single element CIT.

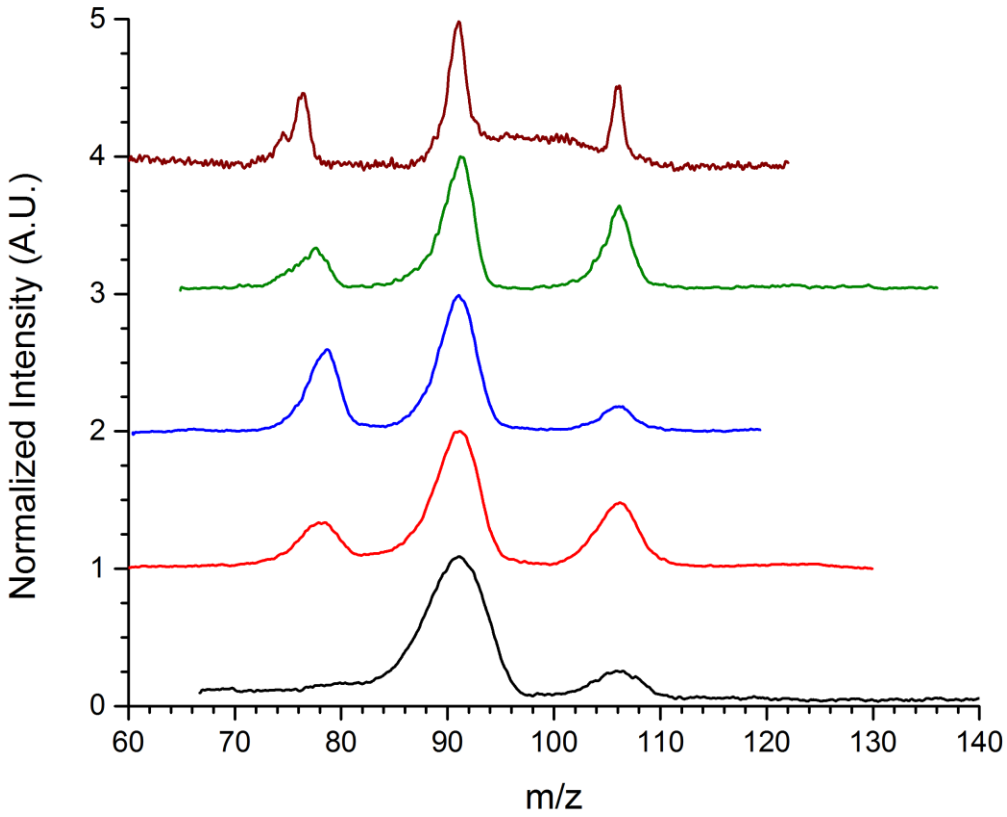

Figure 4.10: Mass spectra of *p*-xylene taken with 7-element CIT arrays with increasing RF drive frequency and decreasing CIT radius for 6.26 MHz, r_o=500 µm (——), 11.93 MHz, r_o=350 µm (——), 20.57 MHz, r_o=225 µm (——), 25.09 MHz, r_o=165 µm (——), and 50.46 MHz, r_o=100 µm (——).

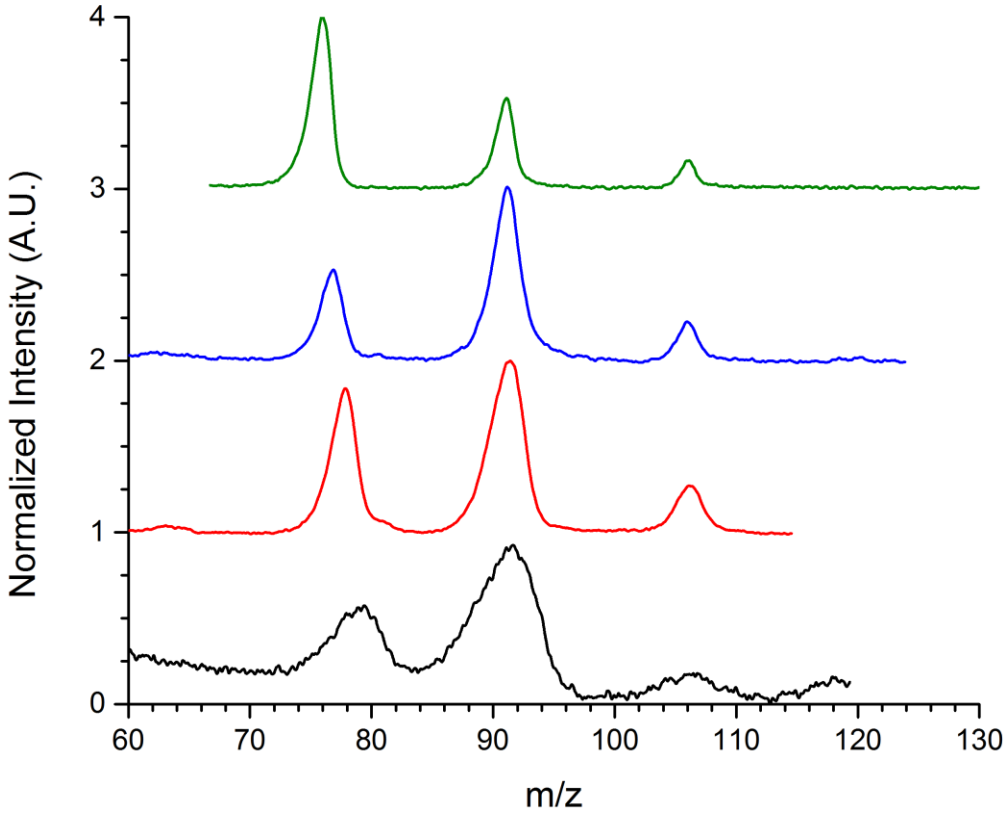

Figure 4.11: Mass spectra of *p*-xylene taken with a SLIT with increasing RF drive frequency and decreasing CIT radius for 6.86 MHz, r_o=500 µm (——), 23.46 MHz, r_o=270 µm (——), 29.36 MHz, r_o=170 µm (——), 42.16 MHz, r_o=100 µm (——).

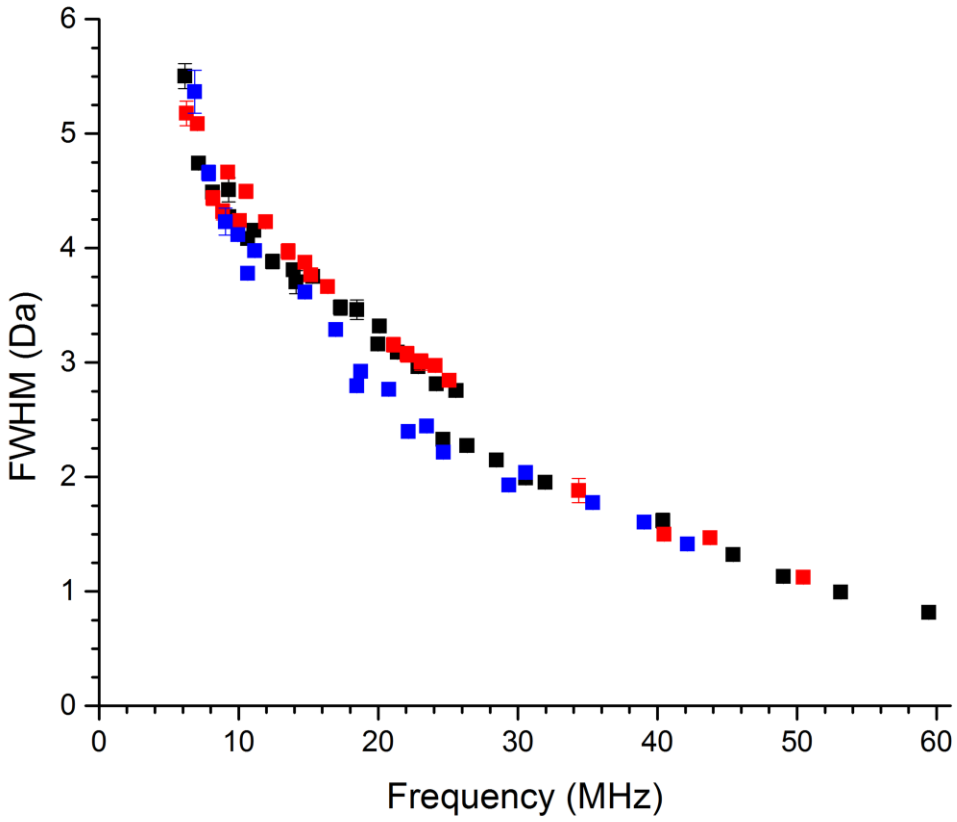

Figure 4.12: Peak widths for *p*-xylene 106 Da as a function of RF drive frequency for single CITs (■), single SLITs (■), and 7-element CITs (■). With the need to improve sensitivity of microscale ion traps, the capability of operating CIT arrays and SLITs without loss in mass resolution is critical.

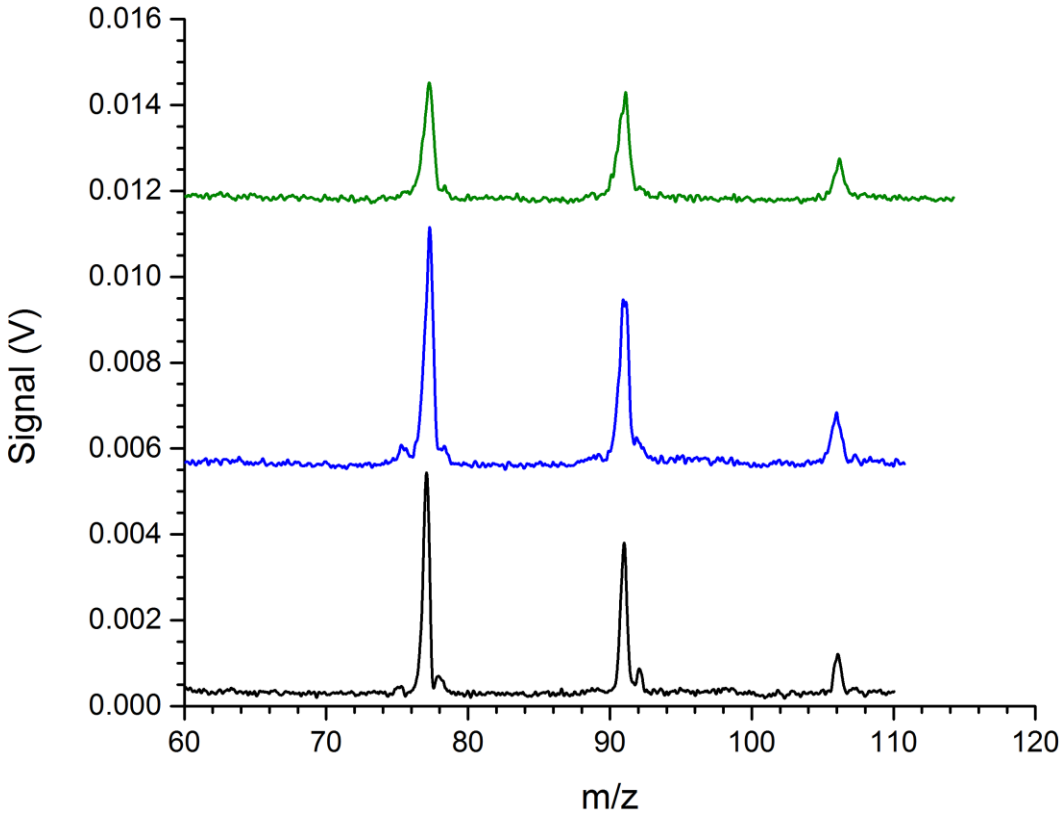

Figure 4.13: Mass spectra of *p*-xylene at a RF drive frequency of 59.44 MHz with ambient air pressures of 313 mTorr (——), 672 mTorr (——), and 1.02 Torr (——).

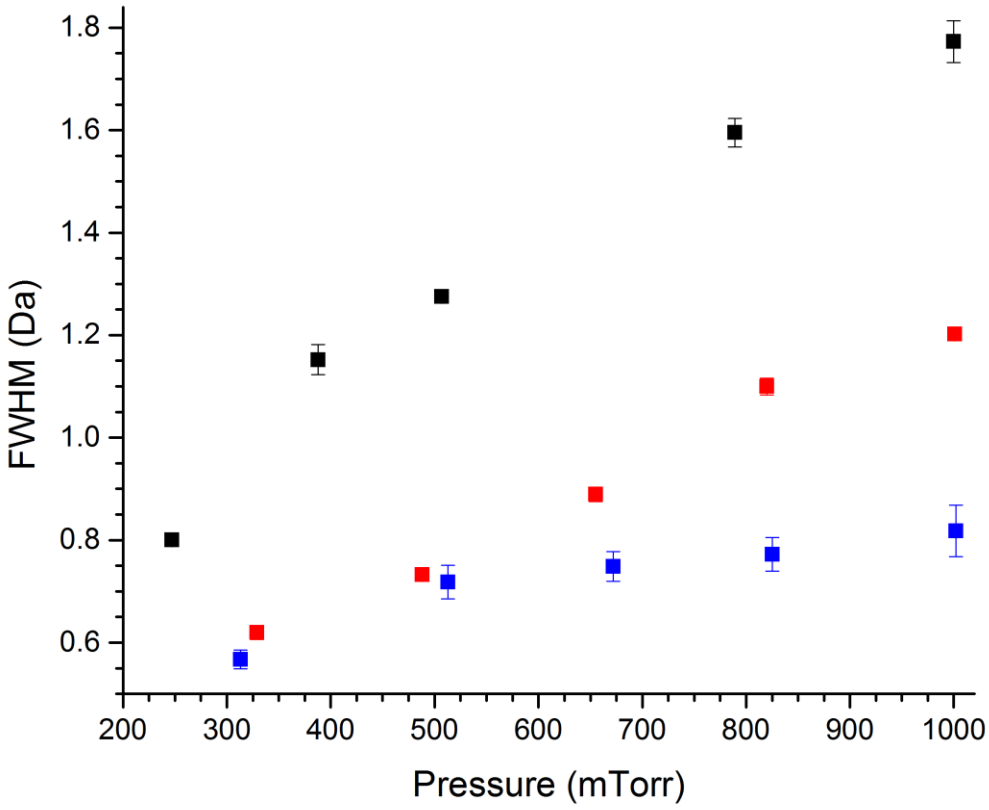

Figure 4.14: Peak widths for *p*-xylene 106 Da with increasing of ambient air pressure for 30.34 MHz, r_o=165 µm (■), 47.24 MHz, r_o=100 µm (■), and 59.44 MHz, r_o=100 µm (■).

4.6 References

1. Heumann, K. G.; Gallus, S. M.; Radlinger, G.; Vogl, J., Precision and accuracy in isotope ratio measurements by plasma source mass spectrometry. *Journal of Analytical Atomic Spectrometry* **1998,** *13* (9), 1001-1008.

2. Muccio, Z.; Jackson, G. P., Isotope ratio mass spectrometry. *Analyst* **2009,** *134* (2), 213-22.

3. Booksh, K. S.; Kowalski, B. R., Theory of analytical-chemistry. *Analytical Chemistry* **1994,** *66* (15), A782-A791.

4. Julian, R. K.; Cooks, R. G., Broad-band excitation in the quadrupole ion trap mass spectrometer using shaped pulses created with the inverse fourier transform. *Analytical Chemistry* **1993,** *65*, 1827-1833.

5. Fico, M.; Yu, M.; Ouyang, Z.; Cooks, R. G.; Chappell, W. J., Miniaturization and geometry optimization of a polymer-based rectilinear ion trap. *Analytical Chemistry* **2007,** *79* (21), 8076-8082.

6. Badman, E. R.; Cooks, R. G., A parallel miniature cylindrical ion trap array. *Analytical Chemistry* **2000,** *72* (14), 3291-3297.

7. Zhang, Z. P.; Peng, Y.; Hansen, B. J.; Miller, I. W.; Wang, M.; Lee, M. L.; Hawkins, A. R.; Austin, D. E., Paul trap mass analyzer consisting of opposing microfabricated electrode plates. *Analytical Chemistry* **2009,** *81* (13), 5241-5248.

8. Stafford, G. C.; Kelley, P. E.; Syka, J. E. P.; Reynolds, W. E.; Todd, J. F. J., Recent improvements in and analytical applications of advanced ion trap technology. *International Journal of Mass Spectrometry and Ion Processes* **1984,** *60* (Sep), 85-98.

9. March, R. E.; Todd, J. F. J., Quadrupole ion trap mass spectrometry, 2nd edition. *Quadrupole Ion Trap Mass Spectrometry, 2nd Edition* **2005,** *165*, 1-351.

10. March, R. E., An introduction to quadrupole ion trap mass spectrometry. *Journal of Mass Spectrometry* **1997,** *32* (4), 351-369.

11. Stick, D.; Hensinger, W. K.; Olmschenk, S.; Madsen, M. J.; Schwab, K.; Monroe, C., Ion trap in a semiconductor chip. *Nature Physics* **2006,** *2* (1), 36-39.

12. Tian, Y.; Higgs, J.; Li, A.; Barney, B.; Austin, D. E., How far can ion trap miniaturization go? Parameter scaling and space-charge limits for very small cylindrical ion traps. *Journal of Mass Spectrometry* **2014,** *49* (3), 233-40.

13. Kornienko, O.; Reilly, P. T. A.; Whitten, W. B.; Ramsey, J. M., Electron impact ionization in a microion trap mass spectrometer. *Review of Scientific Instruments* **1999,** *70* (10), 3907-3909.

14. Wells, J. M.; Badman, E. R.; Cooks, R. G., A quadrupole ion trap with cylindrical geometry operated in the mass selective instability mode. *Analytical Chemistry* **1998,** *70* (3), 438-444.

15. Ouyang, Z.; Cooks, R. G., Miniature Mass Spectrometers. *Annual Review of Analytical Chemistry* **2009,** *2*, 187-214.

16. Blain, M. G.; Riter, L. S.; Cruz, D.; Austin, D. E.; Wu, G. X.; Plass, W. R.; Cooks, R. G., Towards the hand-held mass spectrometer: design considerations, simulation, and fabrication of micrometer-scaled cylindrical ion traps. *International Journal of Mass Spectrometry* **2004,** *236* (1-3), 91-104.

17. Brownnutt, M.; Wilpers, G.; Gill, P.; Thompson, R. C.; Sinclair, A. G., Monolithic microfabricated ion trap chip design for scaleable quantum processors. *New Journal of Physics* **2006,** *8*.

18. Han, Y. H.; Cheung, G.; Li, A.; Sullivan, C. R.; Perreault, D. J., Evaluation of Magnetic Materials for Very High Frequency Power Applications. *Ieee Transactions on Power Electronics* **2012,** *27* (1), 425-435.

19. Schultze, K. P., Advanced System Components for the Development of a Handheld Ion Trap Mass Spectrometer, Ph.D. Dissertation. *UNC at Chapel Hill, North Carolina* **2014**.

20. Arnold, N. S.; Hars, C.; Meuzelaar, H. L., Extended theoretical considerations for mass resolution in the resonance ejection mode of quadrupole ion trap mass spectrometry. *Journal of the American Society for Mass Spectrometry* **1994,** *5* (7), 676-88.

21. McLuckey, S. A.; Van Berkel, G. J.; Goeringer, D. E.; Glish, G. L., Ion-trap mass-spectrometry of externally generated ions. *Analytical Chemistry* **1994,** *66* (13), A689-A696.

22. Major, F. G.; Dehmelt, H. G., Exchange-collision technique for Rf spectroscopy of stored ions. *Physical Review* **1968,** *170* (1), 91-107.

23. Dehmelt, H. G., Radiofrequency spectroscopy of stored ions I: storage. *Advances in Atomic and Molecular Physics* **1967,** *3*, 53-72.

24. Wu, G. X.; Cooks, R. G.; Ouyang, Z., Geometry optimization for the cylindrical ion trap: field calculations, simulations and experiments. *International Journal of Mass Spectrometry* **2005,** *241* (2-3), 119-132.

25. Badman, E. R.; Johnson, R. C.; Plass, W. R.; Cooks, R. G., A miniature cylindrical quadrupole ion trap: Simulation and experiment. *Analytical Chemistry* **1998,** *70* (23), 4896-4901.

26. Schrama, C. A.; Peik, E.; Smith, W. W.; Walther, H., Novel miniature ion traps. *Optics Communications* **1993,** *101* (1-2), 32-36.

27. Londry, F. A.; Wells, G. J.; March, R. E., Enhanced mass resolution in a quadrupole ion trap. *Rapid Communications in Mass Spectrometry* **1993,** *7* (1), 43-45.

28. Bartelt-Hunt, S. L.; Knappe, D. R. U.; Barlaz, M. A., A review of chemical warfare agent simulants for the study of environmental behavior. *Critical Reviews in Environmental Science and Technology* **2008,** *38* (2), 112-136.

29. Goeringer, D. E.; Whitten, W. B.; Ramsey, J. M.; McLuckey, S. A.; Glish, G. L., Theory of high-resolution mass-spectrometry achieved via resonance ejection in the quadrupole ion trap. *Analytical Chemistry* **1992,** *64* (13), 1434-1439.

30. Song, Q. Y.; Xu, W.; Smith, S. A.; Gao, L.; Chappell, W. J.; Cooks, R. G.; Zheng, O. Y., Ion trap mass analysis at high pressure: an experimental characterization. *Journal of Mass Spectrometry* **2010,** *45* (1), 26-34.

31. Xu, W.; Song, Q. Y.; Smith, S. A.; Chappell, W. J.; Ouyang, Z., Ion trap mass analysis at high pressure: A theoretical view. *Journal of the American Society for Mass Spectrometry* **2009,** *20* (11), 2144-2153.

32. Moxom, J.; Reilly, P. T. A.; Whitten, W. B.; Ramsey, J. M., Double resonance ejection in a micro ion trap mass spectrometer. *Rapid Communications in Mass Spectrometry* **2002,** *16* (8), 755-760.

33. Brewer, R. G.; DeVoe, R. G.; Kallenbach, R., Planar ion microtraps. *Physical review. A* **1992,** *46* (11), R6781-R6784.

34. Li, X. X.; Jiang, G. Y.; Luo, C.; Xu, F. X.; Wang, Y. Y.; Ding, L.; Ding, C. F., Ion trap array mass analyzer: structure and performance. *Analytical Chemistry* **2009,** *81* (12), 4840-4846.

35. Pau, S.; Pai, C. S.; Low, Y. L.; Moxom, J.; Reilly, P. T. A.; Whitten, W. B.; Ramsey, J. M., Microfabricated quadrupole ion trap for mass spectrometer applications. *Physical Review Letters* **2006,** *96* (12).

36. Ramsey, J. M.; Schultze, K., US Patent 2,014,064,001. **2014**.

37. Whitten, W. B.; Reilly, P. T. A.; Ramsey, J. M., High-pressure ion trap mass spectrometry. *Rapid Communications in Mass Spectrometry* **2004,** *18* (15), 1749-1752.

38. Ouyang, Z.; Wu, G. X.; Song, Y. S.; Li, H. Y.; Plass, W. R.; Cooks, R. G., Rectilinear ion trap: Concepts, calculations, and analytical performance of a new mass analyzer. *Analytical Chemistry* **2004,** *76* (16), 4595-4605.

39. Wang, Y.; Franzen, J., The nonlinear resonance quistor .1. potential distribution in hyperboloidal quistors. *International Journal of Mass Spectrometry and Ion Processes* **1992,** *112* (2-3), 167-178.

40. Piltingsrud, H. V., Miniature peristaltic vacuum pump for use in portable instruments. *Journal of Vacuum Science & Technology a-Vacuum Surfaces and Films* **1996,** *14* (4).

41. Young, R. M., Freidhoff, C. B., Micro-miniature diaphragm pump for low pressure pumping of gases. *US Patent 5,659,171* **1997**.

CHAPTER 5. CHARACTERIZING NEW ELECTRODE MATERIALS

5.1 Introduction

The primary goal of this project was to demonstrate HPMS at 1 Torr with ambient air as the buffer gas. By eliminating the turbopump and using ambient air as the buffer gas, significant SWaP savings are achieved to the extent that a field portable instrument is feasible. Because peak widths widen as pressure increases, scaling ion traps down to 100 µm and operating at RF frequencies up to 60 MHz regained sub-unit mass resolution. Eliminating the turbopump is the major factor in reducing SWaP but it is worth looking at each component of the MS under development for further SWaP savings. Glow discharge ionization is available as a pressure tolerant, low power ionization source although a solid state microionizer currently under development could further decrease power and size requirements by two orders of magnitude. Faraday cup detectors are being optimized for sensitivity and operate independently of pressure as a potential replacement for electron multipliers.

Wet etched metal ion trap electrodes were the standard traps used for developing HPMS, but there is interest in re-evaluating the material selection in terms of SWaP and also fabrication procedures. For SWaP, the focus would be on reducing the ion trap's capacitance that would help alleviate RF power draw. For fabrication, improving fabrication dimensional tolerances so that large ion trap arrays are possible would increase sensitivity while

maintaining mass resolution. Fabrication methodology for potential reductions in production costs is also a consideration.

Reducing the ion trap capacitance is important to SWaP as the RF power required to produce the trapping fields is directly related to the capacitance squared. This is of importance as in order to reach unit resolution under high pressure, it was necessary to increase the RF drive frequency from 6 MHz to 60 MHz. Fundamentally this corresponds to a factor of 100 increase in RF power. Trap sizes were also reduced; traps went from 250 µm spacing between electrodes for a 500 µm ion trap to 50 µm spacing for a 100 µm ion trap. With this lower spacing the capacitance of the ion trap is expected to increase by a factor of 5, corresponding to power requirements increasing by a factor of 25. The CITs used so far were designed for maximizing experimental flexibility and not minimizing capacitance. A trap design that reduces capacitance compared to the CITs would decrease the power requirements for highly miniaturized ion traps operated at frequencies approaching 60 MHz.

Trap capacitance is a function of the conductive surface area of the electrodes and spacing between electrodes. For a specific ion trap, the electrode spacing is fixed, so to achieve a reduction in capacitance the focus was on reducing the conductive surface area of each electrode. One method to achieve this would be by using printed circuit board technology. With printed circuit board fabrication, it is possible to pattern conductive features onto an insulating layer, which leaves minimal conductive surface area in relation to the board. In fact, printed circuit boards have already found niche uses in mass spectrometry to date including ion optics[1], transport of ions through linear ion traps[2], and FT-ICR analyzer cells.[3] There is also significant interest in PCB based ion traps for quantum computing.[4-7]

The capacitance was not a concern for these applications however they demonstrate that PCB-based fabrication of MS components is feasible.

Another consideration for microscale ion traps is improving electrode fabrication tolerances, especially for ion trap arrays and SLITs**.** Differences in r_o between array elements can cause mass resolution to decrease as identical mass ions could be ejected over a span of time. Wet etched ion trap tolerances are specified as ± 10% from r_o target dimensions for the current CITs. For SLIT traps the accuracy of the x_o dimension was ± 10%, while variations up to 20 µm in x_o along the y_o axis have also been observed with x_o = 100 µm SLIT traps. If further miniaturization is desired using wet etch techniques, there are limited commercially available sheet metal thicknesses at or below the 130 µm thickness required to fabricate them. While custom sheet metal thicknesses are possible, they come with the drawbacks of increased fabrication costs and material expense. Furthermore, thin sheet metal loses its structural rigidity, compromising the tight dimensional control that microscale ion traps require. Therefore, alternative methods of fabrication with tighter tolerances are needed.

Microelectromechanical systems (MEMS) technologies are proven fabrication techniques for creating micro and nanoscaled features. For SLIT or array trap fabrication using photolithography and deep reactive ion etching (DRIE), it is possible to fabricate ion traps with ± 1% tolerances. These tolerances are important for ensuring the ion trap dimensions are maintained between array elements. This would minimize differences in electric field components helping to ensure simultaneous ion ejection from each trap of the array or along the length of a SLIT. In addition to maintaining or improving mass resolution, sensitivity and mass range would also be improved. Beyond intra-electrode dimensional

control, maintaining dimensions between batches of ion traps should make performance metrics predictable between traps.

Printed circuit board ion traps and highly doped n-type silicon ion traps were investigated as alternative electrode materials to sheet metal. PCB electrodes were designed to decrease ion trap capacitance and decrease power requirements for the drive RF. Silicon ion traps with more reproducible dimensions (± 1%) were fabricated to improve both intra-electrode dimensions for arrays and batch to batch reproducibility. Their performance was analyzed at high pressures of ambient air with glow discharge ionization. The new electrodes were designed with comparable critical dimensions to previously studied CIT used at elevated RF drive frequencies for comparison.

5.2 PCB Traps

Figure 5.1 shows the difference in conductive surface area between the previously studied BeCu electrodes (Figure 5.1a) and a PCB trap (Figure 5.1b). For the metal ring and endcap electrodes, the entire surface is conductive so when the ring electrode is aligned with the endcap electrodes, there is significant overlap of conductive surfaces leading to increased capacitance. This overlap includes the areas around the alignment pin and mounting screw holes that do not influence the ion trap's performance. For the PCB electrodes, the Cu is patterned to the circuit board material (FR-4) forming just a solder region and CIT feature linked together. The majority of the surface area is non-conductive FR-4 insulator so when the ring and endcap electrodes are aligned, only the CIT feature in the center of the electrode should overlap. The difference in overlapping surface area between the metal and PCB traps is decreased by approximately a factor of 75 and with it there is a drop in capacitance.

Another benefit is a reduction in potential electrical breakdown paths through the alignment features and mounting screw holes. Multi-layer PCB are possible raising the possibility of a multi-layer PCB trap that requires no assembly eliminating manual assembly time (15 to 30 minutes) and potentially further reducing capacitance.[8-9]

The reproducibility for PCB electrodes including the thicknesses of patterned Cu layers and the aperture dimensions resulting from conventional milling are concerns. In most circuit board applications, the patterned Cu is used to connect electrical components so large tolerances are acceptable. The thickness of the patterned Cu determines the z_o dimension, and the aperture drilled into the PCB board determines r_o, so both need to be accurate and reproducible.[10-11] The machining process could also leave a rough sidewall that requires post-processing to improve.[12] Laser machining is another technique that could be used to form apertures, although the tapering for a cylinder or slot formed by laser etching that could exceed 10% is a concern.[13-14]

5.2.1 PCB Electrode Physical Properties

Three different PCB ring electrodes were fabricated on FR-4 material as the base material with patterned Cu forming the conductive features (Figure 5.2). There were two CITs with r_o dimensions of (a) 130 µm, (b) 100 µm and (c) a x_o = 240 µm single SLIT. The critical dimensions were adjusted by etching the deposited Cu to meet the desired dimensions that were comparable to previously studied metal electrodes. Aqua regia, a 3:1 mixture of concentrated HCl to HNO_3, was used to etch the Cu layer on the FR-4 material. This isotropic wet etch increased the diameter of the electrode aperture and decreased the thickness of the electrode by 20 µm to 70 µm. The electrodes were etched for between 3 to

20 minutes depending on the amount of Cu to be removed. While a more precise etching method is possible, aqua regia was chosen for its speed.[15-16] If PCB traps are proven feasible, more precise control of the critical dimensions during fabrication would eliminate the etch step.

The capacitance of four trap configurations was measured with an inductance, capacitance, and resistance (LCR) meter sampling at 1 kHz. The trap configurations consisted of an (a) all BeCu trap (MCIT), (b) PCB endcaps: BeCU ring electrode (hy-MCIT), (c) BeCu endcaps: PCB ring electrode (hy-PCIT) and (d) all PCB trap (PCIT) (Figure 5.3). The spacing between all electrodes was 50 μm and the SMA feedthrough used to transmit the RF trapping voltage to vacuum from the RF amplifier at atmosphere accounted for approximately 1 pF. Accounting for the contribution of the SMA feedthrough to the measured capacitance, the MCIT had a capacitance of 24 pF and when the BeCu ring electrode was replaced with a PCB ring electrode (hy-PCIT), the capacitance dropped 92% to 2 pF. The hy-MCIT had a capacitance of 4 pF. While the two hybrid configurations should have the same capacitance, it is believed fringing field capacitance accounts for the 50% higher capacitance that was observed for the hy-MCIT.[17-18] For the PCIT, the capacitance was 1 pF or 96% lower than the MCIT.

5.2.2 PCB Trap Performance

PCIT had significantly lower capacitance (92% to 96%) than MCIT. While this capacitance improvement is significant, the advantage of lower capacitance would be offset if significant losses in sensitivity and mass resolution also occur. To compare sensitivity between MCIT and PCIT, r_o = 130 μm traps from both materials were run. Figure 5.4 shows

spectra from both ion traps run at 41 MHz drive RF with a pressure of 1.0 Torr of air. The comparison was done similarly to the SLIT and CIT in Chapter 4 (Figure 4.9). The ionization time was kept constant, although the ion accelerating voltage was optimized to maximize the signal. The axial RF conditions producing the narrowest peak widths were used. A factor of two difference in signal between the MCIT than the PCIT was observed. The signal difference is likely an effect of differences in sidewall profiles between the fabrication techniques and/or rough sidewalls produced by the conventional milling of the PCB traps that add higher order field components that are detrimental to sensitivity.

To compare mass resolution, three different PCIT (Table 5.1) with r_o comparable to MCITs were fabricated. The first trap studied was a r_o = 165 µm hybrid MCIT with a BeCu ring electrode and PCB endcaps (Figure 5.3b). Mass spectra of *p*-xylene were recorded as a function of RF drive frequency from 21.67 MHz to 25.07 MHz with 1.0 Torr of ambient air as the buffer gas (Figure 5.5). The RF drive frequency was limited to a maximum value of 25.07 MHz by electrical breakdown, which destroyed the traps. The three peaks at 106 Da, 91 Da, and 77 Da were seen as with the MCIT. Peak widths over the 3.4 MHz range decreased 20% from 2.87 Da to 2.31 Da. The next ion trap analyzed was a r_o = 130 µm PCIT. From 36.06 MHz to 43.96 MHz in 1.0 Torr of ambient air peak widths decreased 20% from 1.55 Da to 1.24 Da (Figure 5.6).

The peak widths for the hy-MCIT and PCIT were compared to MCITs (Figure 5.7). For the hy-MCIT, the peak width was 3.57 Da at 17.46 MHz compared to 3.48 Da for a r_o = 165 µm MCIT operated at 17.31 MHz. This translates to a 2.5% difference in peak widths for a 0.9% difference in RF drive frequency, well within experimental error. At higher RF frequencies, the hy-MCIT had a peak width of 2.71 Da at 23.06 MHz compared to 2.96 Da

for the r_o = 165 µm MCIT operated at 22.87 MHz. Here the RF frequencies were different by 0.8% while the peak widths varied by 8.5%. One difference was this MCIT used the 1/3 hexapolar resonance while the 1/4 octopolar resonance was used for the hybrid trap. With the hybrid trap using the octopolar resonance instead of the hexapolar resonance, this improvement in mass resolution was not surprising.

Peak widths for the r_o = 130 µm PCIT were compared to the r_o = 100 µm MCIT. At 39.56 MHz the r_o = 130 µm PCIT had a peak width of 1.47 Da compared to 1.62 Da for the r_o = 100 µm MCIT at 40.38 MHz. The MCIT was operated at a 2.1% higher RF frequency while its peaks were 10% wider than the PCIT. At higher RF frequencies, the r_o = 130 µm PCIT had a peak width of 1.24 Da at 43.96 MHz compared to 1.32 Da for the r_o = 100 µm MCIT at 45.42 MHz. This corresponded to the PCIT operating at a lower RF frequency by 3.3% but still having 6.5% narrower peak widths than the MCIT.

There are several possible explanations to why the PCITs had better mass resolution than the MCITs. The higher order field components for the PCITs with cylindrical sidewalls are different from the MCITs that have wet etched sidewall profiles.[19-20] A second possible reason is that lower capacitance means the RF amplifiers run more efficiently with lower power draw producing less heating of the trap

With the PCIT showing better mass resolution compared to MCIT, a PCB SLIT trap (PSLIT) was also compared. A x_o = 240 µm PSLIT was run at 1.0 Torr of ambient air over the RF drive frequency range of 16.76 MHz to 25.76 MHz (Figure 5.8). RF voltage requirements limited the highest RF drive frequency to 25.76 MHz. The 1/4 octapole axial RF resonance was used for all the SLIT electrodes. Peak widths for the x_o = 240 µm PSLIT

were compared to a x_o = 270 µm BeCu SLIT (MSLIT) (Figure 5.9). At 16.76 MHz the PSLIT had peak widths of 3.77 Da compared to 3.29 Da peak widths for the MSLIT at 16.96 MHz. While the RF frequency was 1.2% higher for the MSLIT, its peak widths were 13% narrower. With higher RF frequencies the PSLIT had peak widths of 2.71 Da at 23.06 MHz while the MSLIT operated at a 1.7% lower RF frequency of 23.46 MHz had peak widths of 2.44 Da or 10% lower. The likely reason for MSLIT having narrower peak widths than the PSLIT was the bowing features near the ends of the SLIT features. These features significantly change the y_o dimension near the boundaries of the trap and could significantly affect the ion motion near those regions, causing a loss in mass resolution.

The order of magnitude lower capacitance for PCIT compared to a MCIT should decrease power requirements by a factor of 100, significantly improving the power budget for a miniature RF system operated at elevated RF drive frequencies. For these experiments, the broadband benchtop RF amplifier, used because of the capability to dial in different frequencies, was unable to achieve these power benefits. The amplifier still required 50 W to operate and the power draw was independent of the RF frequency. Recently, however, a miniaturized RF amplifier used with a 6 pF r_o = 500 µm CIT was operated at a RF frequency of 7.63 MHz drew only 4.8 W of power.[21] This is an order of magnitude improvement in power draw compared to the benchtop RF amplifier. The benchtop amplifier was used because it is a broadband amplifier whereas the miniaturized RF amplifiers are optimized for a single RF frequency, and cannot be used to study large frequency ranges. This suggests that once target RF frequencies are determined, the power savings can be achieved with miniaturized RF amplifiers operational at single frequencies. With these miniaturized single

frequency RF amplifiers, the lower capacitance of the PCB traps should improve the power draw as predicted.

While the PCB electrodes are successful in reducing capacitance, there are performance tradeoffs. Sensitivity was a factor of two better for the MCIT than the PCIT. PCB based CITs had narrower peak widths by up to 10% compared to the MCITs. The SLIT electrode experiments showed that dimensional fabrication tolerances for PCB ion traps could limit mass resolution for SLIT geometries. The tradeoffs between RF power and frequency were also observed. By decreasing the capacitance of an ion trap, higher RF frequencies can be used without any increase in RF power. Since PCITs decreased capacitance by up to a factor of 10, a factor of 10 higher RF frequency could be used to improve mass resolution with no difference in RF power draw.

A common fabrication method for PCB boards is to bond multiple layers. This could be taken advantage of by bonding multiple electrode layers and then milling through them, eliminating the need to stack and align electrodes by hand. A new ion trap was designed that does not require manual assembly, eliminating much of the potential for human error in constructing reproducible ion traps. The new PCB ion trap design (Figure 5.10) consists of four Cu layers separated by three FR-4 insulating layers. The seven layers are permanently bonded together to form an integrated ion trap PCB. The two outer Cu layers (81 μm and 99 μm) serve as the endcap electrodes, while the two inner Cu layers (60 μm and 55 μm) act as ring electrodes.

There were two copper ring electrodes due to fabrication considerations. Two FR-4 substrates were patterned on both sides to form endcap and ring electrode features. These

two patterned FR-4 boards were then bonded to opposite sides of a third FR-4 substrate to form the integrated electrode stack. Using a single ring electrode would have resulted in more difficult and expensive fabrication. Both ring electrodes are connected to the drive RF. The ring electrodes are separated by 112 µm, while the endcap electrodes are separated from the nearest neighbor ring electrode by 100 µm and 121 µm. The electrodes were machined to a diameter of 600 µm to form the trapping fields, and the overall dimensions were r_o = 300 µm and z_o = 225 µm. The diameters of the ring and endcap electrodes are all the same (600 µm), which lowers capacitance and simplifies fabrication by eliminating the need to manually align and stack the electrodes in multiple steps. Capacitance for this ion trap was 4 pF.

The bonded PCB ion trap successfully demonstrated mass analysis at elevated pressures (715 mTorr of ambient air) with *p*-xylene as the analyte (Figure 5.11). Three peaks were observed at 77 Da, 91 Da, and 106 Da as expected. Peak widths were approximately 4 Da which were higher than anticipated, but not surprising since the aperture feature was formed with a drill bit, leaving burrs and other machining features that could influence trap performance. Future designs could use post-processing techniques such as polishing or etching to improve the electrode profile. This design fulfilled its purpose of demonstrating an integrated ion trap that requires no electrode hand assembly. Since hand-assembly of ion traps requires significant time (10 to 60 minutes), an integrated design decreases fabrication time, human error, and cost.

5.3 Silicon Ion Traps

Micro-electro-mechanical system (MEMS) technology has been investigated as a cost effective method for fabricating miniature mass analyzers in large quantities.[22-23] Mass analyzers that have been miniaturized using MEMS technology include quadrupole mass filters[24-25], time of flight[26], and sectors.[27] Of most interest are MEMS based approaches to fabricating miniaturizing ion traps. Both reactive ion etching (RIE) and deep reactive ion etching (DRIE) have been used to fabricated CITs (r_o = 360 μm) with silicon and silicon on insulator (SOI) wafers.[28-30] Silicon micromachining and tungsten metallization was used to fabricate 1μm CIT arrays with up to 10^6 elements.[31-32] CIT arrays with r_o = 20 μm (256 and 1028 elements) were fabricated from polysilicon and silicon dioxide layers.[33] A planar Paul ion trap was constructed with two ceramic plates patterned with metal rings that were overlaid with germanium.[34] While MEMS technology has been used to fabricate miniaturized mass analyzers, they have not been widely introduced into fully miniaturized instruments.

For this project, silicon ion trap electrodes were fabricated in highly doped n-type silicon with a nominal resistivity of 0.003 Ω-cm by DRIE Bosch. The Bosch process was patented in 1996 as a highly anisotropic etching method for fabricating high aspect ratio features exceeding 50:1 with near 90 degree sidewalls (Figure 5.12).[35] The process starts by using a substrate that has been photolithographically patterned exposing areas to be etched. The first step of the Bosch process uses an SF_6 plasma to etch away a thin layer of the substrate forming a trench (Figure 5.12a). This is followed by a passivation layer of CF_x deposited on the substrate trench and sidewalls (Figure 5.12b). The SF_6 plasma is reintroduced and directionally etches the passivation layer more quickly on the trench bottom

thus etching into the silicon while the sidewalls remain protected by the passivation layer (Figure 5.12c). The process is repeated until the desired feature depth is reached. The etch depth per step is critical as large step sizes used to minimize fabrication times can result in scalloping along the sidewalls from the alternating etching and deposition steps.[36-38] This could lead to higher order fields adversely effecting resolution.

5.3.1 Silicon Electrodes Physical Properties

Silicon electrodes were used to build three silicon CITs (SCIT) (Table 5.2) with r_o = 225 µm, r_o = 250 µm, and r_o = 130 µm. The SCIT were designed to replace the MCIT with minimal chamber modification while using the same electrical contact scheme. Figure 5.13 shows images of silicon electrodes and ion traps. Figure 5.13a shows a 7-element CIT silicon array with r_o = 250 µm. The four mounting holes are in the same position as the BeCu electrodes, and four 1 mm features can be used for electrode alignment. A sputter coater was used to deposit Cu on the silicon surface for improved electrical contact. With this design the solder tabs located near the mounting screw holes were found to be fragile. In the second design (Figure 5.13b), the solder tabs were replaced by a triangular soldering pad similar to those used with the metal electrodes. SEM imaging of the silicon traps was used to examine the sidewall roughness, which could affect ion trap performance.[12] Figure 5.13c shows smooth sidewalls for a r_o = 250 µm CIT where there is little evidence of scalloping from the etch process.

Although not specifically developed to reduce the capacitance, the capacitance for the various silicon based traps was also measured. The r_o = 130 µm SCIT had a capacitance of 12 pF compared to 24 pF and 1 pF for a MCIT and PCIT with the same r_o. The SCIT trap

decreased capacitance by a factor of 2 compared to the MCIT but increased capacitance by a factor of 12 compared to the PCIT. RF power with an optimized RF amplifier setup for the SCIT trap is expected to be a factor of 4 lower than the MCIT but a factor of 144 higher than the PCIT. The SCIT trap design was optimized for structural rigidity and not low capacitance, so a large decrease in capacitance comparable to the PCIT was not expected. Overlapping surface area was lower than that MCIT by approximately 20%, so the factor of 2 decrease in capacitance was not surprising. This suggests that improved RF power performance could be achieved with the silicon based traps.

5.3.2 Silicon Ion Trap Performance

As with the PCIT, signal strength and mass resolution were compared with the MCIT. The signal strength comparison was performed with a r_o = 130 μm SCIT and MCIT operated at 1.0 Torr ambient air with *p*-xylene as the analyte (Figure 5.14). Both ion traps were run at 42 MHz drive RF and the axial RF voltage and frequency were optimized for maximum mass resolution. The ionization times were identical, although the glow discharge accelerating voltage was optimized to maximize signal. The SCIT had approximately a factor of two better integrated signal than the MCIT. This is unsurprising since the sidewalls produced by DRIE are more uniform and smooth than the wet etched MCIT. This could result in better-defined electrical fields that improve signal strength.

To compare mass resolution between silicon and MCITs, three different SCITs were studied. The first was a hybrid CIT with a silicon ring electrode with r_o = 225 μm and 200 μm diameter BeCu aperture endcaps (hy-SCIT). Mass spectra with *p*-xylene were recorded at 1.0 Torr of ambient air over a RF drive frequency range of 17.90 MHz to 21.50 MHz

(Figure 5.15). Three *p*-xylene peaks at 106 Da, 91 Da, and 77 Da were observed as expected. For this trap peak widths decreased by 0.49 Da or 15% over a 3.6 MHz range. The next trap was a SCIT with r_o = 250 µm and 200 µm aperture endcaps. Mass spectra were recorded from 15.20 MHz to 24.70 MHz (Figure 5.16) in 1.0 Torr of ambient air. Peak widths decreased 34% from 3.26 Da to 2.14 Da over a RF frequency range of 9.5 MHz. A further miniaturized SCIT with r_o = 130 µm and 165 µm aperture endcaps was run in 1.0 Torr of ambient air with RF frequencies from 31.66 MHz to 46.96 MHz (Figure 5.17). Peak widths decreased from 1.64 Da to 0.99 Da or 40% over a RF frequency range of 15.3 MHz.

Peak widths for each of the three SCITs were compared to MCIT (Figure 5.18). For the hy-SCIT, peak widths were compared to the r_o = 225 µm MCIT. At 17.90 MHz the silicon ion trap had peak widths of 3.53 Da while the MCIT had peak widths of 3.48 Da at 17.31 MHz. The RF frequency for the hy-SCIT was 3.3% higher while peak widths were 1.4% wider than the MCIT. At higher RF frequencies the hy-SCIT had peak widths of 3.18 Da at 20.5 MHz compared to 3.32 Da for the MCIT at 20.1 MHz. The hy-SCIT was operated at a RF frequency 2.0% higher while its peak widths were 4.4% narrower. For the hy-SCIT there was excellent agreement in peak widths with the MCITs, suggesting that the material and corresponding geometry change had minimal effects on mass resolution.[10]

Peak widths for the r_o = 250 µm SCIT were compared to the r_o = 225 µm MCIT. At 15.20 MHz the SCIT had peak widths of 3.26 Da while the MCIT had 3.75 Da peak widths at 15.33 MHz. The SCIT was run at a 0.9% lower RF frequency and had 15% narrower peak widths than the MCIT. At higher RF frequencies, the SCIT had peak widths of 2.37 Da at 21.10 MHz while the MCIT had peak widths of 3.32 Da at 20.10 MHz. The MCIT was operated at a RF frequency 4.7% lower than the SCIT while its peak widths were

disproportionally wider (40%). The significant improvement in peak width in excess of 30 % for the SCIT compared to the MCIT was unexpected. The silicon ring electrode was similar to the hybrid trap, suggesting that the addition of silicon endcap electrodes significantly improves ion trap performance.

Peak widths for the r_o = 130 μm SCIT were compared to the r_o = 100 μm MCIT. The SCIT had peak widths of 1.16 Da at a RF drive frequency of 41.46 MHz opposed to 1.62 Da for the MCIT at 40.38 MHz. The RF frequency for the SCIT was higher by 2.7% while the peaks widths were 40% narrower. With higher RF frequencies, the SCIT had peak widths of 0.99 Da at 46.96 MHz compared to 1.32 Da for the MCIT at 45.42 MHz. Peak widths for the SCIT were 33% narrower while the RF frequency was 3.2% higher.

Once again, peak widths were significantly improved for the SCIT compared to the MCIT. Unit mass resolution was achieved at 53 MHz for the MCIT opposed to 47 MHz for the SCIT. This 11% decrease in RF frequency of 6 MHz for achieving unit resolution should decrease RF amplifier power requirements by 22%. While the cause of the mass resolution improvement with silicon ion traps compared to MCIT remains under investigation, the trend was reproducible over different traps of the same dimensions and across a factor of two critical dimensions.

There were questions concerning the viability of silicon ion traps that were addressed through quantitatively studying their sensitivity and mass resolution. Structural rigidity was another concern since silicon wafers as thin as 80 μm were investigated. The microscale silicon ion traps were hand assembled, showing they were more rugged than initially expected. Several traps were successfully taken apart and reassembled despite their fragility.

Reliable electrical contact was made through metallization and soldering despite high RF frequency and voltage requirements in excess of 1 kV (p-p). While wire bonding also has potential as a high throughput method for making electrical contact, soldering simplified the trap construction compared to previously proven methods.[39-41]

5.4 Conclusions

Ion traps fabricated using PCB fabrication and MEMS technology were tested under HPMS operating conditions. The capacitance for CITs fabricated from PCB were compared to BeCu traps and found to decrease by 96% from 24 pF to 1 pF. Two PCITs were fabricated, one was a hybrid trap with a r_o = 165 µm BeCu ring electrode and 220 µm PCB endcaps, and the other a r_o = 130 µm PCB ring electrode with 165 µm PCB endcaps. A PSLIT with x_o = 240 µm was also fabricated. There was a factor of 2 lower signal for a r_o = 130 µm PCIT compared to a MCIT. The hybrid PCB trap (PCB endcaps, BeCu ring) had nearly identical mass resolution to the MCIT, while the 130 µm PCIT had approximately 5% better peak widths. In comparison, the PSLIT trap had wider peak widths by approximately 10%, showing the fabrication limitations of PCBs since bowing was observed. A stacked PCB trap requiring no manual assembly was also demonstrated at 715 mTorr.

Ion traps were also fabricated from silicon wafers and analyzed under HPMS operating parameters. Three CITs were fabricated, the first being a hybrid trap with a r_o = 225 µm BeCu ring electrode and 200 µm silicon endcaps. The other two CITs had all silicon electrodes were r_o = 250 µm with 200 µm endcaps, and r_o = 130 µm with 165 µm endcaps. The SCIT had a factor of 2 higher signal than a r_o = 130 µm MCIT. The hybrid silicon CIT had the same peak widths as the MCIT within experimental error. In comparison, the 250

μm SCIT had peak widths that were better than the MCIT by approximately 30%, which was believed to be an effect of the field profiles in the trap. The 130 μm SCIT showed similar peak widths improvements of 30% compared to the MCIT. With the PCB and silicon traps demonstrating peak widths at or exceeding unit mass resolution, the capacitance and dimensional tolerance concerns associated with wet etching of sheet metal could be addressed. Furthermore, both fabrication methods are amenable to manufacturing, a key metric for ion trap miniaturization on a large scale.

5.5 Tables and Figures

r_o or x_o (μm)	z_o (μm)	Insulator Thickness z_o (μm)	Ring Electrode Thickness z_o (μm)	Endcap Hole Diameter z_o (μm)
165	203	75	255	200
130	150	45	210	220
240	300	150	300	460

Table 5.1 Critical dimensions for the PCB ion traps used to compare performance with traps of different materials.

r_o or x_o (μm)	z_o (μm)	Insulator Thickness z_o (μm)	Ring Electrode Thickness z_o (μm)	Endcap Hole Diameter z_o (μm)
225	285	125	320	200
250	280	125	310	200
130	175	75	255	165

Table 5.2 Critical dimensions for the silicon ion traps used to compare performance with traps of different materials.

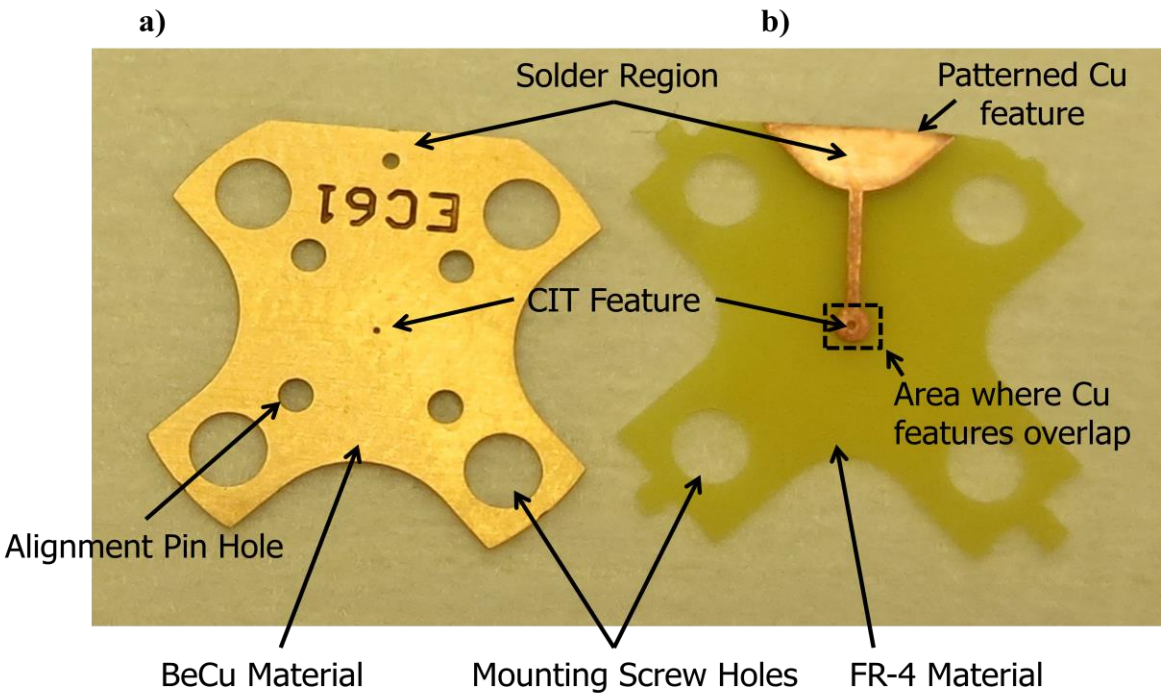

Figure 5.1: Images comparing a) BeCu and b) PCB ion trap electrodes. The PCB ion traps are only conductive where copper was patterned, decreasing capacitance when the ion trap electrodes are stacked.

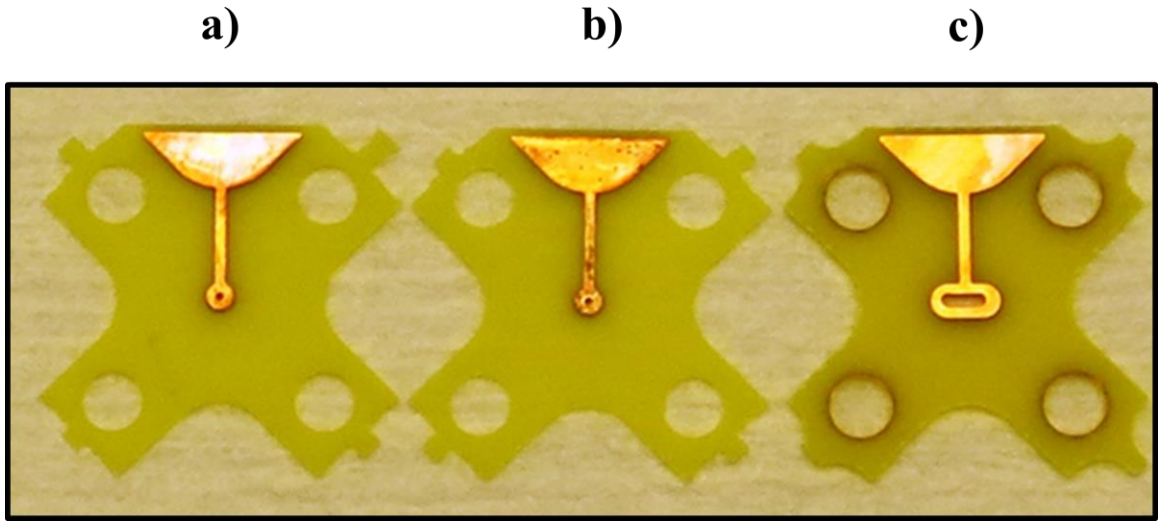

Figure 5.2: Images of PCB ion trap electrodes with a) r_o = 130 µm CIT, b) r_o = 100 µm CIT, c) x_o = 240 µm SLIT. Cu is plated on the FR-4 fiberglass material to minimize the overlapping Cu material and thereby minimize capacitance.

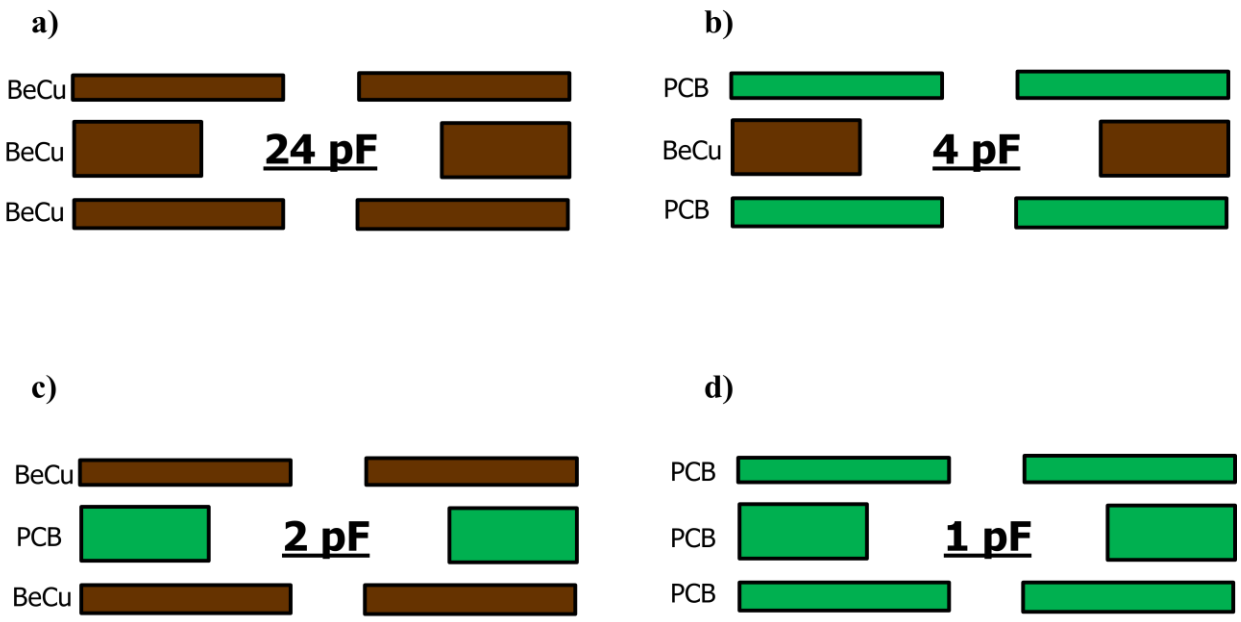

Figure 5.3: Capacitance measurements for different PCB trap configurations with 50 μm spacing between the ring and endcap electrodes. (a) MCIT, (b) hy-MCIT, (c) hy-PCIT and (d) PCIT. Approximately 1 pF of capacitance was from the vacuum SMA feedthrough used to transmit the RF signal to the trap chamber.

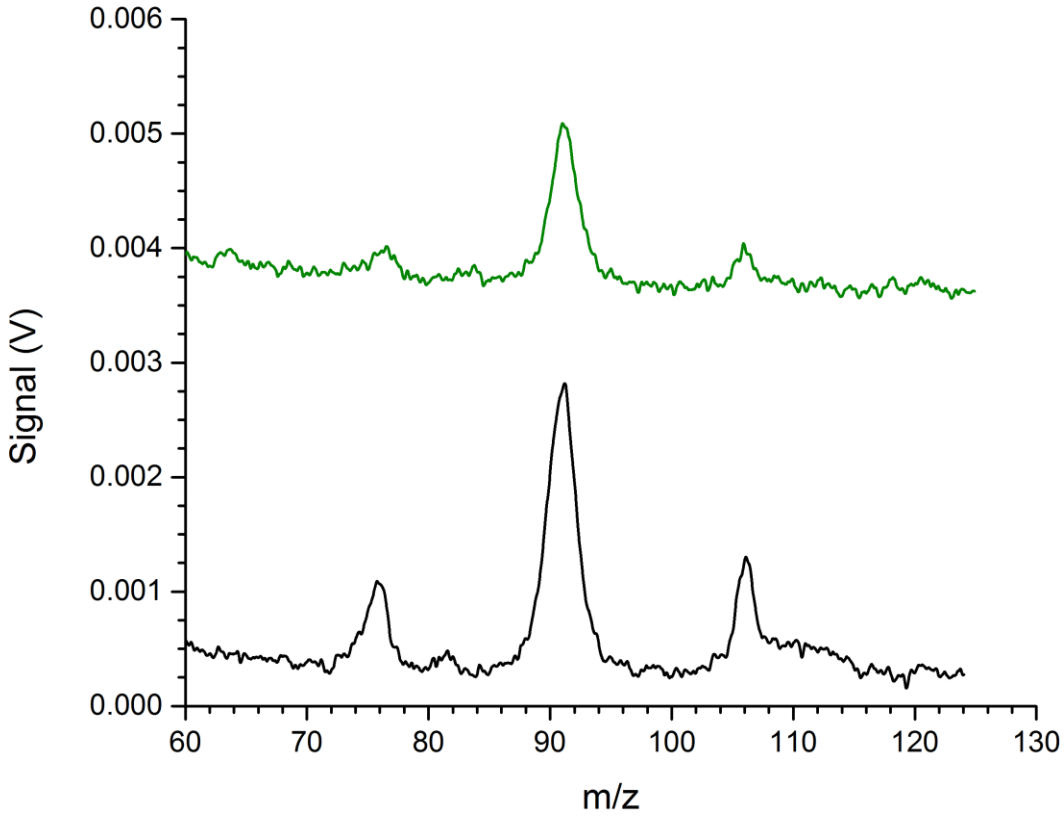

Figure 5.4: Mass spectra of *p*-xylene for r_o = 130 µm CITs operated with a RF frequency of 41 MHz at 1.0 Torr of ambient air comparing signal strength for MCIT (——) and PCIT (——).

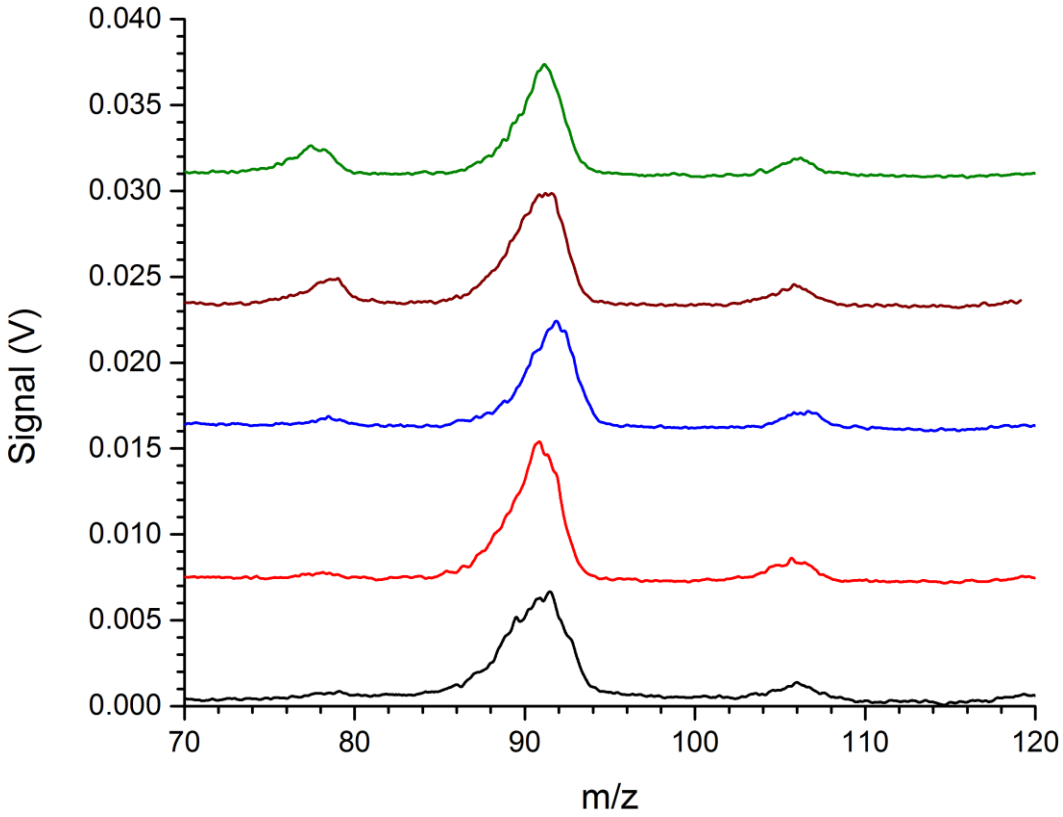

Figure 5.5: Mass spectra of *p*-xylene for a r_o = 165 µm hy-MCIT at RF drive frequencies of 21.67 MHz (——), 22.57 MHz (——), 23.57 MHz (——), 24.17 MHz (——), and 25.07 MHz (——).

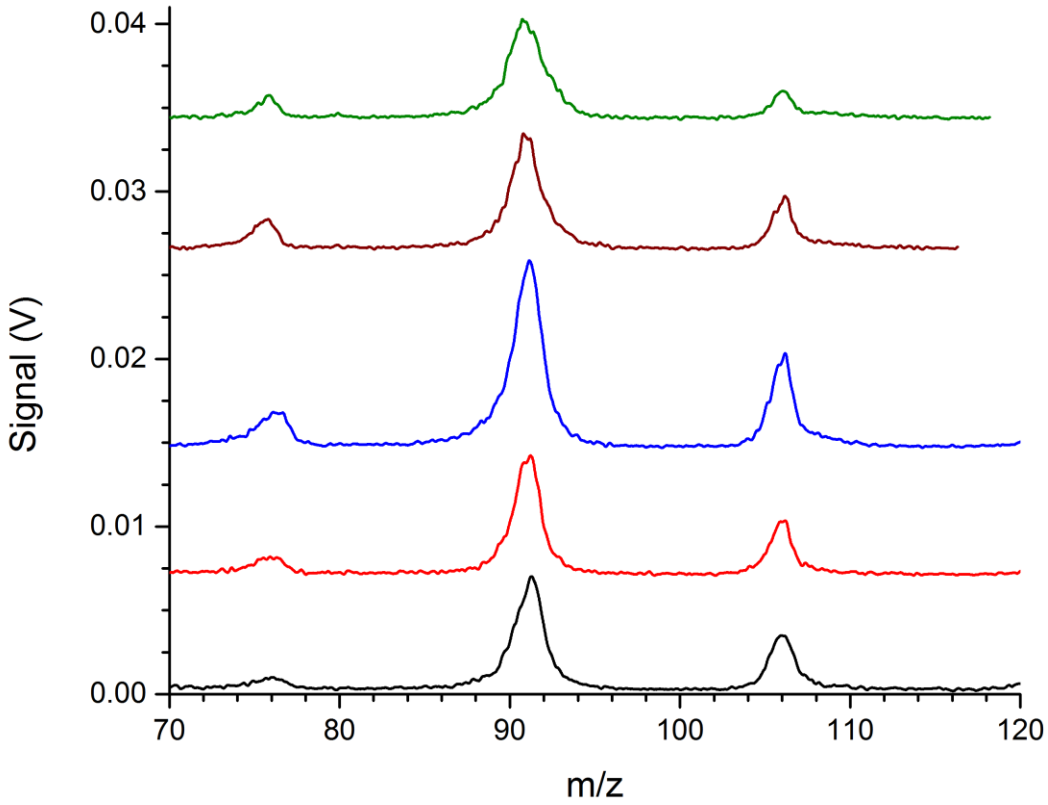

Figure 5.6: Mass spectra of *p*-xylene for a r_o = 130 µm PCIT at RF drive frequencies of 36.06 MHz (——), 37.66 MHz (——), 39.56 MHz (——), 41.56 MHz (——), and 43.96 MHz (——).

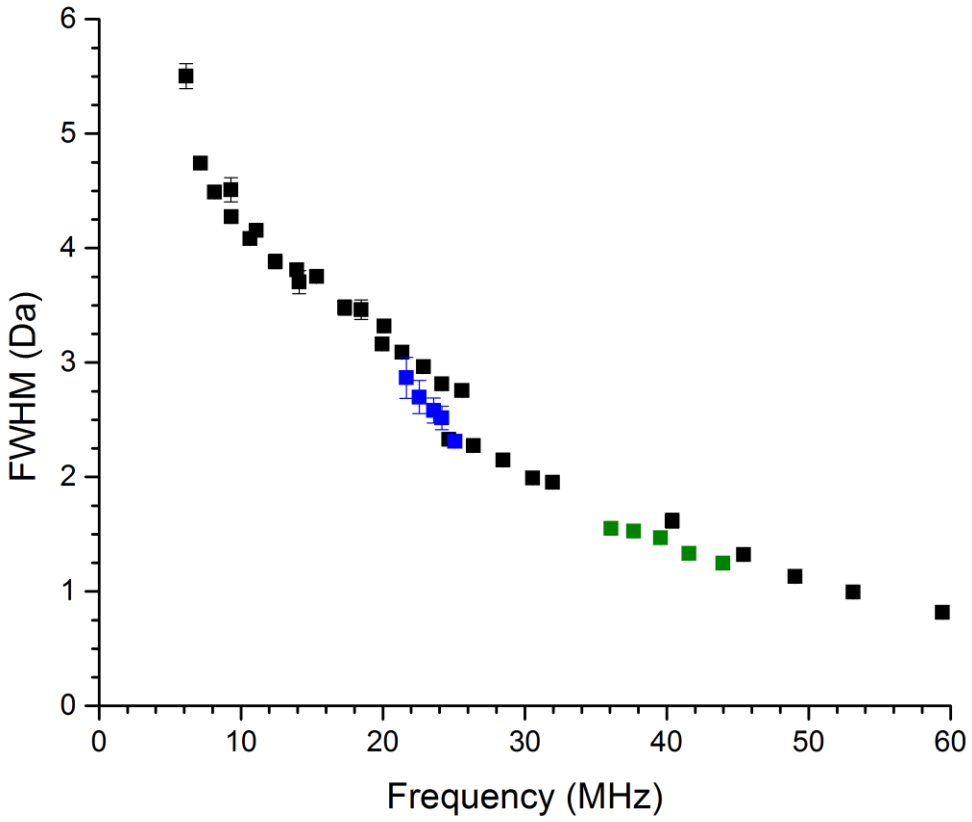

Figure 5.7: Peak widths for *p*-xylene 106 Da with increasing RF drive frequency for MCITs (■), a hy-MCIT (■), and PCIT (■). The PCITs decrease capacitance and therefore the power required for RF trapping voltages.

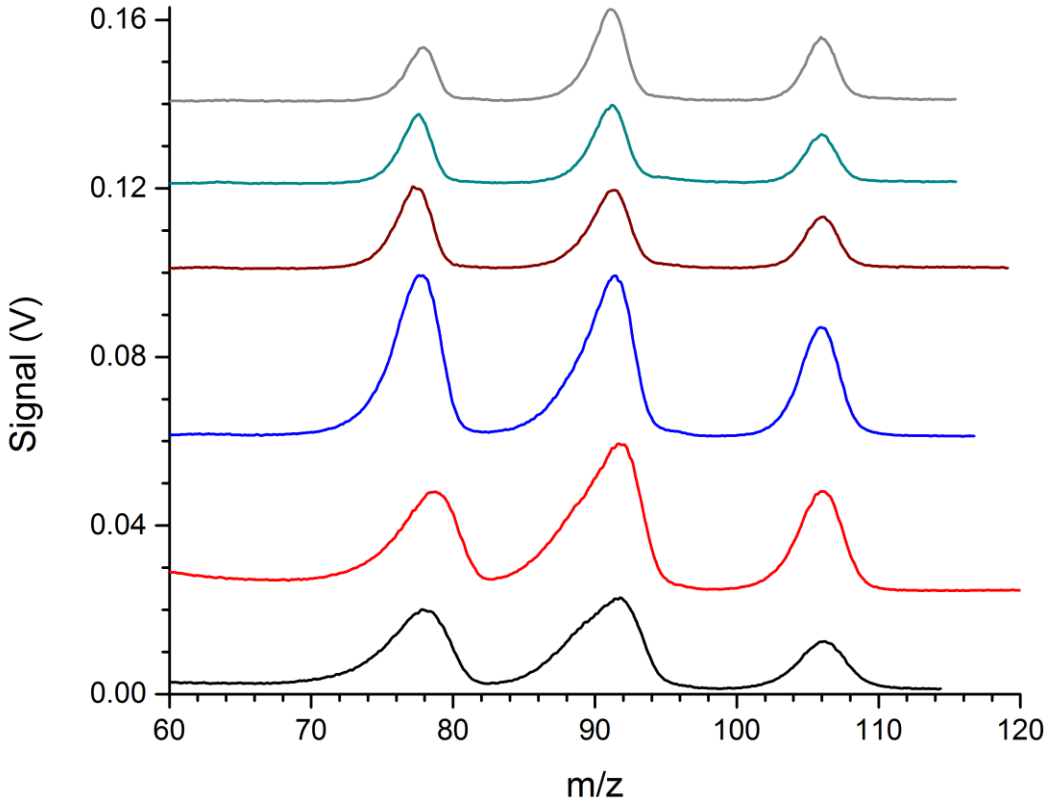

Figure 5.8: Mass spectra of *p*-xylene for x_o = 240 µm PSLIT at RF drive frequencies of 16.76 MHz (——), 17.46 MHz (——), 21.26 MHz (——), 23.06 MHz (——), 24.76 MHz (——), and 25.76 MHz (——).

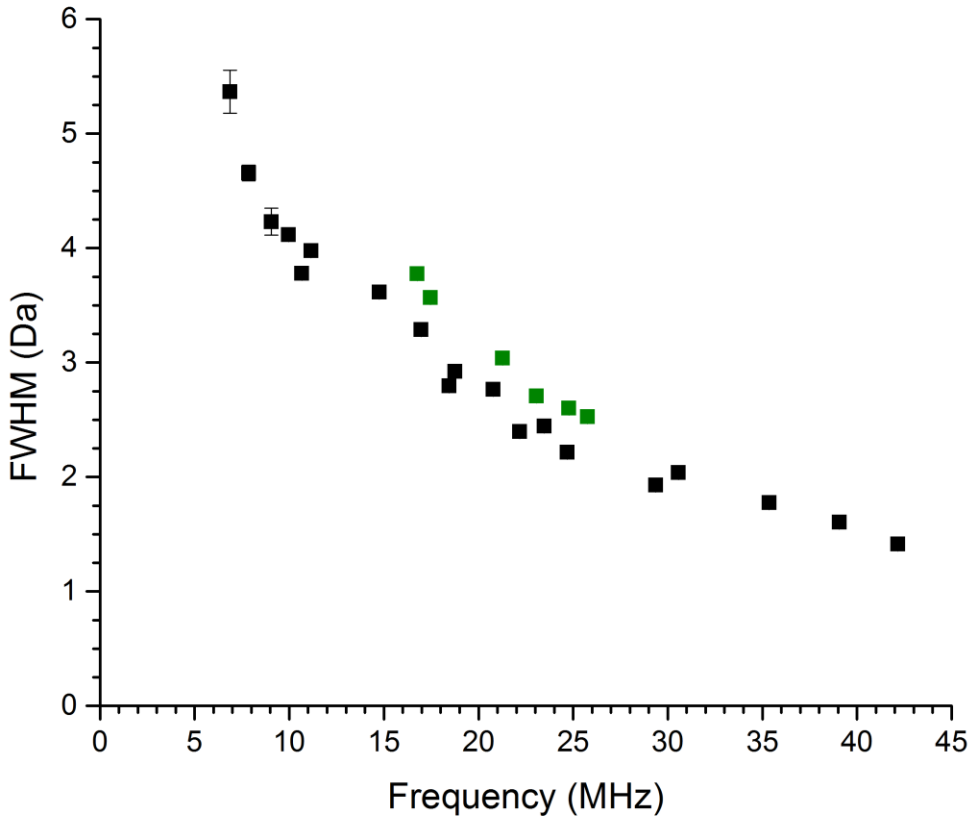

Figure 5.9: Peak widths for *p*-xylene 106 Da with increasing RF drive frequency for a MSLIT (■) and PSLIT (■). PCB based ion traps decrease capacitance and therefore the power required for RF trapping voltages.

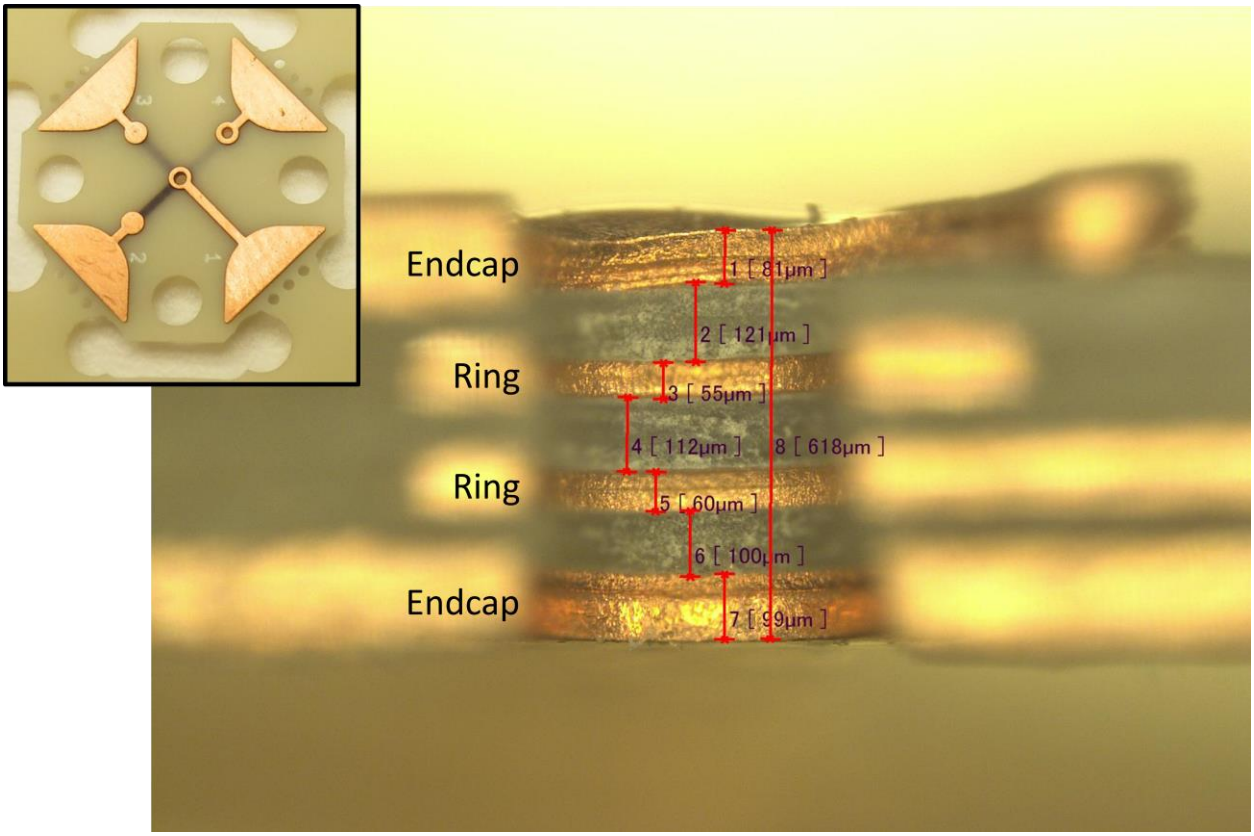

Figure 5.10: Images of the stacked electrode PCB trap showing the ring electrodes (two inner Cu layers) and endcap electrodes (outer two Cu layers). The electrodes are separated by FR-4 insulating material. Four Cu pads are used to make electrical contact to each layer.

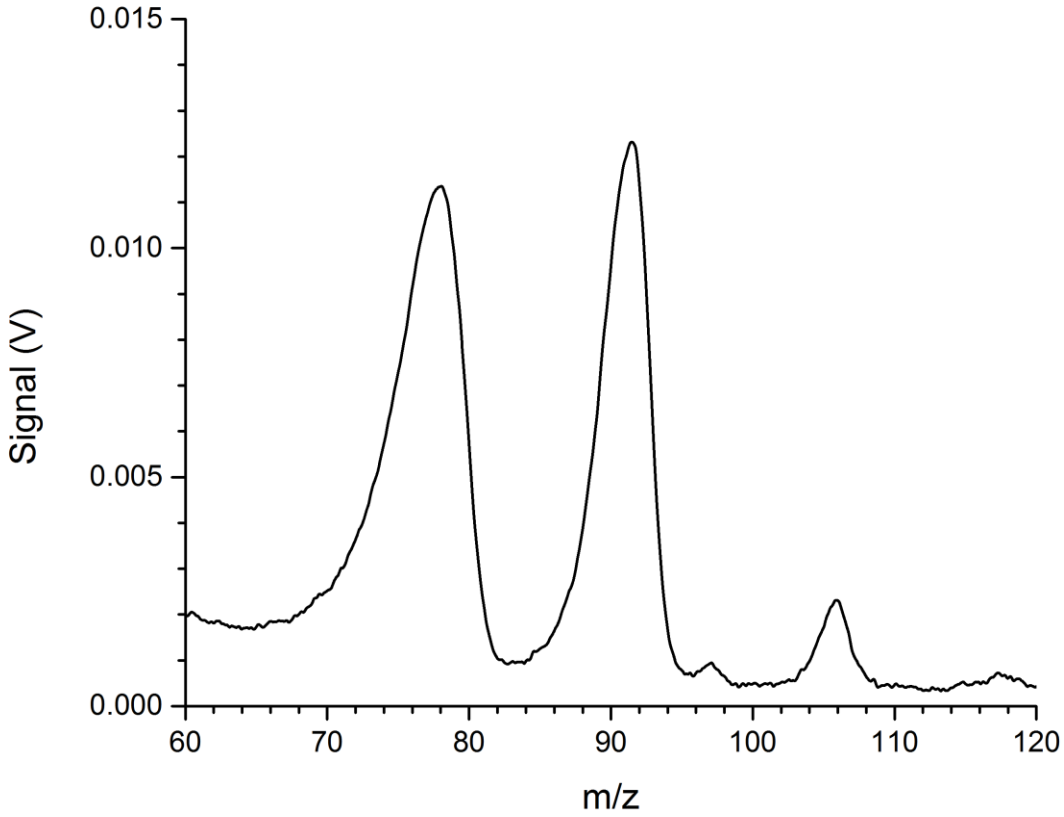

Figure 5.11: Mass spectra of *p*-xylene for the stacked electrode PCB trap. The CIT had critical dimensions of r_o = 300 µm and z_o = 225 µm and was operated with a RF frequency of 19.86 MHz. The ion trap pressure was 715 mTorr of ambient air.

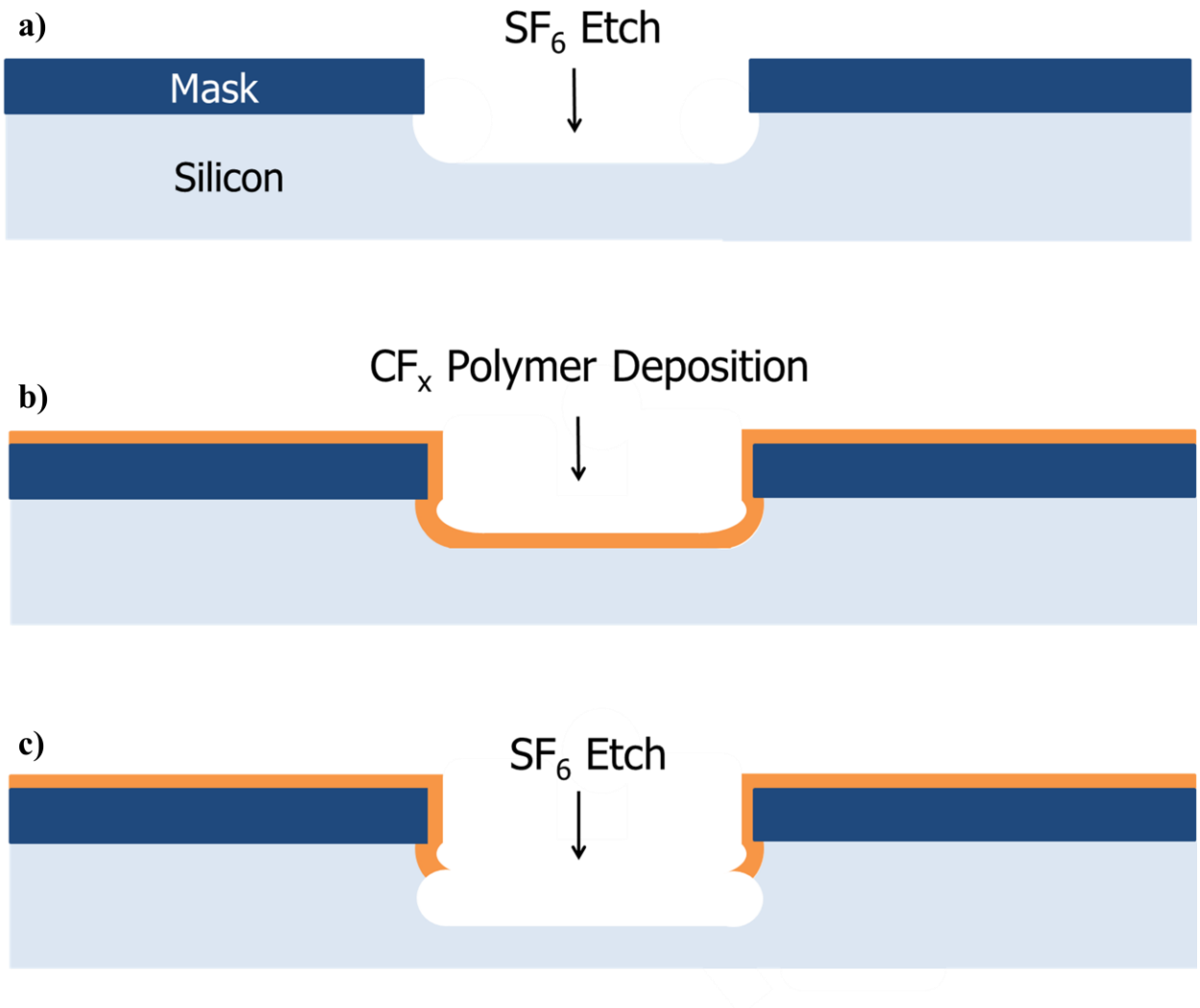

Figure 5.12: Schematic for the DRIE Bosch Process used to fabricate silicon-based ion traps. a) The patterned substrate is etched with a SF_6 plasma, forming a trench in the silicon b) A passivation layer of CF_x is deposited to the substrate trench and sidewalls c) The SF_6 plasma etches through the passivation layer on the trench and into the substrate, while the sidewalls are protected by the passivation layer. This alternating etching and deposition process is repeated many times to form high aspect ratio features.

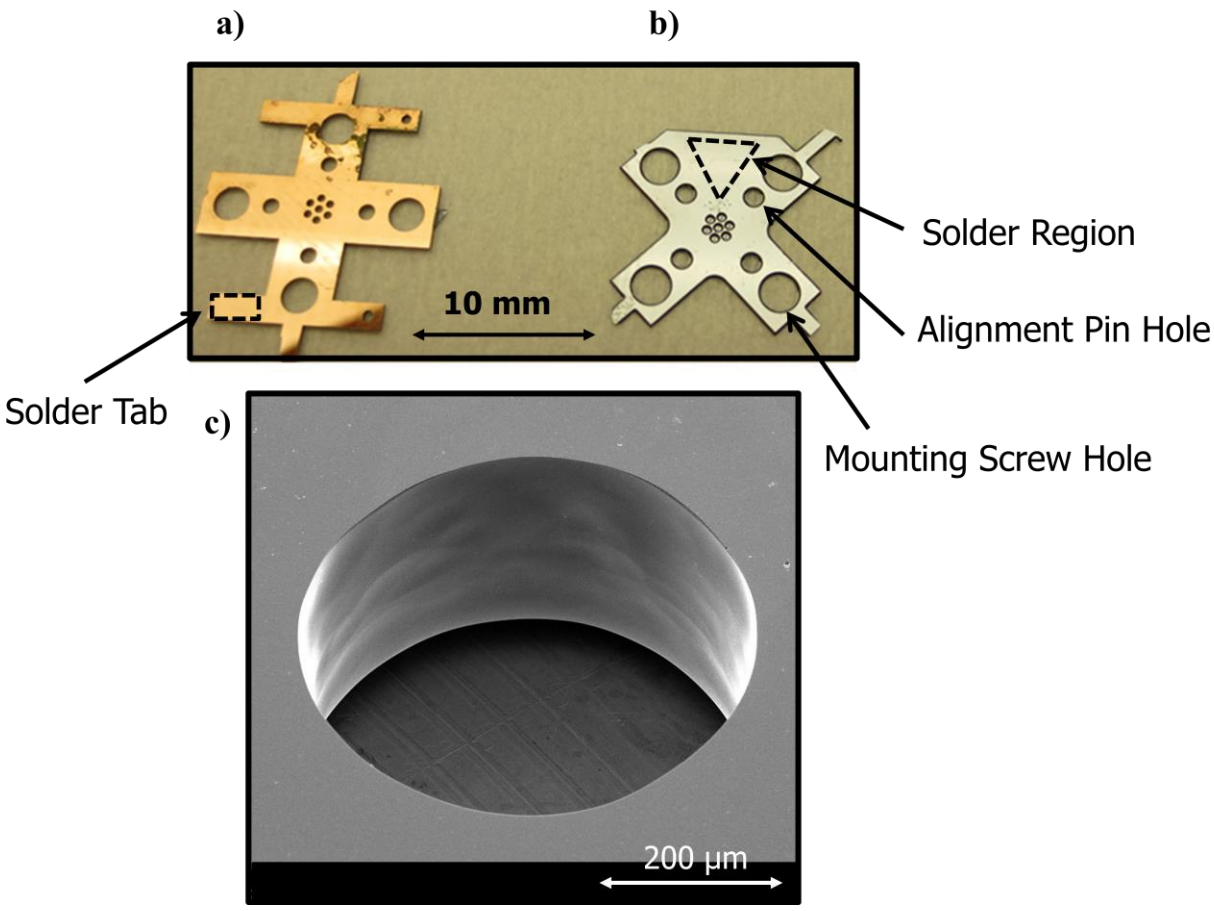

Figure 5.13: Silicon ion trap images. a) SCIT array (7 element, r_o= 250 µm) fabricated from highly doped silicon and coated with a thin layer of BeCu for electical contacts b) bare CIT array c) SEM image of a silicon electrode showing smooth sidewalls post-fabrication.

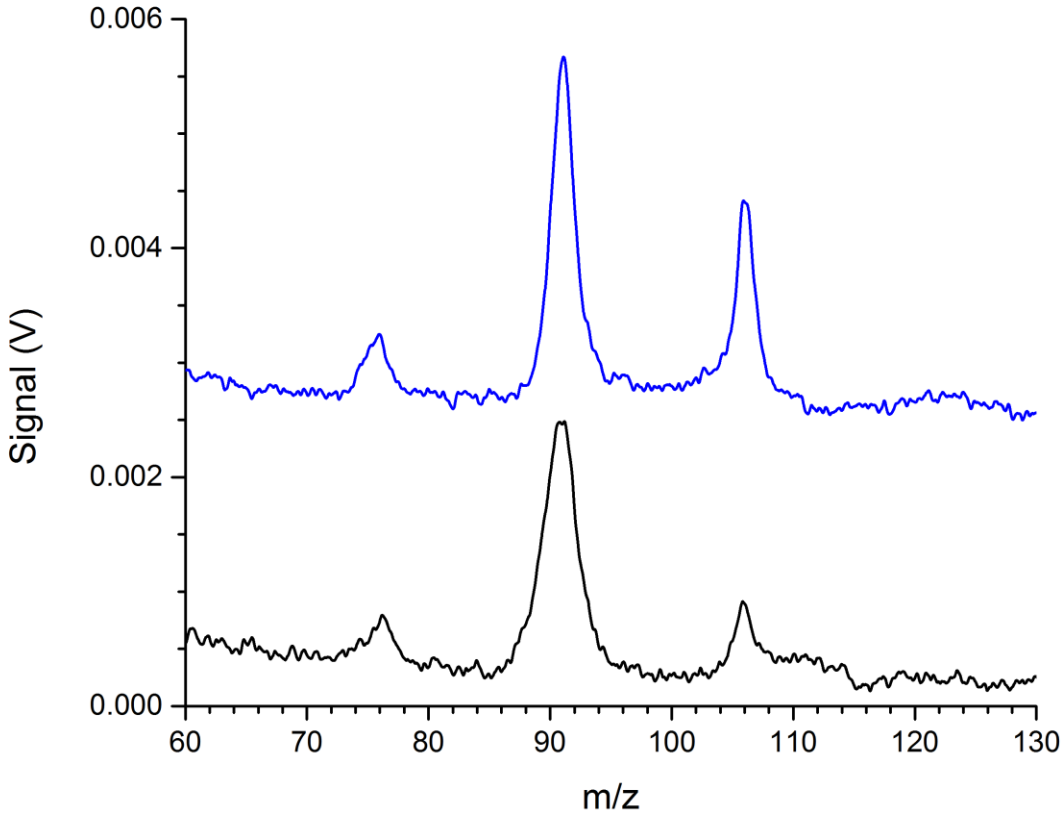

Figure 5.14: Mass spectra of *p*-xylene for r_o = 130 µm CITs operated with a RF frequency of 42 MHz at 1.0 Torr of ambient air comparing signal strength for MCIT (——) and SCIT (——).

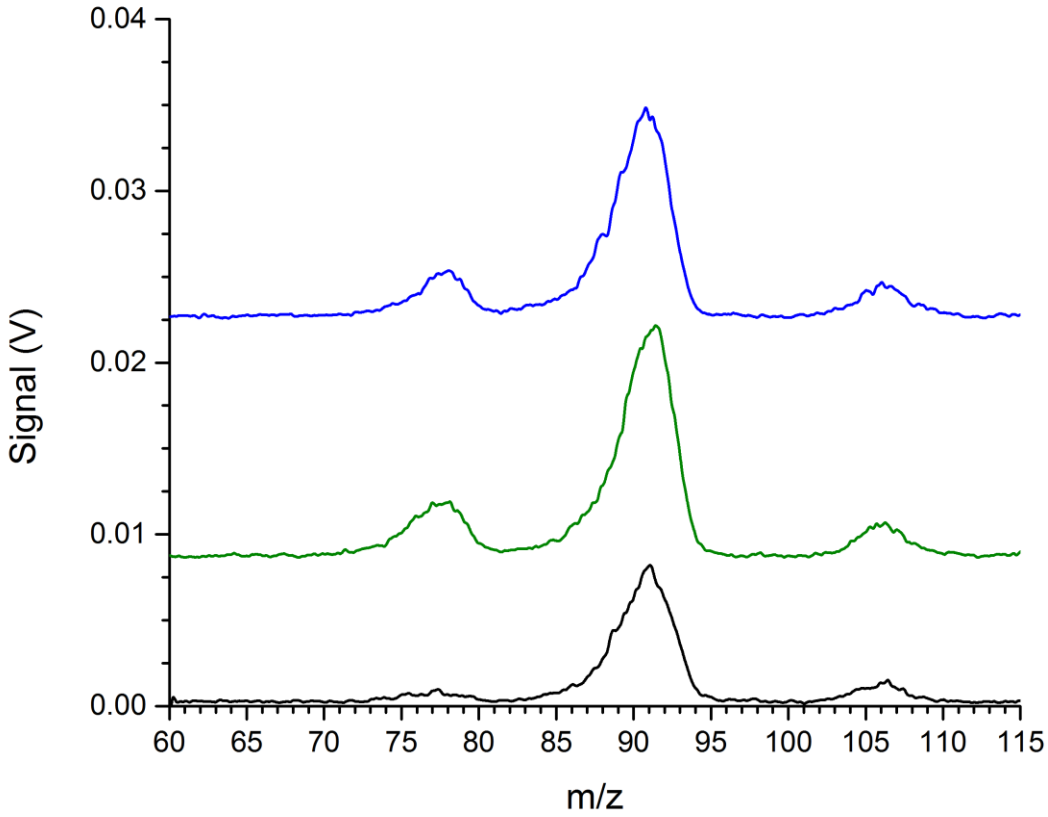

Figure 5.15: Mass spectra of *p*-xylene for a r_o = 225 µm hy-SCIT at RF drive frequencies of 17.90 MHz (——), 20.50 MHz (——), and 21.50 MHz (——).

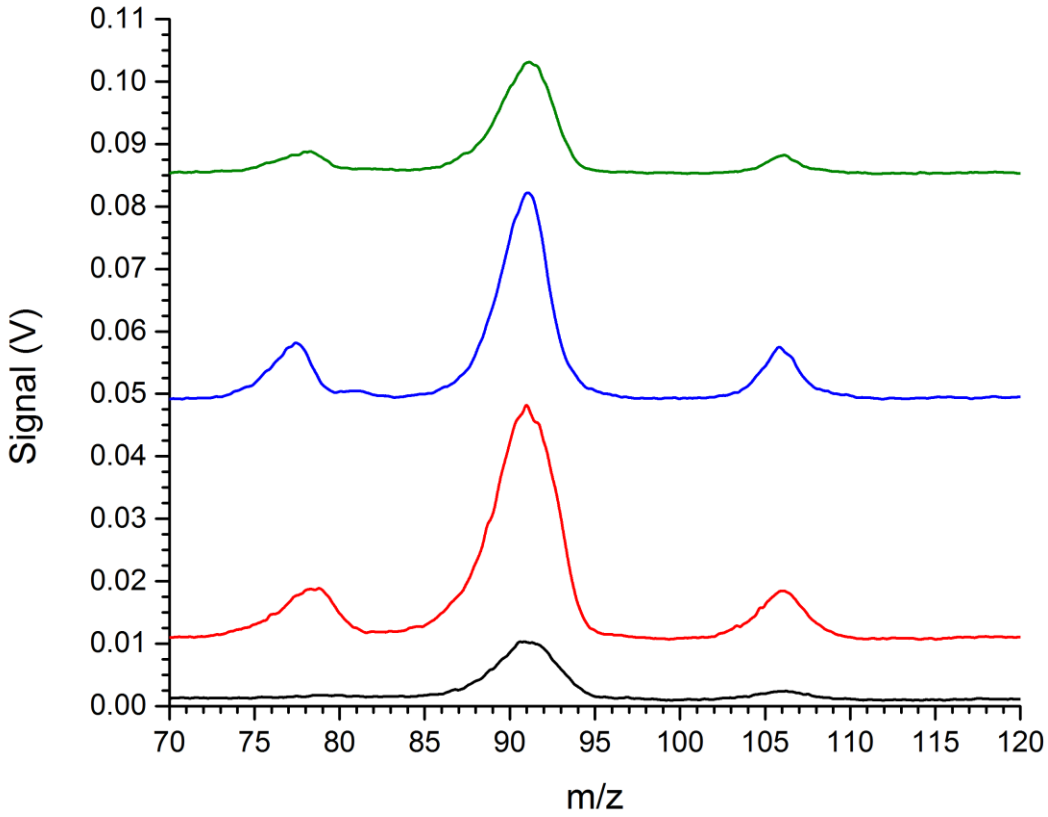

Figure 5.16: Mass spectra of *p*-xylene for a r_o = 250 µm SCIT at RF drive frequencies of 15.20 MHz (——), 17.80 MHz (——), 21.10 MHz (——), and 24.70 MHz (——).

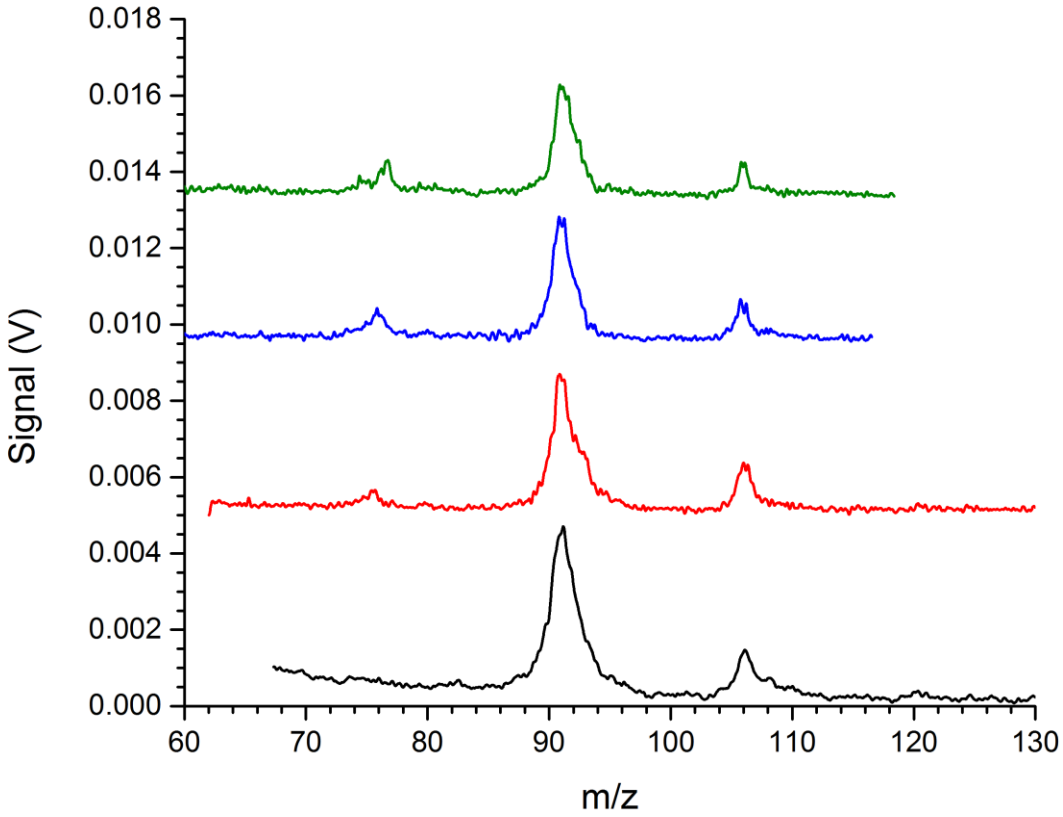

Figure 5.17: Mass spectra of *p*-xylene for a r_o = 130 µm SCIT at RF drive frequencies of 31.66 MHz (——), 37.36 MHz (——), 41.46 MHz (——), and 46.96 MHz (——).

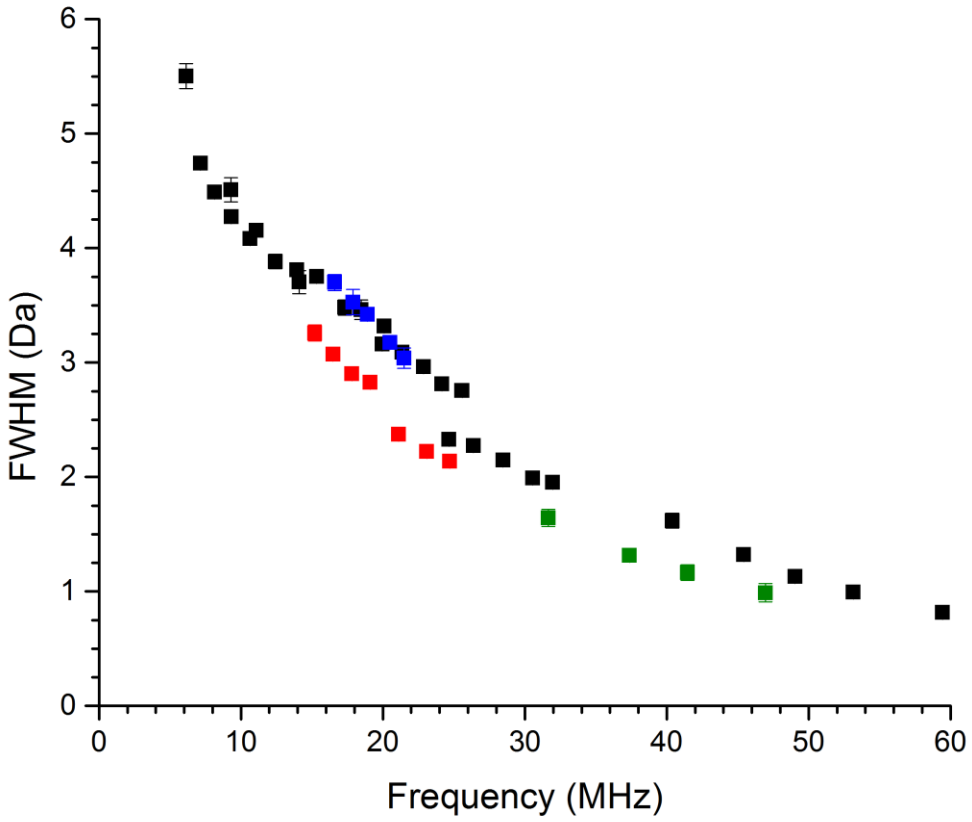

Figure 5.18: Peak widths for *p*-xylene 106 Da with increasing RF drive frequency for MCITs (■), r_o = 225 µm CIT hy-SCIT (■), r_o = 250 µm SCIT (■), and r_o = 130 µm SCIT (■).

5.5 References

1. Olsen, J. V.; Schwartz, J. C.; Griep-Raming, J.; Nielsen, M. L.; Damoc, E.; Denisov, E.; Lange, O.; Remes, P.; Taylor, D.; Splendore, M.; Wouters, E. R.; Senko, M.; Makarov, A.; Mann, M.; Horning, S., A dual pressure linear ion trap orbitrap instrument with very high sequencing speed. *Molecular & Cellular Proteomics* **2009,** *8* (12), 2759-2769.

2. Huber, G.; Deuschle, T.; Schnitzler, W.; Reichle, R.; Singer, K.; Schmidt-Kaler, F., Transport of ions in a segmented linear Paul trap in printed-circuit-board technology. *New Journal of Physics* **2008,** *10*.

3. Leach, F. E.; Norheim, R.; Anderson, G.; Pasa-Tolic, L., Application of printed circuit board technology to FT-ICR MS analyzer cell construction and prototyping. *Journal of the American Society for Mass Spectrometry* **2014,** *25* (12), 2069-72.

4. Brown, K. R.; Clark, R. J.; Labaziewicz, J.; Richerme, P.; Leibrandt, D. R.; Chuang, I. L., Loading and characterization of a printed-circuit-board atomic ion trap. *Physical Review A* **2007,** *75* (1).

5. Pearson, C. E.; Leibrandt, D. R.; Bakr, W. S.; Mallard, W. J.; Brown, K. R.; Chuang, I. L., Experimental investigation of planar ion traps. *Physical Review A* **2006,** *73* (3).

6. Kumph, M.; Brownnutt, M.; Blatt, R., Two-dimensional arrays of radio-frequency ion traps with addressable interactions. *New Journal of Physics* **2011,** *13*.

7. Crick, D. R.; Donnellan, S.; Ananthamurthy, S.; Thompson, R. C.; Segal, D. M., Fast shuttling of ions in a scalable Penning trap array. *Review of Scientific Instruments* **2010,** *81* (1).

8. Nelson, M. A., U.S. Patent 3,934,335. **1976**.

9. Suzuke, H., U.S. Patent 4,755,911. **1988**.

10. Wu, G. X.; Cooks, R. G.; Ouyang, Z., Geometry optimization for the cylindrical ion trap: field calculations, simulations and experiments. *International Journal of Mass Spectrometry* **2005,** *241* (2-3), 119-132.

11. Fico, M.; Yu, M.; Ouyang, Z.; Cooks, R. G.; Chappell, W. J., Miniaturization and geometry optimization of a polymer-based rectilinear ion trap. *Analytical Chemistry* **2007,** *79* (21), 8076-8082.

12. Xu, W.; Chappell, W. J.; Cooks, R. G.; Ouyang, Z., Characterization of electrode surface roughness and its impact on ion trap mass analysis. *Journal of Mass Spectrometry* **2009,** *44* (3), 353-360.

13. Van Steenberge, G.; Geerinck, P.; Van Put, S.; Van Koetsem, J.; Ottevaere, H.; Morlion, D.; Thienpont, H.; Van Daele, P., MT-compatible laser-ablated interconnections for optical printed circuit boards. *Journal of Lightwave Technology* **2004,** *22* (9), 2083-2090.

14. Gower, M. C., Industrial applications of laser micromachining. *Optics Express* **2000,** *7* (2), 56-67.

15. Park, Y. J.; Fray, D. J., Recovery of high purity precious metals from printed circuit boards. *Journal of Hazardous Materials* **2009,** *164* (2-3), 1152-1158.

16. Veit, H. M.; Bernardes, A. M.; Ferreira, J. Z.; Tenorio, J. A. S.; Malfatti, C. D., Recovery of copper from printed circuit boards scraps by mechanical processing and electrometallurgy. *Journal of Hazardous Materials* **2006,** *137* (3), 1704-1709.

17. Chew, W. C.; Kong, J. A., Effects of fringing fields on the capacitance of circular microstrip disk. *Ieee Transactions on Microwave Theory and Techniques* **1980,** *28* (2), 98-104.

18. Bansal, A., Paul, B. C., Roy, K., An analytical fringe capacitance model for interconnects using conformal mapping. *ISEE Transactions on Computer-Aided Design of Integrate Circits and Systems* **2006,** *25* (12), 2765-2774.

19. Wang, Y.; Franzen, J., The nonlinear resonance quistor .1. potential distribution in hyperboloidal quistors. *International Journal of Mass Spectrometry and Ion Processes* **1992,** *112* (2-3), 167-178.

20. Wang, Y.; Franzen, J.; Wanczek, K. P., The nonlinear resonance ion trap .2. A general theoretical-analysis. *International Journal of Mass Spectrometry and Ion Processes* **1993,** *124* (2), 125-144.

21. Schultze, K. P., Advanced System Components for the Development of a Handheld Ion Trap Mass Spectrometer. Ph.D. Dissertation, *UNC at Chapel Hill, North Carolina* **2014**.

22. Hauschild, J. P.; Wapelhorst, E.; Muller, J., Mass spectra measured by a fully integrated MEMS mass spectrometer. *International Journal of Mass Spectrometry* **2007,** *264* (1), 53-60.

23. Syms, R., Advances in microfabricated mass spectrometers. *Analytical and Bioanalytical Chemistry* **2009,** *393* (2), 427-429.

24. Taylor, S.; Tindall, R. F.; Syms, R. R. A., Silicon based quadrupole mass spectrometry using microelectromechanical systems. *Journal of Vacuum Science & Technology B* **2001,** *19* (2), 557-562.

25. Boumsellek, S.; Ferran, R. J., Trade-offs in miniature quadrupole designs. *Journal of the American Society for Mass Spectrometry* **2001,** *12* (6), 633-640.

26. Wapelhorst, E.; Hauschild, J. P.; Muller, J., Complex MEMS: a fully integrated TOF micro mass spectrometer. *Sensors and Actuators a-Physical* **2007,** *138* (1), 22-27.

27. Diaz, J. A.; Giese, C. F.; Gentry, W. R., Sub-miniature ExB sector-field mass spectrometer. *Journal of the American Society for Mass Spectrometry* **2001,** *12* (6), 619-632.

28. van Ameron, F. H. W. C., A., Cardenas, M., Bumgarner, J., Short, R. T., Microfabrication of cylindrical ion trap mass spectrometer arrays for handheld chemical analyzers. *Chemical Engineering Communications* **2008,** *195*, 98-114.

29. Chaudhary, A.; van Amerom, F. H. W.; Short, R. T., Development of microfabricated cylindrical ion trap mass spectrometer arrays. *Journal of Microelectromechanical Systems* **2009,** *18* (2), 442-448.

30. Chaudhary, A.; van Amerom, F. H. W.; Short, R. T., Experimental evaluation of micro-ion trap mass spectrometer geometries. *International Journal of Mass Spectrometry* **2014,** *371*, 17-27.

31. Blain, M. G.; Riter, L. S.; Cruz, D.; Austin, D. E.; Wu, G. X.; Plass, W. R.; Cooks, R. G., Towards the hand-held mass spectrometer: design considerations, simulation, and fabrication of micrometer-scaled cylindrical ion traps. *International Journal of Mass Spectrometry* **2004,** *236* (1-3), 91-104.

32. Cruz, D.; Chang, J. P.; Fico, M.; Guymon, A. J.; Austin, D. E.; Blain, M. G., Design, microfabrication, and analysis of micrometer-sized cylindrical ion trap arrays. *The Review of Scientific Instruments* **2007,** *78* (1), 015107.

33. Pau, S.; Pai, C. S.; Low, Y. L.; Moxom, J.; Reilly, P. T. A.; Whitten, W. B.; Ramsey, J. M., Microfabricated quadrupole ion trap for mass spectrometer applications. *Physical Review Letters* **2006,** *96* (12).

34. Zhang, Z. P.; Peng, Y.; Hansen, B. J.; Miller, I. W.; Wang, M.; Lee, M. L.; Hawkins, A. R.; Austin, D. E., Paul trap mass analyzer consisting of opposing microfabricated electrode plates. *Analytical Chemistry* **2009,** *81* (13), 5241-5248.

35. Laermer, F., Schilp, Andrea., U.S. Patent 5,501,893. **1996**.

36. Laermer, F.; Urban, A., Challenges, developments and applications of silicon deep reactive ion etching. *Microelectronic Engineering* **2003,** *67-8*, 349-355.

37. Laermer, F.; Urban, A.; Bosch, R., Milestones in deep reactive ion etching. *Transducers '05, Digest of Technical Papers, Vols 1 and 2* **2005**, 1118-1121.

38. Jansen, H. V.; de Boer, M. J.; Unnikrishnan, S.; Louwerse, M. C.; Elwenspoek, M. C., Black silicon method X: a review on high speed and selective plasma etching of silicon with profile control: an in-depth comparison between Bosch and cryostat DRIE processes as a roadmap to next generation equipment. *Journal of Micromechanics and Microengineering* **2009,** *19* (3).

39. Appelt, B. K.; Tseng, A.; Chen, C. H.; Lai, Y. S., Fine pitch copper wire bonding in high volume production. *Microelectronics Reliability* **2011,** *51* (1), 13-20.

40. Zhong, Z. W., Wire bonding using copper wire. *Microelectronics International* **2009,** *26* (1), 10-16.

41. Toyozawa, K.; Fujita, K.; Minamide, S.; Maeda, T., Development of copper wire bonding application technology. *Ieee Transactions on Components Hybrids and Manufacturing Technology* **1990,** *13* (4), 667-672.

CHAPTER 6: CONCLUSIONS AND FUTURE DIRECTIONS

6.1 Conclusions

The goal of this project was to investigate system components necessary for high pressure mass spectrometry (HPMS) for use with a handheld mass spectrometer. The elimination of turbopumps from the instrumentation used in most mass spectrometers that operate below 1 mTorr yielded the necessary size, weight and power (SWaP) savings making the handheld unit possible. With these SWaP savings, handheld mass spectrometry is possible though the development of ionization sources, mass analyzers, and detectors capable of operating at high pressures is still necessary. The primary focus of this work was developing an ion trap mass analyzer operational at 1 Torr ambient air with unit mass resolution, while minimizing the power requirements.

To accomplish this, there were four objectives contributing towards developing handheld mass spectrometry. The first objective was to demonstrate HPMS using a cylindrical ion trap (CIT) with helium as the buffer gas at pressures near 1 Torr to establish a baseline for performance. With additional ion collisions reducing the efficiency of the ionization source, signal intensity was improved by increasing the electron accelerating energy. Mass resolution was characterized as a function of operating pressure with unit mass resolution at 1.0 Torr achieved, demonstrating the feasibility of HPMS in a miniaturized instrument. With an eye towards developing an oxygen tolerant ionization source, a silicon-

based microionizer was introduced as a low power, high pressure-tolerant field emission source.

The second objective was to develop HPMS with nitrogen and air buffer gases as field-available alternatives to helium. This would reduce SWaP as the need for carrying helium into the field would be unnecessary. Successful HPMS with both nitrogen and air buffer gases of individual VOCs and mixtures of VOCs were acquired at pressures up to 2 Torr. As predicted by theory, mass resolution is lost due to the larger buffer gases. As filament ionization sources are oxygen intolerant, glow discharge electron impact ionization (GD-EI) and glow discharge ionization (GDI) sources were introduced as low power, nitrogen and air tolerant ionization sources.

The third objective was to try and recapture mass resolution that is lost from operating the microscale ion traps at high pressures. This was accomplished by further miniaturizing the ion traps and operating at higher RF frequencies. Five CITs, with r_o ranging between 500 μm to 100 μm used with RF drive frequencies between 6.14 MHz to 59.44 MHz, showed that as CIT dimensions decreased and RF frequencies increased, unit mass resolution was possible. For comparison, commercial instruments typically use 1 cm traps at 1 MHz. As signal intensity decreases with trap size, alternative trap geometries, stretched length ion traps (SLIT) and 7-element CIT arrays were used to increase signal compared to single CITs. Mass resolution was maintained despite trap miniaturization and the use of more complex geometries than the single CIT.

The final objective characterized new ion trap electrodes as potential replacements for the wet etched metal electrodes with SWaP and fabrication procedure considerations guiding

trap design. Ion traps were fabricated using printed circuit board (PCB) technology and silicon wafers with MEMS fabrication techniques. The PCB traps lowered trap capacitance by up to an order of magnitude compared to metal traps, which should reduce the power needs for generating the RF voltages. The PCB trap fabrication procedure also lends itself to mass production. Silicon ion traps fabricated by the DRIE Bosch process had improved fabrication accuracy, reproducibility and smoother surface features. This resulted in peak widths that were up to 30% narrower than metal electrodes, while integrated signal was higher by a factor of 2.

6.2 Future Directions

There has been significant research in developing miniaturized ion traps for handheld mass spectrometers. This has included determining the relationship between mass resolution and pressure[1-2], the demonstration of microscale ion traps[3-4], and most recently high pressure operation. As a result of these efforts, the first handheld mass spectrometer, the M908, was released in 2014 by 908Devices, Inc..[5] The M908 is a 2 kg microscale ion trap based instrument with dimensions of 22 x 18.5 x 7.6 cm that runs 4 to 6 hours on a single battery charge. It was developed to operate at elevated ambient air pressures and uses a single miniaturized roughing pump.[6]

Though a commercial HPMS is available, continued development of ionization sources, mass analyzers, and detectors are still needed. For ionization, continued development of a solid state microionizer could decrease SWaP associated with ionization by two orders of magnitude. To date, most ionization development has focused on air sampling of volatile analytes. Alternative ionization sources such as electrospray ionization (ESI)

could expand the application of HPMS instruments to non-volatile samples including biologically relevant molecules.

Microscale ion traps were developed that operate at elevated pressures with unit mass resolution, but the tradeoff is higher RF power and lower sensitivity. Improved mass resolution increases potential HPMS applications but requires RF drive frequencies approaching 60 MHz or potentially above. The inefficiencies in current RF amplifiers limit the RF frequencies possible that also meet SWaP requirements for use in a miniature instrument (approximately 25 W). For example, the in-house produced benchtop RF amplifiers used for these studies are shoe-box sized and draw approximately 50 W operating near 1 kV (p-p) from 10 MHz to 60 MHz and clearly are not suitable for a handheld instrument. While miniaturized RF amplifiers have decreased power draw to 4.8 W at 7.63 MHz[7], more efficient RF amplifiers are still needed to take advantage of higher RF frequencies.

To reach the target mass resolution, smaller ion traps with lower charge capacity were necessary. While initial experiments were performed to improve sensitivity with CIT arrays and SLITs, limits of detection and linear dynamic range were not characterized and should be addressed. Between the CIT arrays and SLITs, SLIT arrays are the more promising approach for increasing sensitivity. Silicon-based ion traps with their tighter fabrication tolerances showed promise as electrode materials as they performed better than the metal ion traps. Taking advantage of the dimensional control due to the MEMs fabrication, larger ion trap arrays could be fabricated while maintaining mass resolution. Multi-layer silicon on insulator (SOI) wafers could also be used to eliminate manual construction of ion traps, simplifying fabrication as demonstrated with PCBs, but with better dimensional control. If

the dimensional tolerances could be improved for PCB traps, they also could be used as cost effective, low capacitance ion traps.

Finally, although not a focus for this work, the development of pressure insensitive Faraday cup detectors with improved sensitivity closer to those of commercially available electron multipliers are needed. While silicon-based ion traps show promise for large arrays that improve sensitivity, the signal loss associated with detection is still critical for detection limits. Through optimizing each part of the mass spectrometer (ionization source, mass analyzer, and detector), SWaP, mass resolution, sensitivity, and cost can all be improved for handheld instruments.

6.3 References

1. Goeringer, D. E.; Whitten, W. B.; Ramsey, J. M.; McLuckey, S. A.; Glish, G. L., Theory of high-resolution mass-spectrometry achieved via resonance ejection in the quadrupole ion trap. *Analytical Chemistry* **1992,** *64* (13), 1434-1439.

2. Arnold, N. S.; Hars, C.; Meuzelaar, H. L., Extended theoretical considerations for mass resolution in the resonance ejection mode of quadrupole ion trap mass spectrometry. *Journal of the American Society for Mass Spectrometry* **1994,** *5* (7), 676-88.

3. Kornienko, O.; Reilly, P. T. A.; Whitten, W. B.; Ramsey, J. M., Micro ion trap mass spectrometry. *Rapid Communications in Mass Spectrometry* **1999,** *13* (1), 50-53.

4. Kornienko, O.; Reilly, P. T. A.; Whitten, W. B.; Ramsey, J. M., Electron impact ionization in a microion trap mass spectrometer. *Review of Scientific Instruments* **1999,** *70* (10), 3907-3909.

5. 908devices, Introducing M908: the world's first handheld mass spectrometer for hazardous material detection and identification. *http://908devices.com/news/introducing-m908-worlds-first-handheld-mass-spectrometer-hazardous-material-detection-identification/* **(accessed March 30, 2015)**.

6. Brown, C. D., Handheld mass spectrometery at high pressures. *PITTCON 2015, New Orleans, LA, March 8-12, 2015, Session 130, Paper 6.* **2015**.

7. Schultze, K. P., Advanced System Components for the Development of a Handheld Ion Trap Mass Spectrometer, Ph.D. Dissertation. *UNC at Chapel Hill, North Carolina* **2014**.